Ph.D thesis

Mid-infrared Non-perturbative Nonlinear Optics in Atomically Thin Semiconductors

Department of Physics
Graduate School of Science
Kyoto University

Kohei Nagai

Abstract

Nonperturbative interactions between a strong mid-infrared laser field and electrons in solid induces various coherent dynamics of electrons and creates novel electronic states that cannot be understood within the framework of perturbation theory. The emergence of such new electronic states in a strong laser field leads to the discovery of new functionalities and ultrafast quantum control methods of materials that could be useful for future electronic and optical devices. High harmonic generation (HHG), which converts low-energy photons into visible and ultraviolet photons, is the simplest and most powerful means to study the nonlinear electronic response in solids driven by strong light. HHG was first studied in atomic gases for attosecond pulse sources, then extended to solids, and has been observed in many semiconductors. A number of theoretical studies explain the mechanism of HHG in semiconductors in terms of light-driven coherent electron dynamics in momentum space. However, understanding the microscopic electronic structure is still a subject of intense investigation. This is due to the complexity of the HHG mechanism. The understanding is extremely challenging since highly non-equilibrium states are realized in a strong field, and their typical energy scales are much larger than the fundamental excitations in solids, and they are accompanied by many-body interactions. Furthermore, it has been experimentally shown that the properties of HHG strongly depend on the material and its macroscopic structure, which makes microscopic physical understanding difficult. Therefore, a key issue in this research field is to clarify the microscopic and general physics governing the properties of strongly light-driven systems.

In this thesis, we study dynamical symmetry (DS), a general concept for electronic systems driven by a strong laser field in solids. The idea of DS was proposed in 1993, and has successfully explained HHG selection rules in atomic gases. A recent study formulated DS as a group theory and provided a general way to describe periodically driven systems. However, the validity of DS in solids remains non-trivial because the electron-electron scattering process and the accumulation of excited carriers during the application of strong infrared pulses may break DS, such as the time-periodicity of electron dynamics.

Here, we performed two experiments to understand the validity of DS in solids. First, we explored the DS by investigating the polarization selection rules of higher-order sideband generation (HSG) in semiconductors, a phenomenon similar to HHG. HSG is a nonperturbative higher-order sum-frequency generation process in solids that occurs when a weak near-infrared and a strong mid-infrared light pulses overlap in time. Next, to understand the effect of incoherent electron-hole pairs accumulated in HHG process, we performed an experiment in which incoherent photo-carriers were prepared by irradiating near-infrared pulses before MIR pulses in the same setup as in HSG. We used atomically thin layered semiconductors as experimental samples. High harmonics have been obtained from bulk solids in many experimental studies. However, propagation effects, such as phase matching and reabsorption, occur when light propagates through the sample and

may obscure the harmonic spectrum generated by the microscopic mechanism. In this study, we used monolayer semiconducting transition metal dichalcogenides to avoid such effects.

In Chapter 1 of this thesis, we introduce nonperturbative optical phenomena and optical properties of transition metal dichalcogenides (TMDs). In Chapter 2, we present the theoretical formulation of DS and its connection to HHG. In Chapter 3, we determine the polarization selection rules of HSG in monolayer MoS_2, a kind of TMDs. In the experiments, we systematically determined the polarization selection rules for circular and linear polarization by controlling the polarization of near-infrared and mid-infrared light and measuring the spectra by resolving the sideband polarization. Figure 1 shows the results for circularly polarized light. Clear polarization selection rules were obtained for incident light of four different polarizations. A new physical picture of HSG as "Raman scattering in Floquet system" is proposed, which provides a comprehensive understanding of the selection rules. We found a perfect agreement between the experimental and theoretical selection rules. This result indicates that DS well describes the nature of intense light-driven semiconductors. In Chapter 4, we studied the effect of photo-carrier doping on HHG. We observed HHG in monolayer WSe_2 and confirmed a weak enhancement of the fifth harmonics (appearing at the lower energy side of the absorption edge) and a strong suppression of the higher harmonics (at higher energy side of the absorption edge) following the photo-carrier doping. Numerical calculations showed that the enhancement is due to the increase in the intraband current of photo-carriers, which is relatively suppressed by momentum relaxation. In addition, we found that the incoherent carriers generated by the mid-infrared light pulse promote the dephasing of the interband polarization later in the MIR pulse duration. In addition, we discuss the validity of DS and its relation to many-body effects. In Chapter 5, we summarize this thesis and discuss future prospects.

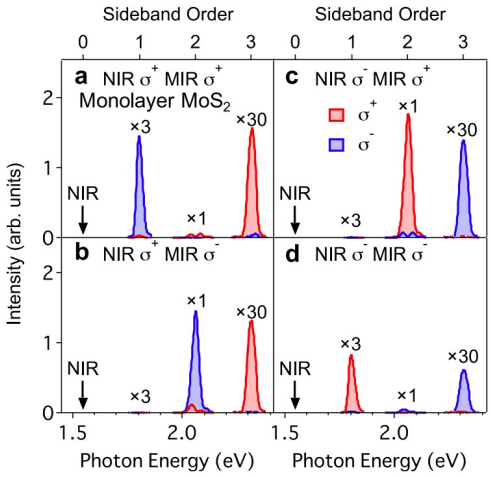

Figure 1: Circular polarization-resolved high-order sideband generation (HSG) spectra. Red and blue shaded areas indicate σ^+-, σ^--polarized spectra. The polarizations of near-infrared (NIR) and mid-infrared (MIR) are respectively **a** (σ^+, σ^+), **b** (σ^+, σ^-), **c** (σ^-, σ^+), **d** (σ^-, σ^-). Reproduced from K. Nagai *et al.*, Communications Physics **3**, 137 (2020). ©2020 The authors. Distributed under a Creative Commons Attribution 4.0 International license (CC BY 4.0) [1].

概要

強い中赤外レーザー電場と固体中との電子の非摂動的な相互作用は、様々な電子のコヒーレントダイナミクスを誘起し、摂動論の枠組みで理解できない新しい電子状態を作り出す。このような強い光電場中における新たな電子状態の出現は、将来の電子・光デバイスや量子情報技術に役立ちうる物質の新しい機能性や超高速量子制御法の発見につながる。低エネルギーの光子を可視光や紫外光に変換する高次高調波発生（HHG）は、強く光で駆動された固体における非線形な電子応答を研究するための最も単純かつ強力な手段である。HHG は、原子ガス中のアト秒光源のために研究された後、固体に拡張され、多くの半導体、絶縁体において現在観測がなされている。様々な理論的研究が行われ、その多くは半導体における HHG のメカニズムを、波数空間において光に駆動されるコヒーレントな電子と正孔のダイナミクスの観点から説明してきた。しかし、微視的な電子状態の理解を目指した研究はいまだに盛んに行われている。これは HHG のメカニズムの複雑性に起因する。高強度光下においては非常に非平衡な状態が実現され、その典型的なエネルギースケールは固体の基本的な励起に比べて大きく、さらに多体の相互作用などを伴うことなどからその理解は極めて困難である。さらに、HHG の特性は材料やそのマクロな構造に強く依存することが実験的に明らかになってきており、微視的な物理的理解が難しい。そのため、この研究分野においては、強く光駆動された系の特性を支配する微視的で一般的な物理を明らかにしていくことが重要な課題となっている。

本論文では、強い光電場で駆動された電子系の一般的な概念である動的対称性（DS）を固体において研究する。DS のアイデアは 1993 年に提案され、DS は原子気体における HHG の選択則をうまく説明してきた。最近の研究は DS を群論として定式化し、周期的に駆動する系を記述する一般的な方法を明らかにした。しかし、固体中での DS の有効性は依然として非自明であった。というのも、強い赤外パルスを印加する際の電子-電子散乱過程や励起キャリアの蓄積が、電子ダイナミクスの時間周期性などの DS を壊してしまう可能性があるからである。

ここでは固体における DS の有効性を理解するために、2 つの実験を行った。まず、HHG と似た現象である半導体中の高次サイドバンド発生（HSG）の偏光選択則を調べることで、DS の有効性を探った。HSG は、弱い近赤外光パルスと強い中赤外光パルスが時間的に重なったときに起こる、固体中の非摂動的な高次和周波発生過程である。次に、光パルスを照射する時間中に蓄積されたインコヒーレントなキャリアが HHG に与える影響を調べ、その時間中におけるキャリアダイナミクスの動的対称性の破れについて研究した。HHG におけるインコヒーレントな電子正孔対がもたらす影響について解明するために、HSG と同じ実験系で、MIR パルス照射前に近赤外パルスを照射してインコヒーレントな光キャリアを用意する実験を行った。また本研究では実験試料として原子層薄膜半導体を用いた。多くの実験的な研究においては HHG を観測する対象の物質としてバルクの固体を用いていたが、これでは光が試料中を伝播する際に生じる、位相整合や再吸収といった効果が微視的なダイナミクスを反映した高調波スペクトルを変調してしまう可能性がある。そこで本研

究においてはこれらの効果を避けるため層状半導体である遷移金属ダイカルコゲナイドの単原子層薄膜を用意し、実験を行った。

本論文の第 1 章では、非摂動的な光学現象、高次高調波発生と遷移金属ダイカルコゲナイドの光学特性について紹介する。第 2 章では、DS の理論的な定式化と高次高調波発生との関係について紹介する。第 3 章では、TMD の一種である MoS_2 の単層膜における HSG の偏光選択則を実験、理論の両面から決定する。実験においては近赤外光と中赤外光の偏光を制御し、サイドバンドの偏光を分解してスペクトルを測定することで円偏光と直線偏光の偏光選択則を系統的に決定した。図 1 は円偏光に対する結果を示しており、はっきりとした偏光の選択則が 4 つの異なる偏光の入射光に対して得られていることがわかる。この選択則を説明するために、DS を用いた理論的枠組みを構築した。HSG を「フロケ系におけるラマン散乱」とみなす新たな物理的描像を提案し、選択則を包括的に理解する方法を示した。実験と理論で得られた選択則は完全に一致することが明らかになった。この結果は DS が高強度光駆動された半導体をよく記述する概念であることを示している。第 4 章では、光キャリアドーピングの効果を調べることで、半導体に強い赤外パルスを照射した際に蓄積されたインコヒーレント電子正孔対の影響を研究した。単層の WSe_2 において HHG を観測し、光キャリアをドーピングした際に 5 次高調波（吸収端より低エネルギー側）の小さな増強と、高次高調波（吸収端より高エネルギー側）の大きな抑制が確認された。実験結果を再現する数値計算を行った結果、5 次高調波の増加は光キャリアによるバンド内電流の増大に起因するが、これは運動量緩和によって相対的に抑制されることがわかった。また、MIR 光パルスによって生成されたインコヒーレントなキャリアは、パルスの後半でバンド間分極に対する位相緩和を促進していることがわかった。また、DS の有効性と多体効果との関係について議論する。第 5 章では、本論文のまとめと今後の展望を述べる。

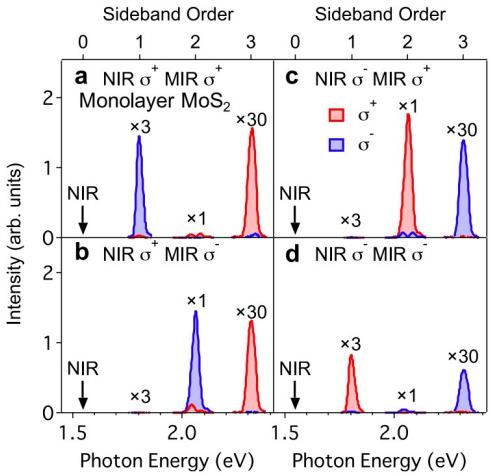

図 1: 円偏光に分解した高次サイドバンド発生のスペクトル。赤と青の領域はそれぞれ σ^+、σ^- 偏光のスペクトルを示す。それぞれ近赤外 (NIR) および中赤外 (MIR) 光の偏光が **a** (σ^+, σ^+), **b** (σ^+, σ^-), **c** (σ^-, σ^+), **d** (σ^-, σ^-) の場合を示す。Reproduced from K. Nagai *et al.*, Communications Physics **3**, 137 (2020). ©2020 The authors. Distributed under a Creative Commons Attribution 4.0 International license (CC BY 4.0) [1].

Contents

Chapter 1

Introduction

The study on nonperturbative interactions between ultrafast laser pulses and electrons in solids opened a way for exploring novel material properties and developing an ultrafast technique for quantum control of materials. A challenging issue has been how to generally describe the electronic state under the strong laser field. This thesis focuses on elucidating the validity of dynamical symmetry in solids, which is a promising concept for describing the periodically driven system.

In this Chapter, we introduce nonperturbative nonlinear optics in solids in Section 1.1 In Section, 1.2, we focus on the explanation of nonperturbative high harmonic generation, which is the most simple and powerful way to examine the strongly light-driven electronic system. In Section, 1.3, we introduce dynamic symmetry, which is the core concept in this thesis. In Section, 1.4, we introduce monolayer transition metal dichalcogenides that are an ideal platform for high harmonic generation.

1.1 Nonperturbative nonlinear optics in solids

Nonperturbative nonlinear optics is initiated by the development of strong ultrashort laser pulses. A broad review of the nonperturbative nonlinear optics in solids is provided in this section.

1.1.1 Development of ultrashort pulse laser technique

In our daily life, light is used as a tool to see objects in a great variety of applications such as industry, medicine, and science. Before the development of lasers, it was believed that light could not change the state of matter. After the invention of the ruby laser in 1960, P. A. Franken et al. realized a nonlinear optical phenomenon, second harmonic generation, in 1961, and the study of nonlinear optics began [2]. Since then, it has become clear that light can be used not only to see objects, but also to change their states and to control its physical properties. The first ruby laser had a focused intensity of about 10^7 W cm^{-2}, followed by the development of Q-switched lasers, mode-locked lasers, and laser amplification techniques, which led to short-pulse and high-power lasers. However, the breakdown of the laser medium or reflector was the limit of the output power, and it was difficult to increase the output power of the laser [3]. In 1985, the development of chirped-pulse amplification (CPA) broke through this limitation [4]. In CPA, short pulses are temporally stretched to reduce their peak power, and then amplified and shrunk

again to produce high-intensity pulses. This technology has dramatically increased the laser power and the highest focused intensity to about 10^{22} or 10^{23} W/cm^{-2} [5, 6]. The development of nonperturbative nonlinear optics, which will be presented in the next sections, was initiated by the development of such intense ultrashort pulsed lasers.

1.1.2 Nonperturbative light-matter interaction in solids

In this section, we describe nonperturbative light-matter interaction in solids. The development of ultrashort pulsed laser generation technology has made it possible to induce nonperturbative nonlinear optical phenomena that go beyond conventional nonlinear optics [3,7]. The magnitude of the light-matter interaction is important for the manifestation of such phenomena. The Hamiltonian H for a system in which light and matter interact is generally written as

$$H = H_0 + H_I. \tag{1.1}$$

H_0 is the Hamiltonian of matter in the absence of external fields, and H_I denotes the Hamiltonian of the interaction between light and matter. In the case of $H_0 \gg H_I$, the interaction between light and matter can be treated within the framework of perturbation theory, and the system lies almost in the ground state. However, in the case of $H_0 \lesssim H_I$, i.e., when the magnitude of the interaction is equal to or larger than the typical energy scale of matter, H_I is no longer considered as a perturbation to matter, and the quantum state undergoes such an extensive modulation that it deviates from the ground state. Such an interaction energy regime is called nonperturbative. In such a nonperturbative regime, light is no longer seen as a photon but rather as an electric field. There are various degrees of freedom in solids, such as electrons, spin, and lattice, but electrons interact most strongly with light and determine the material response to intense light. How do electrons in solids behave in intense light? This question has opened up a field of research that now has a variety of attractions.

The variety of nonperturbative phenomena is attractive as a research subject in physics, for example, Zener tunneling, Bloch oscillation, Wannier Stark localization, and dynamical Franz-Keldysh effect in electronic systems in semiconductors [8]. These phenomena are caused in significantly modulated electronic states from the ground state of matter, which will lead to the emergence of novel quantum states and phenomena in solids.

In addition, lightwave electronics are also attracting increasing interest as electronics that can ultimately be performed at high speed with low energy consumption [9, 10]. Standard electronics involves joule heating according to Ohm's law by applying an external voltage to a semiconductor. On the other hand, lightwave electronics can realize the electronics with less dissipation and ultimately lower energy consumption. The electric field of ultrashort pulse laser manipulates the movement of electrons ballistically or modulates the conductivity of matter. It may also lead to the realization of fast electronics at a petahertz clock rate beyond the limit of terahertz in conventional electronics [11–14].

Moreover, solid-state electron systems in the intense laser external field have been the subject of the study of Floquet theory, which can be applied for the nonperturbative regime [15–20]. Floquet theory can treat the problem of time-periodic systems as an eigenvalue problem and gives further insight into the dynamics of the system. According to the formalism of the Floquet theorem, by manipulating the intensity and frequency of the external field and its waveforms, we can give the Hamiltonian the desired properties.

This is called Floquet engineering and is expected to lead to next-generation quantum control technology. Floquet engineering is similar to the photo-induced phase transition, which has been studied for many years to control materials for device applications [21], but the target time scales are different [18, 22]. While the photo-induced phase transition aims to switch the material properties before and after the passage of an ultrashort light pulse, Floquet engineering aims to control the material during the pulse duration, which remains a field to be developed in the future.

As described above, strong light-matter interactions in solids are a very attractive research field from the viewpoint of fundamental physics and material science, high-speed electronics, and ultrafast material control. The most straightforward and powerful tool for studying such a system is the nonperturbative high harmonic generation (HHG), which converts low-energy photons to higher energy photons. High harmonic generation (HHG) has been studied in atomic gases and extended to solids in recent years. It has potential applications as a compact extreme ultraviolet light source or as a spectroscopic method to study electron dynamics in solids on the attosecond time scale. In the following, we will introduce HHG and discuss the current status of the research.

1.2 High harmonic generation

In this section, we introduce HHG in atomic gases and solids. We start with a brief introduction to nonlinear optics. We explain the mechanism of HHG and its historical background in the following sections. We also discuss the current issue of the research on HHG in solids.

1.2.1 Conventional nonlinear optics

Conventional nonlinear optics deals with a region where the perturbation theory can treat the interaction, i.e., $H_0 \gg H_I$. In this case, the optical polarization induced in the material is given by the Taylor expansion for the laser electric field $E(t)$.

$$P(t) = \varepsilon_0(\chi^{(1)}E(t) + \chi^{(2)}E^2(t) + \chi^{(3)}E^3(t) + \cdots) \tag{1.2}$$

$\chi^{(1)}$ is a linear susceptibility, $\chi^{(n)}(n > 1)$ are nonlinear susceptibilities. This expansion is useful when the laser light is weak and not resonant with the electronic transitions. Also, we neglect the relativistic effect of the charge here.

For example, let us consider the second term of eq. (1.2). We consider the electric field of

$$E(t) = \tilde{E}(t)\cos(\omega t + \phi), \tag{1.3}$$

where $\tilde{E}(t)$ is envelop function and ϕ is a so-called carrier envelop offset. In this case,

$$\chi^{(2)}E^2(t) = \chi^{(2)}\tilde{E}^2(t)\cos^2(\omega t + \phi) \tag{1.4}$$

$$= \chi^{(2)}\tilde{E}^2(t)\frac{1}{2}(1 + \cos^2(2(\omega t + \phi))) \tag{1.5}$$

Electromagnetic waves are radiated from such nonlinear polarization according to Maxwell's equations. The first term 1 in eq. (1.5) reflects so-called optical rectification or the photo-galvanic effect. The second term has a carrier frequency of 2ω, which describes second

harmonic generation. In the same way, the third term of eq. (1.2) describes third harmonic generation and self-phase modulation.

Here, when the laser intensity $E(t)$ becomes equal to or larger than the typical energy of matter, the Taylor expansion in eq. (1.2) breaks down due to the divergence of the higher order terms. This leads to novel nonlinear optical phenomena that cannot be explained by the conventional nonlinear optics, called nonperturbative nonlinear optical phenomena.

1.2.2 High harmonic generation in atomic gases

The primary example of nonperturbative nonlinear optical phenomena is high harmonic generation (HHG) in atomic gases, where light with integer multiples of the excitation frequency is emitted, i.e.,

$$\omega_{HHG} = n\omega, \quad (n\text{: integer}) \tag{1.6}$$

where ω_{HHG} is the angular frequency of high harmonic and ω is that of the excitation laser. This phenomenon was discovered in 1987 by a group at the University of Illinois by using femtosecond laser pulses [23] and then experimentally investigated by many research. Later, the physical properties of HHG were semiclassically very well understood by the model proposed by P. B. Corkum in 1993 [24]. Currently, HHG is used as X-ray sources and attosecond pulse sources [25, 26].

The spectra of HHG in atomic gases show their nonperturbative features. The higher harmonic spectrum from a typical atomic gas (Helium) is shown in Fig. 1.1 [27]. This spectrum was generated when a Ti:sapphire laser was irradiated on gaseous helium at a high intensity of 10^{15} W/cm^2. The n-th order harmonic generation within the perturbative nonlinear optics is generated by n times interactions of the photons with the atom. As a result, the intensity of harmonic generation decays exponentially with increasing the harmonic order. However, the obtained harmonic intensity does not decrease even up to the wavelength of 11 nm, and the intensity suddenly starts to decrease exponentially. These are nonperturbative features called plateau and cutoff, respectively.

It is known that the following relation is established for the cutoff energy E_c

$$E_c = 3.17U_p + I_p, \tag{1.7}$$

where

$$U_p = \frac{e^2E_0^2}{4m\omega^2} \tag{1.8}$$

is the ponderomotive energy and I_p is the ionization energy of the target atom. The ponderomotive energy is the cycle-averaged kinetic energy of free electrons with the charge of $-e$ obtained from a laser field. E_0 is the amplitude of the electric field, and ω is its frequency. Note that this formula is independent of the detailed electronic structure of the atom.

The three-step model proposed by P. B. Corkum succeeded in explaining this relationship. This semiclassical model describes the electron dynamics in a strong field underlying HHG. Figure1.2 is the schematics explaining the following three-step model [25],

1. Tunnel ionization of electron

2. Acceleration in the laser field

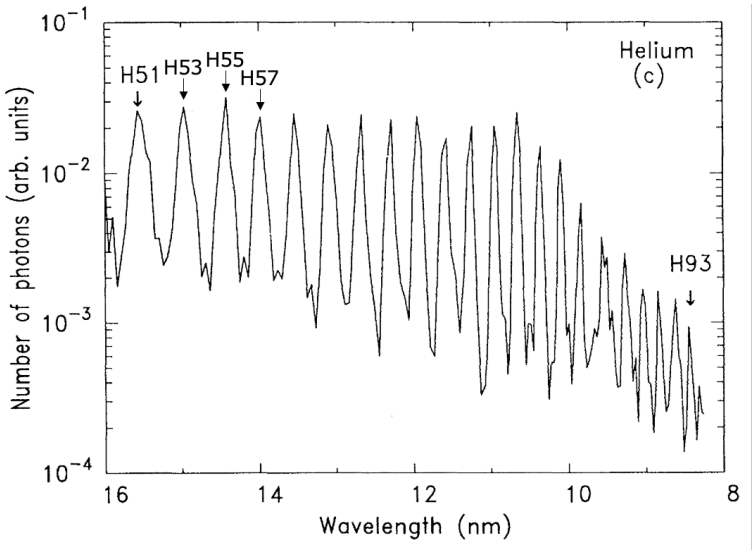

Figure 1.1: High harmonic generation in Helium gas [27]. Reprinted figures with permission from Ref. [27]. Copyright 1993 by American Physical Society.

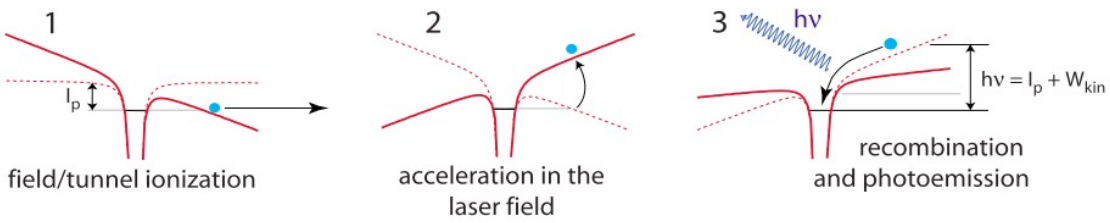

Figure 1.2: Three-step model for high harmonic generation in atomic gases [25]. Reprinted figures with permission from Ref. [25]. Copyright 2008 by American Physical Society.

3. Recombination and emission of a high-energy photon

The first step in Fig. 1.2 describes the tunnel ionization of the electron. This phenomenon is much different from the multi-photon absorption treated within the perturbative theory. The laser works not as a photon but rather as an electric field and tilts the Coulomb potential for the electron. Then, the electron wave function in the atom penetrates the same energy in the continuous state, i.e. a tunneling process occurs. The ionized electrons gain kinetic energy from acceleration by the laser electric field in free space, as shown at the second step in Fig. 1.2. The electrons are approximated to be free of Coulomb interaction from the parent ion in this process. When the direction of the electric field reverses in the next half cycle of the laser, the electrons are accelerated back to their original atomic site and recombine with the parent ion. The electrons then release the kinetic energy gained from the acceleration and produce the harmonic emission. Since these processes are repeated twice for every laser cycle, the spectrum of light has only frequencies that are integer multiples of the driving laser. This is nothing but the HHG. The three-step model reproduces the relation in eq. (1.7), considering that the maximum kinetic energy that an electron can acquire from the laser electric field corresponds to the cutoff energy. The higher harmonics in Fig. 1.2 have only odd-order peaks, which is due to the inversion symmetry of atomic gases [28].

The three-step model is semiclassical and does not incorporate quantum mechanical interference effects. However, M. Lewenstein et al. later vouched for the validity of this three-step model using a quantum mechanical model [29]. They used the time-dependent Schrödinger equation (TDSE) to consider the time evolution of the dipole moment created by the electron. By applying the strong field approximations, they found that the saddle point solution corresponds to the semiclassical three-step model.

According to eq. (1.7), the cut-off energy is proportional to the intensity of the laser and the square of the wavelength (inverse square of the frequency). A stronger, longer wavelength laser electric field can provide more kinetic energy to the electrons. Thus, a driving electric field in the mid-infrared was used to obtain harmonics in the x-ray region [26]. Also, the generation of ultra-broadband light allows us to obtain light pulse with attosecond time duration when the chirp of the bursts generated by the electron recombination process is carefully compensated [25]. Thus, pump-probe spectroscopy using the HHG source allows us to study electron dynamics with attosecond time resolution [25].

HHG has also been observed in molecular systems, where ionization and recombination processes occur in multiple atomic sites [30]. The molecular systems have richer dynamics than atoms due to the presence of internal degrees of freedom. In this context, there are many attempts to use harmonic generation itself as a spectroscopic tool, e.g., the imaging of molecular orbitals and the resolving charge migration in attosecond time scale [31, 32]. Furthermore, HHG has also been observed in various solids and a few liquids [33, 34]. In the next section, we will introduce the current status of the study on solid-state HHG.

1.2.3 High harmonic generation in solids

The generation of higher harmonics has also been observed in solids. However, there is an experimental difficulty that is different from that of atomic gases: damage to the sample in a strong electric field. In particular, irradiation with intense visible or near-infrared

light resonates with the electronic excitation of semiconductors, resulting in significant absorption and destruction of the material by laser ablation [35].

Harmonics up to the seventh order were observed in a semiconductor ZnSe using mid-infrared femtosecond pulses with central wavelengths between 3 μm and 6 μm in the pioneering work by A. H. Chin et al. in 2001 (Fig. 1.3) [36]. The frequency of mid-infrared light is so low for semiconductors that even intense light does not destroy them. The intensity range realized in Fig. 1.3 was sufficient to reach the nonperturbative regime although the nonperturbative nature was not confirmed in their study. Ten years later, S. Ghimire et al. observed higher harmonics up to the 25th order in bulk ZnO by irradiating it with mid-infrared pulses at a wavelength of 3.25 μm, confirming the nonperturbative intensity dependence for the first time [37].

They reported a considerably different nature of HHG in solids from that of atoms due to their high electron densities and periodic crystal structures. When the cutoff is defined as the maximum order of the observed high harmonics, the cutoff increases linearly with the electric field of the incident pulse. This is much different from the HHG of atomic gases, where the cutoff energy increases in proportion to the square of the electric field (in proportion to the ponderomotive energy). They also observed anisotropic HHG reflecting the crystal structure and even-order harmonics due to the broken inversion symmetry. The dependence of the HHG intensity on the ellipticity is also different from that of the atomic case. When the ellipticity of the incident light increases, the harmonic generation efficiency decreases rapidly in atomic gases. This is because the accelerated electrons in free space cannot return to their parent ion under a circularly polarized laser field. In ZnO, the decrease in HHG intensity is slight even when the ellipticity of the incident light increases. These facts indicate that there is an HHG mechanism unique to solids.

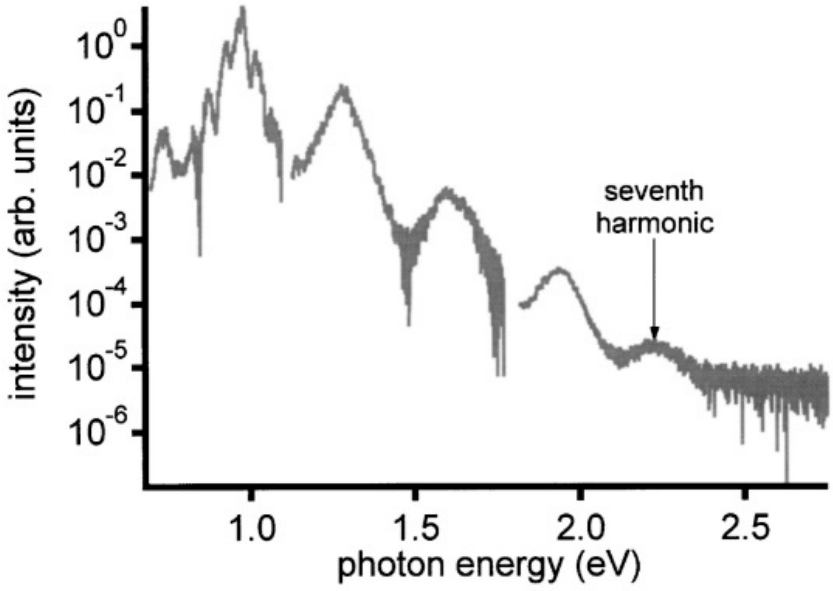

Figure 1.3: High harmonic generation spectra obtained from ZnSe using mid-infrared pulses with the wavelength of 3.9 μm and pulse width of 200 fs. Reprinted figures with permission from Ref. [36]. Copyright 2001 by American Physical Society.

HHG in solids has recently been observed in various semiconductors and insulators such as GaSe, SiO_2, glass, Si, GaAs, MgO, Sapphire, rare gas solids, and monolayer MoS_2. [12, 36–55]。 In recent years, it has also been observed in metals, graphene, three-dimensional Dirac semimetals, Weyl semimetals, the surface of topological insulators, and strongly correlated electron systems. [56–65] However, the origin of HHG in solids remains a subject of debate.

Mechanism of high harmonic generation in solids

A number of theoretical studies have treated light-driven coherent electrons and holes to describe the mechanism of HHG [33]. In semiconductors, two distinct sources of the high harmonics are proposed, intraband and interband mechanisms. Figure 1.4 shows the schematics of these mechanisms in the sub-cycle timescale of the laser field. The mechanism of HHG in solids are described in both momentum (k) -space (Fig. 1.4 (a)) and real space (Fig. 1.4 (b)). This mechanism is understood in terms of the three-step mechanism similar to that in atomic gases:

1. Electron-hole pair creation in conduction and valence bands through a tunneling process
2. Intraband acceleration of the electron-hole pair
3. Recombination of the electron and hole

When a semiconductor is irradiated with an intense non-resonant driving field, a tunneling process occurs and electron-hole pairs are generated efficiently near the band edge (Fig. 1.4(1)) [66]. The intense field then drives the electron-hole pairs into a higher energy region (Fig. 1.4(2)). In this process, the wavevector of the generated electron-hole pairs are written as

$$\dot{k}(t) = \frac{q}{\hbar}E(t), \tag{1.9}$$

where q is the charge of electron or hole, and $E(t)$ is the incident electric field. The corresponding real space dynamics is written by

$$\dot{r_n} = \frac{1}{\hbar}\nabla_k \varepsilon_n(k), \tag{1.10}$$

where n is the band index and $\varepsilon_n(k)$ is the energy of the band structure [8]. The right-hand side of eq. (1.10) represents the group velocity for electron wave packet in the n-th band. When electrons and holes reach the high energy region in the band structure, the effective mass changes due to the deviation from the parabolic band structure. As a result, electron-hole pairs move nonlinearly in real space due to intra-band transitions and emit light. This is the intraband mechanism, which is not present in atomic gases. The oscillation of electron wave packet in a static external electric field is called Bloch oscillation. In contrast, in the AC external field of a laser, it is called dynamical Bloch oscillation (Fig. 1.4(2)) [8, 37, 38]. In addition, in real space, electrons and holes re-collide and recombine. Thereby the kinetic energy of the electron-hole pair is emitted (Fig. 1.4(3)). This is called the interband mechanism, and is analogous to the three-step model for atomic gases [40, 67]. These emission processes produce sub-cycle bursts that repeat at the same period as the laser field. This results in a spectrum with clear harmonic peaks.

G. Vampa et al. derived this picture in 1994 by developing a theory using saddle point analysis similar to that of M. Lewenstein et al. for Bloch wave function in solids [29, 67]. Figure 1.5 shows an example of harmonic spectra calculated by considering intraband and interband mechanism by G. Vampa et al.. According to their study, harmonics above the bandgap energy are mainly generated by the interband mechanism in an MIR field. On the other hand, the intraband mechanism largely contributes to lower-order harmonics. Note that the interband and intraband mechanisms interfere with each other. Higher-order intraband harmonic spectra are attributed to interband transitions, as described in Ref. [68].

The physical picture in a strong field depends on the gauge of the electromagnetic field and the basis for the electronic state. The above picture of an electron-hole pair moving through k-space is for the case where the Houston basis and the length gauge are selected. [69–71]. Although the above picture focuses on the lowest two bands, we can extend this interpretation to multi-band systems [39, 54].

There are several schemes for theoretically analyzing HHG in solids. Recent theoretical works mainly focus on time domain approach, such as time dependent Schrödinger equation [69], semiconductor Bloch equation（density matrix approach）[67, 72], and time dependent density functional theory [73, 74]. On the other hand, a complementary approach using Floquet theorem has long been attempted [75–77].

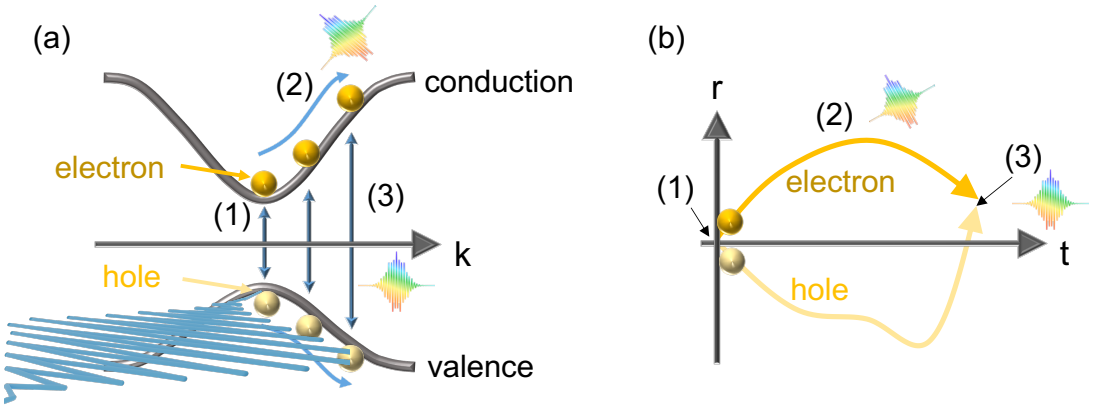

Figure 1.4: Three-step mechanism of HHG in semiconductor. (a) The dynamics of electron wave packet in k-space and (b) the one in k-space. (1) Tunneling (2) Intraband acceleration (3) Recombination.

Experimental studies of high harmonic generation in solids

Many experiments have observed HHG in semiconductors and insulators. There are mainly two categories: those focusing on the harmonics in the infrared to visible range and those focusing on the ultraviolet to high-frequency side. In all the experiments using MIR excitation pulses, the peak intensity of the pulse was around 1 TW cm^{-2} and the pulse duration was several tens of femtoseconds. O. Schubert et al. irradiated semiconductor GaSe with mid-infrared light and observed HHG up to the 23rd order in the visible

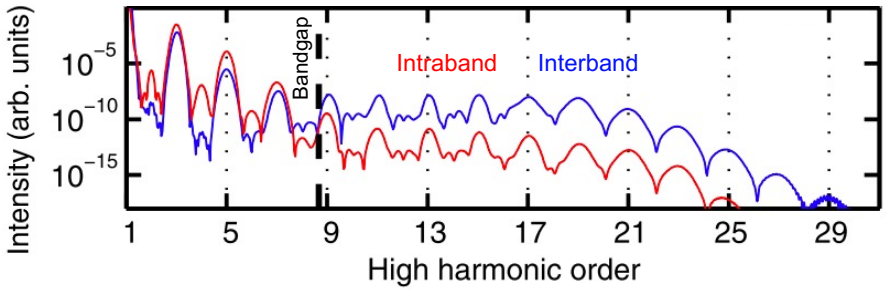

Figure 1.5: Example of calculated harmonic spectrum from interband (blue line) and intraband (red line) currents considering the lowest two bands of ZnO. The driving laser field has a temporal Gaussian envelope with a FWHM equal to 10 cycles and cosine carrier with a laser period of T_0. The dephasing time of $T_2 = T_0/4$ is introduced to obtain clear spectral peaks. The dashed black vertical lines represent the (minimum) band gap at the center of the Brillouin zone. Reprinted figures with permission from Ref. [67]. Copyright 2014 by American Physical Society.

region [38]. They reported that the frequency of HHG shifts when the carrier-envelope phase (CEP) is changed, which is unrelated to HHG in perturbation theory. In addition, they succeeded in reproducing the spectrum of HHG by full quantum numerical calculation. G. Vampa et al. controlled the real-space motion of electrons by simultaneously irradiating a driving field with the frequency of ω and a weak field with the frequency of 2ω, and manipulating their relative phases. They found the resulting interferogram was very similar to that obtained for gaseous atoms and revealed the recombination dynamics of electron-hole pairs [40, 78]. T. T. Luu reported the appearance of HHG with a plateau structure above 20 eV in the extreme ultraviolet region by applying ultrashort pulses of 1.5 cycles with frequencies ranging from near-infrared to visible range to SiO_2 [39]. M. Hohenleutner et al. experimentally performed real-time measurement of high harmonics from GaSe using electric optical sampling. They observed a sequence of subcycle bursts that coincides in time with the electric field crests of one polarity of the driving laser waveform. In addition, their numerical calculation revealed the interference of electronic transitions between multiple bands [41]. Garg et al. generated high harmonics up to the extreme ultraviolet region and measured the photon energy of the emitted bursts in real time using attosecond streaking and found that the intraband mechanism was the main source [12, 51]. G. Ndabashimiye et al. observed HHG in van der Waals solids Ar and Kr, and showed the multiple plateaus, which are not observed in atomic systems [42]. Later theoretical studies suggested that the starting energy of the second plateau corresponds to the bandgap energy of the second conduction band [79]. Y. You et al. reported that the excitation polarization dependence of HHG in MgO is clearly different between the perturbative and nonperturbative regimes, and the dependence on the ellipticity of the excitation light shows anisotropy reflecting the interatomic coupling with respect to the crystal orientation. They also reported that the intensity of HHG in the case of circularly polarized excitation is comparable to that in the case of linearly polarized excitation [43]. N. Yoshikawa et al. and A. Uzan et al. showed that the joint density of states can qualitatively explain the order dependence of the harmonic intensity [52, 54]. The above studies

have mainly focused on single-electron dynamics to reveal the electronic state in a strong field.

Application of high harmonic generation in solids

HHG can be used as a spectroscopic technique to reveal the electronic structure in solids reflecting the abovementioned dynamics, which is called high harmonic spectroscopy. For example, Luu et al. described HHG from SiO_2 using the intraband model and showed that within the scope of that model, the band structure can be extracted from the order dependence of the spectrum [39]. Vampa et al. also claimed that the band structure can be reconstructed by finding a trial band structure from a numerical simulation that reproduces the interferogram measured in a two-color laser field [80]. H. Liu et al. pointed out that Berry curvature contributes to even-order HHG [44], and T. T. Luu et al. used HHG to reconstruct the Berry curvature [34]. H. Lakhotia pointed out that valence electron density can be obtained with a picometer-scale spatial resolution by considering the semiclassical motion of electrons in the valence electron potential in real space [43, 55]. As described above, HHG also attracts attention to probe electronic structures without an external field. Furthermore, HHG in solids is also promising for compact extreme ultraviolet light sources. Several researchers fabricated nanostructures on semiconductors to give them functionality as light sources that cannot be realized in gases [48, 81–84].

Current subject of study on high harmonic generation in solids

As described in the above sections, HHG in solids has been studied intensively in recent years, and the mechanism has been gradually clarified. However, the understanding of HHG is not straightforward because the dynamics have a large energy scale compared to the elementary excitations in typical solids. In addition, the nature of HHG is highly dependent on the target solid. Moreover, although the physical picture based on the single-active electrons approximation is often used to describe HHG, many-body effects also affect the dynamics of single electrons. Although the many-body effect has been discussed phenomenologically, its influence on HHG has not yet been clarified [38, 41, 67]. Therefore, a comprehensive understanding of HHG in solids is a crucial and currently challenging goal.

High order sideband generation in solids

There are studies to understand electron dynamics by preparing an additional laser pulse to control the electron dynamics in a strong field. B. Zaks et al. performed an experiment in which they irradiated a GaAs quantum well with intense terahertz (THz) light and weak near-infrared (NIR) light with the photon energy of exciton resonance. Exciton is a quasiparticle in solids, where electrons and holes are bound by the attraction of Coulomb interactions to form a hydrogen atom-like state. They found that the radiation occurs in the frequency interval of THz light around the frequency of NIR light [85]. This phenomenon is called high order sideband generation (HSG). It has been found that HSG can be observed by using MIR light instead of THz light [86]. The frequency of the sidebands can be written as

$$\omega_{HSG} = n\omega + \omega_{NIR}, \quad (n\text{: integer}) \tag{1.11}$$

where ω_{HSG} is the angular frequency of the sidebands and ω is that of the strong MIR or THz laser and ω_{NIR} is that of the NIR light. In this material, the exciton binding energy is large due to the quantum confinement in the quantum well structure. HSG can also be observed in bulk GaAs where the exciton binding energy is not large [87]. Figure 1.6 shows an HSG spectrum obtained from a GaAs sample with a quantum well structure under near-infrared and THz light field [88]. Since the sidebands with $n < 0$ are associated with perturbative nonlinear optical processes, the study of nonperturbative optics has focused on the sidebands with ($n > 0$).

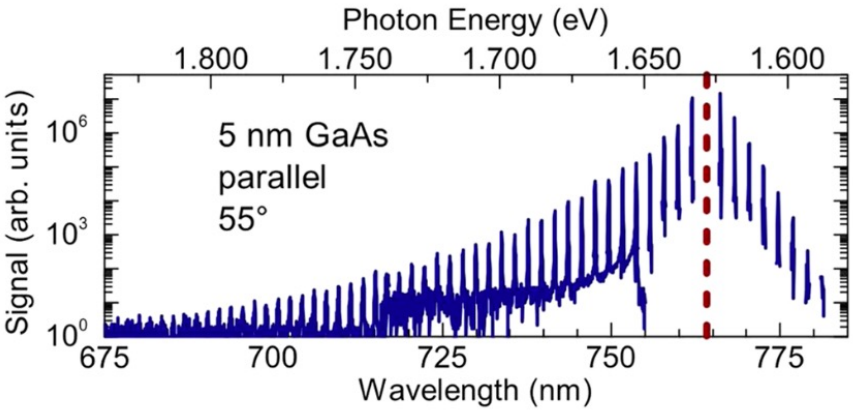

Figure 1.6: High order sideband generation spectrum spanning 106 orders from the 5-nm GaAs sample with a quantum well structure. The red dashed line represents the wavelength and photon energy of the near-infrared (NIR) light. The NIR and THz laser polarizations are parallel to each other, and the [011] direction of the lattice makes a 55° angle with the THz polarization. Reproduced from H. B. Banks *et al.*, Physical Review X **3**, 137 (2017). ©2017 The authors. Distributed under a Creative Commons Attribution 4.0 International license (CC BY 4.0) [88].

The HSG mechanism is understood in terms of a similar mechanism to the three-step model in HHG as shown in Fig. 1.7.

1. Resonant excitation of electron-hole pairs (excitons) by NIR light
2. Intraband acceleration of electron-hole pair by strong THz (or MIR) light
3. Recombination of the electron and hole

This model replaces the step of electron-hole pair creation by strong laser field in HHG with a resonant interband transition induced by near-infrared light [13, 85, 86, 88, 89]. The advantage of HSG is that separate light pulses can control the generation and acceleration of the electron-hole pair, allowing us to understand the underlying dynamics of HHG. In this model, since the interband polarization of electron-hole pairs encodes the information of the NIR light frequency, the HSG mechanism corresponds to the interband mechanism of HHG.

F. Langer et al. manipulated the generation time of electron-hole pairs for a strong field on a sub-cycle time scale by using NIR light pulses that are short enough for one

cycle of MIR light. They found the importance of the electron-hole recollision dynamics by experimentally selecting the trajectory of the electrons and holes [86].

Similar to HHG, HSG can also be used as a spectroscopic tool. For example, it is argued that it can probe the band structure, Berry curvature, and even the Bloch wave function in semiconductors. [88, 90, 91]. Moreover, HSG was applied to demonstrate the lightwave valleytronics [13].

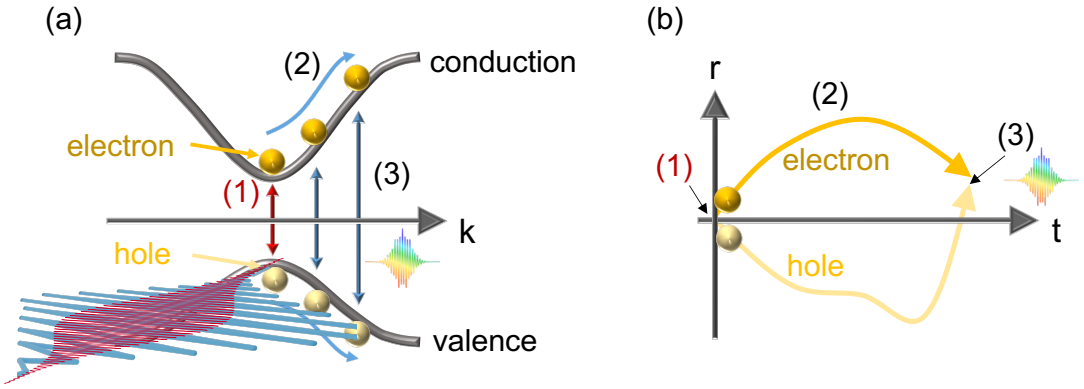

Figure 1.7: Three-step mechanism of high order sideband generation in semiconductor. (a) The dynamics of electron wave packet in k-space and (b) the one in k-space. (1) Tunneling (2) Intraband acceleration (3) Recombination.

1.3 Dynamical symmetry in Floquet system

In this section, we introduce the historical background of dynamical symmetry. Dynamical symmetry (DS) is a symmetry class defined in the product space of real space and time. It is a concept that has the potential to describe the symmetry of periodically driven systems in general [28, 92–100]. The physical understanding of periodically driven systems has been developed recently using the Floquet theorem. The Hamiltonian of a time-periodically driven system with the period of T satisfies

$$H(t) = H(t+T). \tag{1.12}$$

Here, the interacting laser fields are assumed to be completely periodic. The Floquet theorem, a temporal analog of the Bloch theorem in solid-state physics, allows us to analyze a dynamic problem as an eigenvalue problem. For example, its application to transport problems, magnetic and other strongly correlated electron systems, and electron-phonon systems have advanced our understanding of the non-equilibrium dynamics in periodically driven systems [18]. Another interesting direction is the engineering of band topology using periodic external fields and their classification [19, 20]. Experimental studies have been carried out mainly on cold atoms but also photonics and solid-state systems [20]. In particular, the generation of Floquet Bloch bands and the observation of light-induced anomalous Hall effects in solids have been realized by sub-picosecond MIR pulse lasers [101, 102]. The Floquet concept is currently receiving a great deal of attention in both theoretical and experimental studies.

Recently, DS (sometimes called space-time symmetry) has been formulated as a symmetry class unique to the Floquet state [98]. For example, the combinations of time translation, time reversal, spatial rotation, mirroring, etc., are included in this symmetry class. The first theoretical idea was proposed in 1993 by N. Ben-Tal et al. to describe the polarization selection rule of HHG in atomic gases [28]. They described a selection rule in which linear polarization in parallel with excitation polarization appears only at odd orders. In 1997, Ofir E. Alon et al. showed that DS can derive a selection rule for circularly polarized light in the system with discrete rotational symmetry [92]. After Tong et al. theoretically proposed two-color laser field can generate circularly polarized harmonics from atomic gases [103], O. E. Alon et al. explained its principle with the same DS [93]. Circularly polarized HHG from atomic gases was experimentally confirmed in a two-color laser field by A. Fleischer et al. in 2014 [104]. In the following year, its circular polarization selection rule was confirmed and found to be consistent with that predicted from DS [95]. In 2017, N. Saito et al. showed that circularly polarized harmonics can be generated in a single MIR driving field in bulk GaSe, a crystalline solid with three-fold rotational symmetry, and explained it with DS [105]. DS is useful for aspects other than HHG. The Floquet Bloch band, which was experimentally observed in the surface state of a topological insulator, was shown to be protected by DS [94, 101]. In addition, DS is used for the classification of the topological phases [96, 97]. In 2019, O. Neufeld et al. formulate DS as Floquet group theory [98]. O. Neufeld argued that DS can be applied to any periodic external field with any complex temporal profile and any system of gases, molecules, or solids. This allows us to treat polarization selection rules of HHG in a general way. Detailed theoretical formalism is explained in Section 2.1 and 2.2

Although DS is an extremely promising concept, it has not been fully verified experimentally. In particular, the validity of DS is non-trivial in solids since the dissipative processes, and the effects of carrier accumulation during strong field irradiation to semiconductors may break the DS. This is further explained by using a model of a two-level system in Section 2.3. Here, we show how the temporal periodicity of the electron dynamics appears in HHG. In the case that the electron dynamics are periodic, the sub-cycle burst emitted by the electron in the HHG process is repeated with the same period as that of the driving laser field (orange line in Fig. 1.8(b)). Consequently, the emission forms a harmonic spectrum with the same spacing between peaks, as shown in Fig. 1.8(c). On the other hand, suppose that the electron dynamics in the second half of the MIR pulse is changed due to the carrier accumulation, and the timing of the emission is shifted. In this case, the spectral peak is also shifted, as shown is also shifted, as shown by the green line in Fig. 1.8(c). This spectral shift has been confirmed in graphene, which indicates the carrier accumulation can break the temporal periodicity of the electron dynamics under a periodic light field.

To experimentally verify whether such symmetry holds in a strongly light-driven solid, one should examine the polarization selection rule of HHG. For this purpose, it is desirable to remove the effect of the propagation effect described in the next section since the propagation effect may obscure the selection rule [98].

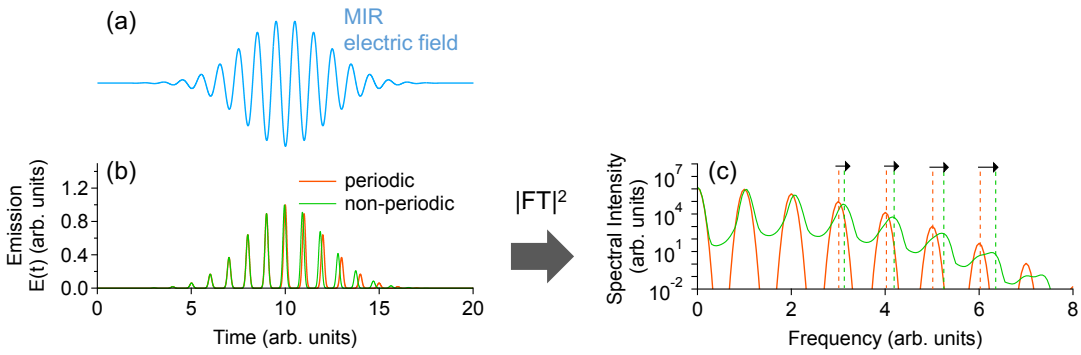

Figure 1.8: Time-periodic emission in the time domain and frequency domain. (a) Schematic diagram of the time profile of the electric field of a mid-infrared (MIR) pulse. (b) Example of a sub-cycle burst that repeats with the same period as that of the laser electric field during the pulse duration (orange line). The green line represents the aperiodic case. The timing of the bursts of the green line is set to be earlier than the orange line in the second half of the MIR pulse. (c) Spectral intensity of the burst calculated by the square of the magnitude of the Fourier transformations for the orange and green lines in (b).

1.4 High harmonic generation in monolayer transition metal dichalcogenides

This section introduces monolayer transition metal dichalcogenides (TMDs), which are ideal samples to avoid the propagation effect. First, we explain the propagation effect and then explain the basic properties of monolayer TMDs. We also introduce several experimental studies of HHG and HSG in monolayer TMDs.

1.4.1 Propagation effect on high harmonic generation in solids

In all experimental studies until 2018, HHG measurements in bulk crystals were performed in the transmission configuration shown in Fig. 1.9. In this configuration, the intensity of the harmonics is modulated according to Maxwell's equations as they propagate through the bulk samples. For example, it is necessary to consider the effect of reabsorption of generated harmonics and the phase-matching condition, which has always been considered in conventional nonlinear optics [106]. The phase-matching condition defines the conditions for the constructive interference of harmonics that are gradually generated within the thickness of the sample. It is essential for optimal generation of high harmonics in gaseous media [25]. It has been investigated in previous studies that such a propagation effect has a significant impact on HHG spectra in solids [50, 107, 108]. G. Vampa et al. and P. Xia et al. compared the spectra of HHG emitted on the reflection side with that emitted on the transmission side [50, 108]. They observed considerable spectral broadening in the spectrum obtained on the transmission side, which was attributed to the self-phase modulation. P. Xia et al. also showed that the efficiency and orientation

dependence of HHG appearing on the transmission side depended on the sample thickness [50]. It is desirable to remove the propagation effect for microscopic understanding, which depends on the macroscopic shape of the crystal.

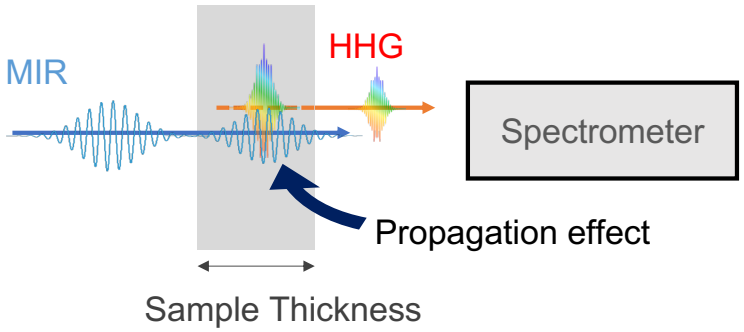

Figure 1.9: Schematic setup for HHG measurement in transmission geometry and propagation effect

1.4.2 Basic properties of monolayer transition metal dichalcogenides

The study of atomically thin layer began with the successful exfoliation of graphene by Nobel prize winners, Novoselov et al. [109]. Graphite is a kind of van der Waals layered material, in which two-dimensional sheets are bound together by weak van der Waals forces. In contrast to the semi-metallic property of graphene, the next monolayer thin films discovered in van der Waals layered materials were semiconducting transition metal dichalcogenides (TMDs) such as MoS_2 [110–112].

This group is represented by the composition formula MX_2 (M=Mo,W, X=S,Se). Figs. 1.10(a) and (b) shows the crystal structure of monolayer transition metal dichalcogenides. These materials have honeycomb lattice structures as shown in Fig. 1.10(a). The crystal axis indicated by black arrows is called zigzag (M-M) and armchair (M-X) direction. Figure 1.10(b) shows the structure of the sample viewed from a direction parallel to the layer, where the M atoms are sandwiched between the X atoms on the top and bottom. The inversion symmetry of the crystal is broken, and the crystal point group belongs to D_{3h}. The K and K′ points in the corresponding hexagonal Brillouin zone are inequivalent due to the broken inversion symmetry.

Since the optical properties of monolayer MoS_2 were investigated in 2010 [113,114], a considerable number of studies have been carried out, and their fundamental optical properties have been well understood in the last decade. One of the reasons why monolayers have attracted so much attention is that they exhibit unique optical properties. Although bilayer or more multi-layer TMDs are indirect-gap semiconductors, the monolayer TMDs have direct gaps at the K and K′ points. According to first-principle calculations, the electronic bands near the bandgap consist mainly of d-orbitals of M atoms, with a small contribution of p-orbitals of X atoms [115]. The exciton dominates the optical properties at the band edge in this material. In monolayer TMDs, the quantum confinement to two-dimensional space and the reduced dielectric screenings cause strong Coulomb interaction between electrons and holes [116]. That forms Wannier-Mott excitons with the exciton

binding energy of several hundred meV that are stable at room temperature [112]. In addition, since the valleys at K and K′ points are not equivalent, there is a valley degree of freedom. This valley degree of freedom can be used as an information carrier in valleytronics, which is expected to be the next generation of electronics. In addition, the presence of large spin-orbit interaction causes the coupling of spin and valley degrees of freedom, and the energy of the spin-up and spin-down states of the valence band is split by about 100 meV [110,117]. As a result, there are absorption peaks for excitons corresponding to each band in the absorption spectrum. Figure 1.11(a) shows the band structure of monolayer MoS_2 [118]. Excitons in the lowest bandgap are called A excitons; excitons in the higher energy side of the energy split are called B excitons. These exciton peaks appear in absorption spectra obtained from four monolayer TMDs (Fig. 1.12(b)). The energy position of the peaks in each material is slightly different from other materials [52, 118]. The absorption peaks indicated by C, D are called the C, D band, respectively, which are the van Hove singularity points where the conduction band and valence band are parallel (denoted by blue arrows in Fig. 1.11). The K and K′ valleys have a valley-dependent circular polarization selection rule for optical transitions: the K (K′) valley couples only to circularly (counter-circularly) polarized light. Consequently, circularly polarized light irradiation can induce valley polarization. It can cause characteristic phenomena such as circularly polarized photoluminescence and valley hall effect [119–122]. Monolayer TMDs have also been studied as a field where many-body effects occur due to strong Coulomb interactions, e.g., formation of trion and biexciton [123], exciton-exciton annihilation [124], and bandgap renormalization [125].

As shown above, a variety of optical properties of monolayer TMDs have attracted attention and have been well investigated. Therefore, in addition to avoiding propagation effects, this material provides an ideal platform to study the details of the HHG mechanism.

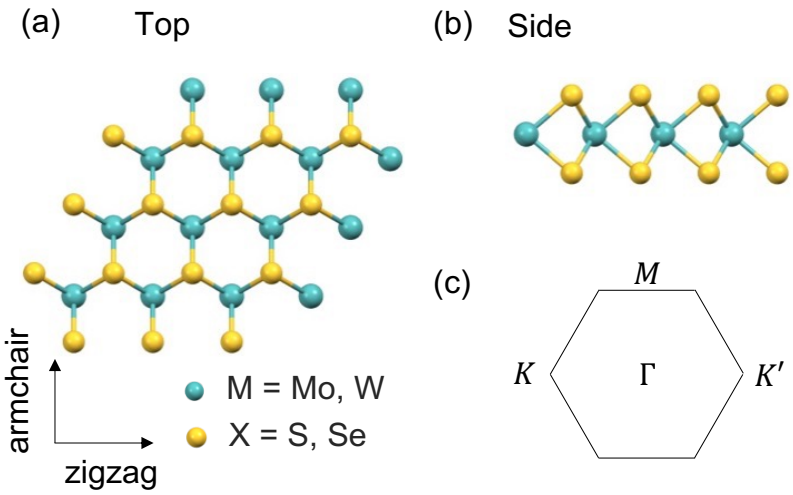

Figure 1.10: (a) Top view and (b) side view of the crystal structure and (c) Corresponding first Brillouin zone of monolayer transition metal dichalcogenides.. The black arrows represent the zigzag and armchair direction.

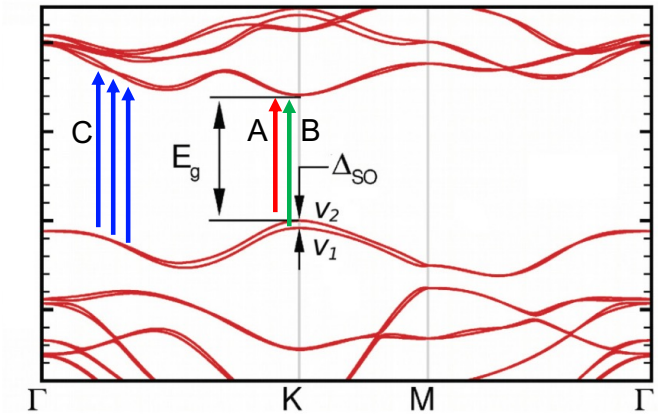

Figure 1.11: Typical band structure for an MX_2 monolayer (calculated using density functional theory for MoS_2). The valence-band maximum is split due to spin-orbit coupling. Transitions between V_2 and the conduction-band minimum at K lead to A-excitons in the absorption spectrum (red arrow), while transitions between V_1 and the conduction-band minimum at K lead to B-excitons (green arrow). The blue arrows represent the band nesting region called C band. Reprinted figures with permission from Ref. [126]. Copyright 2012 by the American Physical Society. Partially modified from the original figure.

1.4.3 High order harmonic and sideband generation in monolayer transition metal dichalcogenides

Monolayer transition metal dichalcogenides are studied as an experimental platform for HHG and HSG. H. Liu et al. reported the first experimental observation of HHG from monolayer TMDs [44]. The even-order harmonics were observed in monolayer TMDs due to the broken inversion symmetry. They explained the harmonic spectra with the intraband model considering Berry curvature [44]. On the other hand, N. Yoshikawa et al. observed the C band resonance in the order dependence of the harmonic intensity and explained it with the interband model [52].

F. Langer et al. observed HSG from monolayer WSe_2 [13]. They create the electron-hole pairs using a NIR pulse resonant with the A-exciton energy. They investigated part of the linear polarization selection rules of HSG and explained it with three-step like dynamics of electron-hole pairs. They succeeded in understanding the polarization selection rules in terms of the symmetry of the dynamics in k-space. However, the selection rules have not been explained by a more general approach: DS.

1.5 Purpose and composition

As described in the previous sections, nonperturbative interaction of electrons in solids with a strong mid-infrared laser electric field induces various coherent dynamics of electrons and creates novel electronic states that cannot be understood in the framework of perturbation theory. The emergence of such electronic states leads to the discovery of ex-

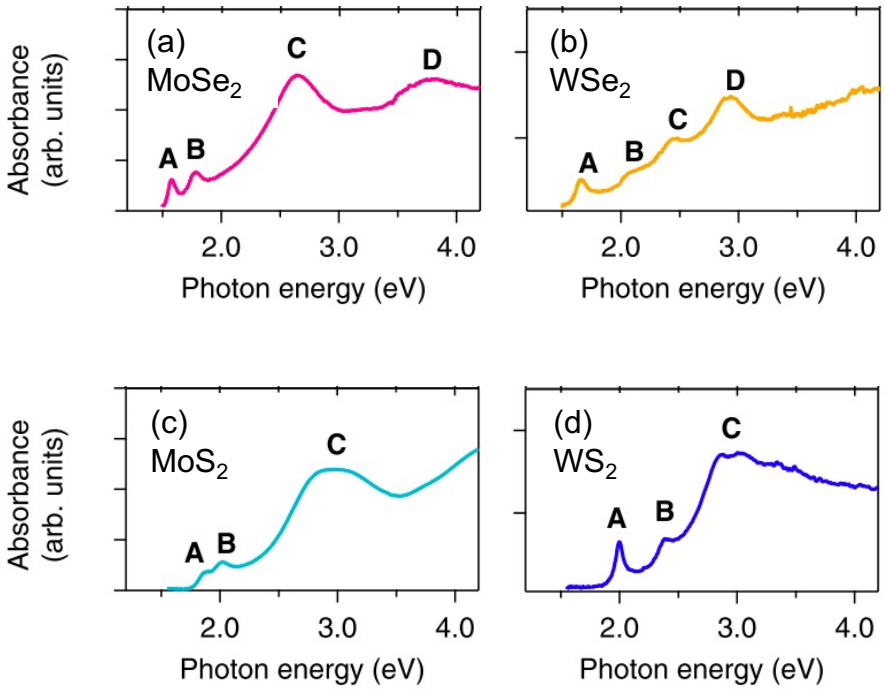

Figure 1.12: Optical absorption spectra of the (a) $MoSe_2$, (b) WSe_2, (c) MoS_2, and (d) WS_2 monolayers. monolayers at room temperature. The peaks of the A and B excitons are labeled A and B, respectively. The peaks due to the band nesting effects are labeled C and D. Reproduced from N. Yoshikawa *et al.*, Nature Communications **3**, 137 (2019). ©2019 The authors. Distributed under a Creative Commons Attribution 4.0 International license (CC BY 4.0) [52]. Partially modified from the original figure.

otic material functionalities, the development of ultrafast electronics, and ultrafast quantum control for future electronic and optical devices. High harmonic generation (HHG), which converts low-energy photons into visible and ultraviolet light, is the most straightforward and powerful way to study the nonlinear electronic response in strongly light-driven solids. Most of the studies on HHG in solids have explained the mechanism in terms of coherent electron and hole dynamics driven by light in k-space. However, research to further our understanding of microscopic electronic states is still being vigorously pursued. Under intense laser fields, highly non-equilibrium states are realized, and their typical energy scales are much larger than the fundamental excitations in solids. and they are accompanied by many-body interactions, which makes their understanding extremely difficult. Furthermore, it has been experimentally shown that the properties of HHG strongly depend on the material and its macroscopic structure, which causes microscopic physical understanding challenging. Therefore, in this research field, it is crucial to clarify the microscopic and general physics governing the properties of strongly light-driven systems.

This thesis studies dynamical symmetry (DS), a general concept for strongly light-driven electronic systems, in solids. DS has been formulated as a group theory and applied for polarization selection rules for HHG. However, the validity of DS in solids remains non-trivial since many-body processes or accumulation of excited carriers during the application of strong infrared pulses can break the time-periodicity of electron dynamics. Two experiments were carried out to understand the validity of DS in solids. Atomically thin semiconductors were used for the experimental samples to remove the influence of propagation effects. In both experiments, information on the electronic state under strong laser fields was obtained by further irradiating the system with a relatively weak near-infrared pulse. First, we explored the validity of DS in the polarization selection rules of higher-order sideband generation (HSG) in semiconductors. This is a nonperturbative higher-order sum-frequency generation process in solids that occurs when weak near-infrared light pulses and strong mid-infrared light pulses overlap in time (Fig. 1.13(a)). Next, to understand the effect of accumulated incoherent electron-hole pairs and many-body interaction in HHG, we performed an experiment in which incoherent photo-carriers were prepared by irradiating near-infrared pulses before the MIR pulse irradiation (Fig. 1.13(b)). The composition of this thesis is summarized in Fig. 1.14.

In Chapter 2, we introduce the recently formulated theory of DS. In Chapter 3, we determine the polarization selection rules of HSG in a monolayer of MoS_2, a kind of TMD, both experimentally and theoretically. In the experiments, we systematically determined the polarization selection rules for circular and linear polarization by controlling the polarization of near-infrared and mid-infrared pulse and measuring the spectra with resolving the sideband polarization. To explain these selection rules, we constructed a theoretical framework using DS. In Chapter 4, we studied the effect of incoherent electron-hole pairs accumulated when a semiconductor is irradiated with intense infrared pulses. Specifically, we investigated the effect of photo-carrier doping on HHG in monolayer WSe_2. Numerical simulations were performed to clarify the mechanism underlying HHG. In Chapter 5, we summarize this thesis and discuss future prospects.

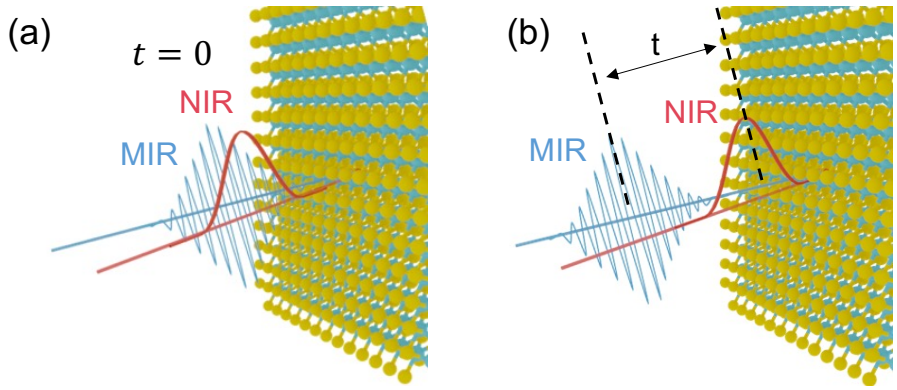

Figure 1.13: Schematics of experimental configuration in this thesis. (a) Schematics of setup for high order sideband generation. The time delay between near-infrared (NIR) and mid-infrared (MIR) pulses are set to 0. (b) Schematics of setup for incoherent photo-carrier doping for high harmonic generation. The time delay is set to be long enough for photo-carriers doped by the NIR pulse to lose their interband coherence due to dephasing process before the MIR pulse arrives.

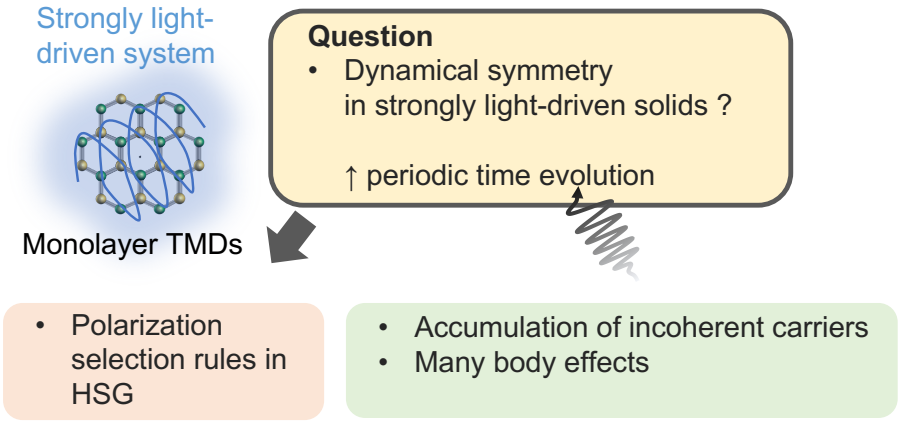

Figure 1.14: Composition of this thesis.

Chapter 2

Dynamical symmetry and high harmonic generation

In this Chapter, we introduce the theoretical formalism of DS and explain its connection to HHG selection rules and electron dynamics under strong fields with some examples. In Section 2.1, we introduce the basics of the Floquet theorem. In Section 2.2, we explain the theoretical formalism of DS and its application for HHG selection rules. In Section 2.3, we discuss the electron dynamics under a strong light field with calculation examples in a two-level system.

2.1 Floquet theorem

In this section, we introduce the basics of Floquet theorem [16, 17, 127, 128]. The Hamiltonian of a time-periodically driven system with period T satisfies

$$H(t) = H(t+T). \tag{2.1}$$

The Schrödinger equation is given by

$$\left(H(t) - i\hbar\frac{\partial}{\partial t}\right)|\Psi(t)\rangle = 0, \tag{2.2}$$

where $|\Psi(t)\rangle$ is the wave function. According to the Floquet theorem, the solution of eq. (2.2) is generally given by

$$|\Psi_\alpha(t)\rangle = \exp(-i\varepsilon_\alpha t/\hbar)\,|\Phi_\alpha(t)\rangle \tag{2.3}$$

$$|\Phi_\alpha(t)\rangle = |\Phi_\alpha(t+T)\rangle\,, \tag{2.4}$$

where ε_α is quasienergy (a real number) and $\Phi_\alpha(t)$ is a Floquet state. The operator in the left-hand side of eq. (2.2) is a Hermitian operator defined as Floquet Hamiltonian

$$H_F = H(t) - i\hbar\frac{\partial}{\partial t}. \tag{2.5}$$

One finds the following equation:

$$H_F\,|\Phi_\alpha(t)\rangle = \varepsilon_\alpha\,|\Phi_\alpha(t)\rangle\,. \tag{2.6}$$

The Floquet state can be represented in terms of a discrete Fourier series with frequency $\omega = \frac{2\pi}{T}$:

$$|\Phi_\alpha(t)\rangle = \sum_m \exp(-im\omega t)\,|\Phi_\alpha^m\rangle\,. \tag{2.7}$$

Hamiltonian is also expanded to discrete Fourier series

$$H(t) = \sum_m \exp(-im\omega t) H^m. \tag{2.8}$$

By using these equations, eq. (2.6) can be transformed into

$$\sum_m \left(H^{(n-m)} - m\omega\delta_{mn}\right)|\Phi_\alpha^m\rangle = \varepsilon_\alpha\,|\Phi_\alpha^n\rangle\,. \tag{2.9}$$

Note that the periodic dynamics can be treated by solving the diagonalization problem eq. (2.9), which does not explicitly include time. The definition of quasienergy is one that needs attention. When $\Phi_\alpha(t)$ is an eigenfunction of eq. (2.6), the following function is also the eigenfunction:

$$|\Phi_{\alpha'}(t)\rangle = \exp(in\omega t)\,|\Phi_\alpha(t)\rangle \equiv |\Phi_{\alpha,n}(t)\rangle \tag{2.10}$$

where n is an arbitrary integer. The corresponding quasienergy is

$$\varepsilon_{\alpha'} = \varepsilon_\alpha + n\hbar\omega \equiv \varepsilon_{\alpha,n}. \tag{2.11}$$

Here, the Floquet state indicated by α represents the same state physically as all solutions specified by $\alpha' = (\alpha, n)$. This is a redundancy encoded in the Floquet formulation. Thus, distinct Floquet state solutions are indexed with quasienergy that falls within the Floquet-Brillouin zone, analogous to the Brillouin zone in solid-state physics,

$$-\frac{\hbar\omega}{2} \le \varepsilon_\alpha < \frac{\hbar\omega}{2} \tag{2.12}$$

Furthermore, there are several formulated theories for describing the perturbation to the periodically driven systems. The transition between Floquet states induced by a weak perturbation is formulated as Floquet Fermi's golden rule, and the linear response theory of the Floquet state is formulated as Floquet Kubo formula [128–131].

2.2 Theoretical formulation of dynamical symmetry and selection rule of high harmonic generation

2.2.1 Theoretical formalism

Symmetry is the most general concept in physics and also a general tool to describe the optical selection rules in materials. Optical selection rules in solids based on the perturbation theory are fully understood with the crystallographic point group. Here, we introduce the formulation of dynamical symmetry (DS), a concept that can also be used in the non-perturbation regime [98].

In conventional perturbative nonlinear optics, the HHG selection rules are derived by requiring the nonlinear susceptibility tensor χ in eq. (1.2) to be invariant under the symmetry operation. For example, inversion symmetry leads to $\chi^{(2n)} = 0$ (n: integer), which

means the disappearance of the even order harmonics. However, the Taylor expansion of polarization does not hold for nonperturbative nonlinear optics.

On the other hand, DS can be applied for the selection rules in a nonperturbative regime. DS was formulated as a group theory by O. Neufeld et al. [98]. The DS operations are defined by the products of spatial and temporal operations. O. Neufeld et al. derived the DS operations for (2+1)D and (3+1)D (product space of space and time) systems. Here, we focus on the DS group in (2+1)D system. In the following, we list all generators of the DS group for (2+1)D.

$$\hat{D} = \hat{T}\cdot\hat{\sigma} \tag{2.13}$$
$$\hat{Z} = \hat{\tau}_2\cdot\hat{\sigma} \tag{2.14}$$
$$\hat{H} = \hat{T}\cdot\hat{\tau}_2\cdot\hat{\sigma} \tag{2.15}$$
$$\hat{C}_2 = \hat{\tau}_2\cdot\hat{R}_2 \tag{2.16}$$
$$\hat{Q} = \hat{T}\cdot\hat{R}_2 \tag{2.17}$$
$$\hat{G} = \hat{T}\cdot\hat{\tau}_2\cdot\hat{R}_2 \tag{2.18}$$
$$\hat{C}_n = \hat{\tau}_n\cdot\hat{R}_n \tag{2.19}$$
$$\hat{C}_{n,m} = \hat{\tau}_n\cdot(\hat{R}_n)^m \equiv \hat{\tau}_n\cdot\hat{R}_{n,m} \tag{2.20}$$
$$\hat{e}_{n,m} = \hat{\tau}_n\cdot\hat{L}_b\cdot\hat{R}_{n,m}\cdot\hat{L}_{1/b} \tag{2.21}$$

where

$$\hat{L}_b = \begin{pmatrix} 1 & 0 \\ 0 & b \end{pmatrix} \tag{2.22}$$

Here, purely spatial transformations are excluded for simplicity though they give HHG selection rules. In the above operations, spatial symmetry elements include two operations: $\hat{R}_n$ ($\hat{R}_n$ stands for rotation by an angle $2\pi/n$, and reflections, denoted by the operator $\hat{\sigma}$. Temporal symmetry elements include time-reversal, denoted by $\hat{T}$, and time-translations, where translations by time T/n are denoted by $\hat{\tau}_n$. $\hat{C}_{n,m}$ is the generalized version of $\hat{C}_n$. For $m=1$, $\hat{C}_{n,m}$ reduces to $\hat{C}_n$. $\hat{e}_{n,m}$ denotes discrete elliptical symmetry scaled by the transformation $\hat{L}_b$ that generalizes $\hat{C}_{n,m}$. This symmetry has no analog in molecular groups [98]. Figures 2.1-2.3 shows the examples of driving electric fields that is invariant under each dynamical symmetry operation. DS is an excellent concept to discuss the symmetry and HHG selection rule for complex electric field waveforms as shown in these figures.

When the Hamiltonian $\hat{H}$ conforms to a DS group G, the Floquet Hamiltonian commutes with all symmetry operation $\hat{X}_q$ in G:

$$[\hat{X}_q, H_F] = 0, \quad \hat{X}_q \in G, \tag{2.23}$$

where $\hat{X}_q$ is the corresponding unitary or anti-unitary operator to the above DS operators ($\hat{X}$) defined in (2+1)D system. In this case, the Floquet states are simultaneous eigenmodes of the Floquet Hamiltonian, and of $\hat{X}$. Since $\hat{X}_q$ is unitary or anti-unitary, its eigenvalues are

$$\hat{X}_q\,|\Phi_\alpha(t)\rangle = e^{I\theta}\,|\Phi_\alpha(t)\rangle\,, \tag{2.24}$$

When the wave function is described by a single Floquet state, the observables satisfy the following relation

$$\mathbf{o}(t) = \langle\Phi_\alpha(t)|\hat{X}_q\hat{O}\hat{X}_q^\dagger|\Phi_\alpha(t)\rangle = \hat{X}\cdot\mathbf{o}(t), \tag{2.25}$$

Since the electric field $\mathbf{E}_{HHG}(t)$ of the high harmonics are radiated from the current $\mathbf{J}(t)$ in the Floquet system,

$$\mathbf{J}(t) = \hat{X} \cdot \mathbf{J}(t) \tag{2.26}$$

gives the selection rules of HHG. If we consider a simple case where current flows uniformly in xy plane at z=0, the electric field induced by the current is given by

$$\mathbf{E}(z,t) = \frac{1}{2}\mu_0 c \mathbf{J}\left(t - \frac{z}{c}\right) \tag{2.27}$$

where μ_0 is magnetic permeability in a vacuum and c is the speed of light [38, 58]. Thus, we can require

$$\mathbf{E}(t) = \hat{X} \cdot \mathbf{E}(t) \tag{2.28}$$

to derive the selection rule of HHG.

Table 2.1 shows the HHG selection rules [98]. When we derive the dynamical symmetry of laser-driven atomic gases, it is enough to consider the symmetry of the driving electric field since the atomic gases are isotropic. However, in the case of solids, we also have to consider the discrete spatial symmetry of solids to derive the DS.

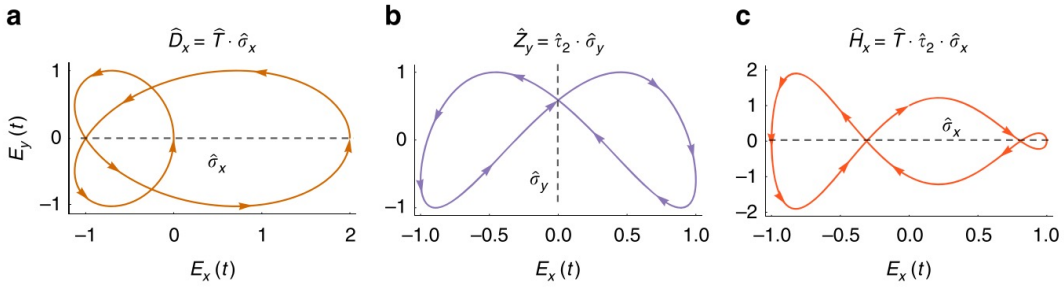

Figure 2.1: Order-2 spatiotemporal DSs in (2+1)D involving spatial reflection with examples for each symmetry. (a) $\hat{D}_x$ symmetry for the example field $\mathbf{E}(t) = (\cos(\omega t) + \cos(2\omega t))\hat{x} + \sin(2\omega t)\hat{y}$, (b) $\hat{Z}_y$ symmetry for the example field $\mathbf{E}(t) = \sin(\omega t)\hat{x} + \sin(2\omega t + \pi/5)\hat{y}$, and (c) $\hat{H}_x$ symmetry for the example field $\mathbf{E}(t) = \sin(\omega t)\hat{x} + \cos(3\omega t)\hat{y}$. The fields are represented on Lissajou plots. The spatial parts of the operators is indicated by dashed lines, colored arrows in the plots indicate the direction of time. Reproduced from O. Neufeld, D. Podolsky, and O. Cohen, Nature Communications **10**, 405 (2019). ©2019 The authors. Distributed under a Creative Commons Attribution 4.0 International license (CC BY 4.0) [98].

2.2.2 Example for selection rule of HHG

The even-order harmonics are forbidden in the system with inversion symmetry, such as atomic gases. This can be explained in terms of DS. The system with inversion symmetry driven by linearly polarized laser field has the symmetry denoted by $\hat{Z} = \hat{\tau}_2 \cdot \hat{\sigma}$ with a reflection symmetry with respect to the plane perpendicular to the direction of laser polarization. Figure 2.4 shows the consequent operation of $\hat{\tau}_2$ and $\hat{\sigma}$ for this system. $\hat{\tau}_2$ shifts

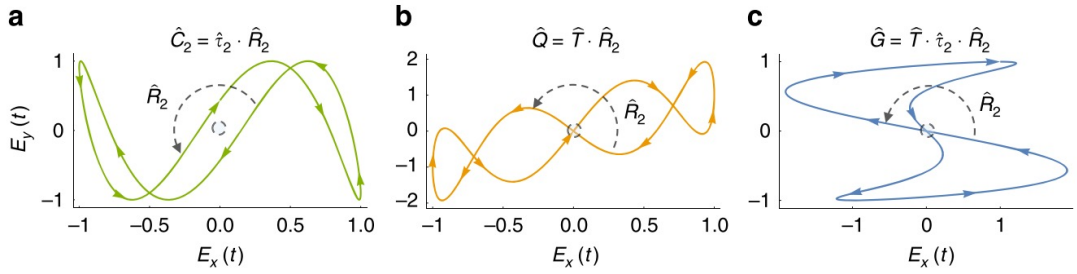

Figure 2.2: Order-2 spatiotemporal DSs in (2 + 1)D involving spatial rotations by 180° with examples for each symmetry. (a) $\hat{C}_2$ symmetry for the example field $\mathbf{E}(t) = \sin(\omega t)^x + \sin(3\omega t + \pi/7)\hat{y}$, (b) $\hat{Q}$ symmetry for the example field $\mathbf{E}(t) = \sin(\omega t)\hat{x} + (\sin(\omega t) + \sin(4\omega t))\hat{y}$, and (c) $\hat{G}$ symmetry for the example field $\mathbf{E}(t) = (\sin(2\omega t) + \cos(3\omega t))\hat{x} + \cos(\omega t)\hat{y}$. The fields are represented on Lissajou plots. The spatial parts of the operators is indicated by dashed arrows, colored arrows in the plots indicate the direction of time. Reproduced from O. Neufeld, D. Podolsky, and O. Cohen, Nature Communications **10**, 405 (2019). ©2019 The authors. Distributed under a Creative Commons Attribution 4.0 International license (CC BY 4.0) [98]

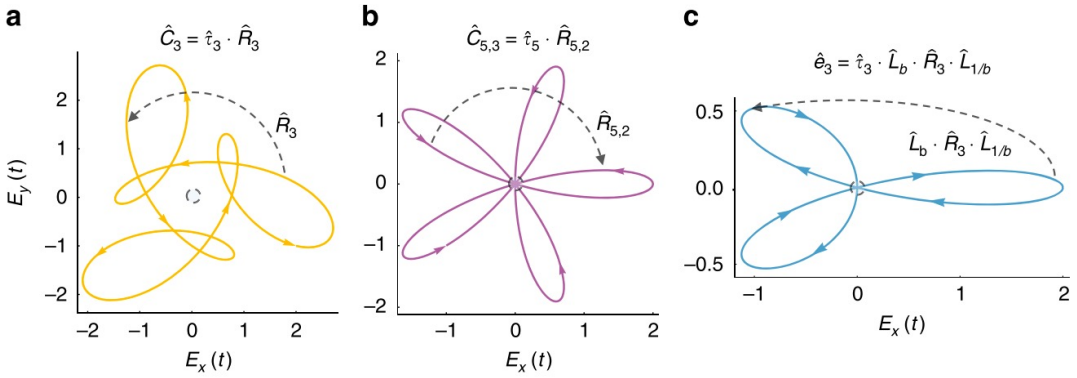

Figure 2.3: High-order spatiotemporal DSs in (2+1)D with examples of each symmetry. (a) $\hat{C}_3$ symmetry for the example field $\mathbf{E}(t) = (\cos(\omega t) + \cos(2\omega t) + \sin(4\omega t))^x + (\sin(\omega t) - \sin(2\omega t) - \cos(4\omega t))\hat{y}$, (b) $\hat{C}_{5,3}$ symmetry for the example field $\mathbf{E}(t) = (\cos(3\omega t) + \cos(2\omega t))\hat{x} + (\sin(3\omega t) - \sin(2\omega t))^y$, and (c) $\hat{e}_3$ symmetry for the example field $\mathbf{E}(t) = (\cos(\omega t) + \cos(2\omega t))\hat{x} + b(\sin(\omega t) - \sin(2\omega t))\hat{y}$. The fields are represented on Lissajou plots. The spatial parts of the operators is indicated by dashed arrows, colored arrows in the plots indicate the direction of time Reproduced from O. Neufeld, D. Podolsky, and O. Cohen, Nature Communications **10**, 405 (2019). ©2019 The authors. Distributed under a Creative Commons Attribution 4.0 International license (CC BY 4.0) [98].

Table 2.1: (2+1)D DSs and their associated selection rules for collinear atomic/molecular HHG [98]

Symmetry	Order	Harmonic generation selection rule
$\hat{D},\hat{H}$	2	Elliptically polarized harmonics with major/minor axis corresponding to the reflection axis.
$\hat{T},\hat{Q},\hat{G}$	2	Linearly polarized only harmonics.
$\hat{Z}$	2	Linearly polarized only harmonics, even harmonics are polarized along the reflection axis, and odd harmonics are polarized orthogonal to the reflection axis.
$\hat{C}_2$	2	Odd-only harmonics, any polarization is possible.
$\hat{C}_{n,m}$	$n>2$	$(\pm)$ circularly polarized $(nq\mp m)$ harmonics, $q\in N$, all other orders forbidden.
$\hat{e}_{n,m}$	$n>2$	$(\pm)$ elliptically polarized $(nq\mp m)$ harmonics, $q\in N$, with an ellipticity b, all other orders forbidden.

the temporal profile from the solid line to the dashed line and $\hat{\sigma}$ reverses the direction of the electric field. According to Table 2.1, this symmetry operation gives the linearly polarized harmonics, where even harmonics are polarized along the reflection axis, and odd harmonics are polarized orthogonal to the reflection axis. In addition, this system has a reflection symmetry with respect to the plane that contains the direction of oscillation of the laser electric field. The perpendicular component of high harmonics is forbidden due to this reflection symmetry. Therefore, in systems with inversion symmetry, the only odd-order harmonics with polarization parallel to the driving field are observed.

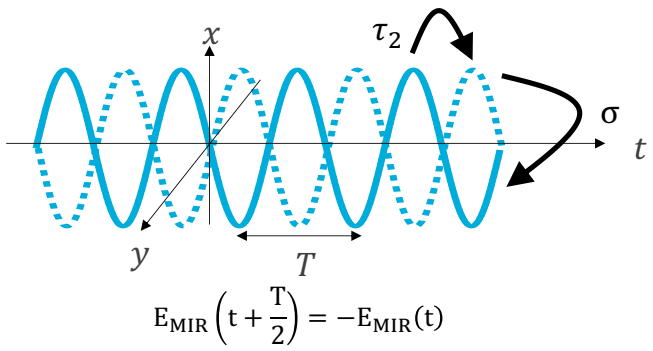

Figure 2.4: Dynamical symmetry operation $\hat{Z}$ for a monochromatic laser electric field along x-direction. T is the period of the laser electric field. $\hat{\tau}_2$ shifts the blue solid line to blue dashed line. $\hat{\sigma}$ reverses the direction of the electric field.

The selection rules associated with the operation $\hat{Z}$ can be explained by the difference of the symmetry of the electric field with the odd and even order harmonic frequency. As shown in Fig. 2.5, the odd order field (e.g. ω, 3ω) has the symmetry of $E_{\text{odd}}(t+T/2) = -E_{\text{odd}}(t)$, where T is the period of the driving field. On the other hand, the even order field (e.g. ω, 3ω) has the symmetry of $E_{\text{even}}(t+T/2) = E_{\text{even}}(t)$. Thus, when the system has the symmetry of $\hat{Z}$, only odd-order harmonics are allowed in the parallel polarization with the driving field.

The operators $\hat{C}_n$ give the circular polarization selection rules. In particular, $\hat{C}_3$ de-

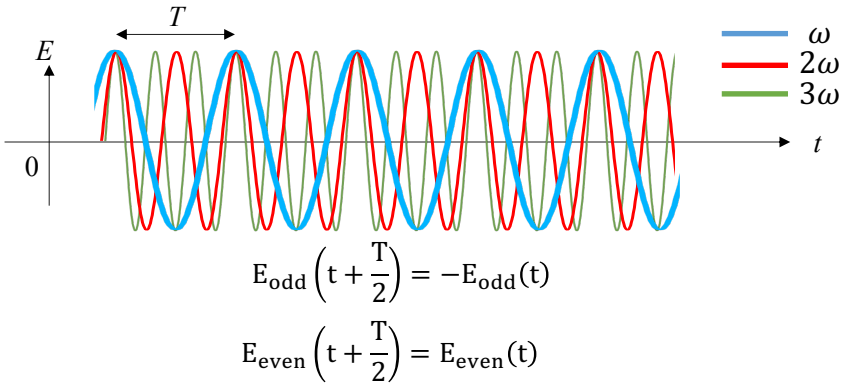

Figure 2.5: Difference of DS between odd and even order harmonics. $T = 2\pi/\omega$ denotes the period of the driving laser frequency. The blue, red, and green curves represent the monochromatic electric field with the frequency of ω, 2ω, and 3ω, respectively.

scribes the circular polarization selection rule of HHG experimentally obtained in a crystalline solid with three-fold rotational symmetry and in atomic gases under a bi-circular laser field [95, 105]. This operation leads to the selection rule in which only $(\pm)$ circularly polarized $(3q \mp 1)$ harmonics $(q \in N)$ is allowed. These selection rules lead to the angular momentum conservation rule of light. The left- and right-circular polarization corresponds to the spin degree of freedom of light. Figure 2.6 shows the energy diagram of the angular momentum conservation rule of HHG. n photons with frequency ω are converted to one photon with frequency $n\omega$. In the case of isotropic media (atomic gases), the system is invariant under infinitesimal rotation symmetry operation. Thus, the total spin of the incident photon and emitted photon should be conserved. As a result, high harmonics are forbidden under circularly polarized driving fields in atomic gases since a photon cannot have the angular momentum of $n\hbar$ $(n > 2)$. This corresponds to the case for $\hat{C}_\infty$. However, in solids, the continuous rotational symmetry is broken and only the discrete rotational symmetry remains. Thus, the Umclapp process for angular momentum occurs. In this case, the angular momentum of $n\hbar$ can be regarded as equal to 0. Therefore, HHG with a single circular polarization driving field is partly allowed in solids. Similar to the nonperturbative HHG in solids, perturbative second harmonic generation has been observed under circularly polarized light in a metal structure and monolayer MoS_2, which have three-fold rotational symmetry [105, 132, 133]. Their selection rule follows a selection rule based on angular momentum conservation. It is worth noting that the photon picture does not hold in nonperturbative light-matter interactions. From this point of view, DS is a powerful concept that can extend our understanding of the selection rule to the non-perturbative regime.

2.3 Light-matter interaction in two level system

The above selection rules can be derived if the system can be written with a single Floquet state. However, in an actual system, the laser fields used for HHG have no perfect periodicity because the ultrashort pulse durations contain only several cycles. Since the

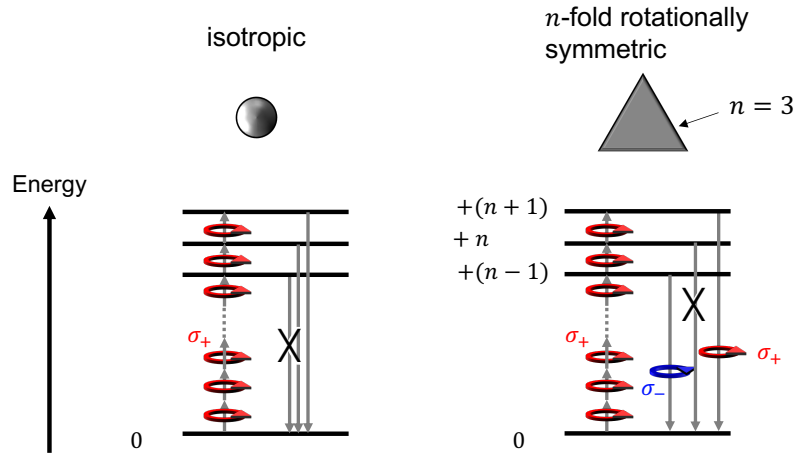

Figure 2.6: Energy diagram for spin angular momentum conservation rule of light in (a) isotropic media (atomic gases) and (b) the media with n-fold rotational symmetry (crystalline solids). The top left and right figures represent typical structures of isotropic and three-fold rotationally symmetric media. Black horizontal bars represent virtual states. The vertical arrows means the transition between the states. The "$\times$" represents the forbidden transition. σ^+ and σ^- represent the helicity of photons.

system is not in equilibrium during ultrashort laser pulses, the electronic state can change in time with each laser cycle. For example, the accumulation of excited carriers during the strong laser field irradiation may break the time-translational symmetry of the electronic dynamics in semiconductors.

Here, we show the example of the dynamics of carrier excitation under light field by using a simple two-level system. In second quantization, the Hamiltonian of a two level system interacting with light within the dipole approximation is given by

$$H = E_1 a_1^\dagger a_1 + E_2 a_2^\dagger a_2 - dE(t)(a_1^\dagger a_2 + a_2^\dagger a_1) \tag{2.29}$$

where the dipole moment is defined as

$$d = \int_{-\infty}^{\infty} \psi_2^*(x)(-ex)\psi_1(x)dx. \tag{2.30}$$

E_1, E_2 are eigenenergies of the level 1 and 2 and ψ_1, ψ_1 are corresponding eigenfunctions. The creation $a^\dagger$ and annihilation a operators create and annihilate electrons in states number 1 or 2, respectively. Here, we neglect the degree of freedom for the polarization of the electric field $E(t)$. The expectation values $\langle a_1^\dagger a_1 \rangle = N_1$ and $\langle a_2^\dagger a_2 \rangle = N_2$ are the occupation numbers of level 1 and level 2 and satisfy $f_1 + f_2 = 1$. $\langle a_1^\dagger a_2 \rangle = P$ is the coherence between the level 1 and 2, which is relevant to the optical polarization.

The time evolution of the occupation and the coherence is calculated by Heisenberg equation:

$$i\hbar \frac{\partial}{\partial t}\mathscr{O} = [\mathscr{O}, H] \tag{2.31}$$

and the anticommutation rules for fermions, i.e.,

$$[a_1, a_1^\dagger] = 1, \quad [a_2, a_2^\dagger] = 1 \tag{2.32}$$

and all other anticommutators are zero. The derived equation is so-called optical Bloch equation [134]

$$\frac{d}{dt}P = -i\omega_0 P - \frac{i}{\hbar}dE(t)(N_1 - N_2) \tag{2.33}$$

$$\frac{d}{dt}N_1 = \frac{i}{\hbar}2\mathrm{Im}[dE(t)P] \tag{2.34}$$

$$\frac{d}{dt}N_2 = -\frac{i}{\hbar}2\mathrm{Im}[dE(t)P] \tag{2.35}$$

where $\omega_0 = (E_1 - E_2)/\hbar$. This set of equations is an analogue of the Bloch equations that describe the time evolution of spins in a magnetic field. Here, we define the Bloch vector

$$\begin{pmatrix} u \\ v \\ w \end{pmatrix} = \begin{pmatrix} \langle a_1^\dagger a_2\rangle + \langle a_2^\dagger a_1\rangle \\ -i(\langle a_1^\dagger a_2\rangle - \langle a_2^\dagger a_1\rangle) \\ \langle a_1^\dagger a_1\rangle - \langle a_2^\dagger a_2\rangle \end{pmatrix} = \begin{pmatrix} 2\mathrm{Re}[P] \\ 2\mathrm{Im}[P] \\ N_1 - N_2 \end{pmatrix} \tag{2.36}$$

The length of the Bloch vector satisfies $u^2 + v^2 + w^2 = 1$ within the time evolution according to the optical Bloch equations (2.33)-(2.35). The Rabi frequency $\Omega(t) = dE(t)/\hbar$ determines the magnitude of the light-matter interaction in this system.

The solution for the resonant excitation shows a well-known phenomenon, Rabi oscillation. Figure 2.7 shows the solution calculated with boxed shape electric field with the peak Rabi frequency of $\Omega = 0.04$. Figure 2.7(a) shows the electric field and Fig. 2.7(b) shows the occupation number in level 1. We calculated it with no initial population in the excited state (level 1). The angular frequency of electric field ω is set to be equal to ω_0. In this case, electrons absorb the photons and in turn, are excited from the ground state into the excited state (level 1). This corresponds to the well-known optical transition described by Fermi's golden rule. In this calculation, the electron behaves full quantum mechanically, thus the N_1 exceeds 0.5 and makes population inversion. Then, due to the stimulated emission, electrons relax back to their ground state. These phenomena repeat with the frequency of Rabi frequency (Ω). The slow oscillating component in Fig. 2.7(b) is so-called Rabi oscillation (only 5/4 cycle of the oscillation is shown in Fig. 2.7(b)). In addition, small and rapid oscillation can be seen in Fig. 2.7(b). This is called Bloch-Siegert oscillation, which is often neglected in the resonant case by applying the rotating wave approximation [3].

On the other hand, if the electrons are excited by a non-resonant electric field, the electrons do not show Rabi oscillation. Since this corresponds to the light irradiation to a transparent media, one may imagine that the electrons cannot absorb the photons. However, during the application of the strong light, electrons can be excited into an upper level. This is called virtual excitation, which is closely related to the tunneling process.

Let us consider the two-level system for electrons in a solid is excited by a non-resonant strong mid-infrared light pulse. Figure 2.8(a) shows the electric field $E(t) = \cos(\omega t)\exp(-t^2/\tau^2)$ used for the calculation, which has the pulse duration of 60 fs (full width at half maxima). The resultant solution of eqs. (2.33)-(2.35) is shown in Fig. 2.7(b). We set calculation parameters to be similar to the experiments shown later. The center frequency of the electric field is set to 0.3 eV, which is non-resonant with the energy gap of 1 eV of the two-level system. The maximum of the Rabi frequency is set to 0.3 eV. In this case, the orbit of the Bloch vector has the shape of an ellipse extending along the X-axis (u), which is different from the resonant case (Fig. 2.7). In this case, N_1 only

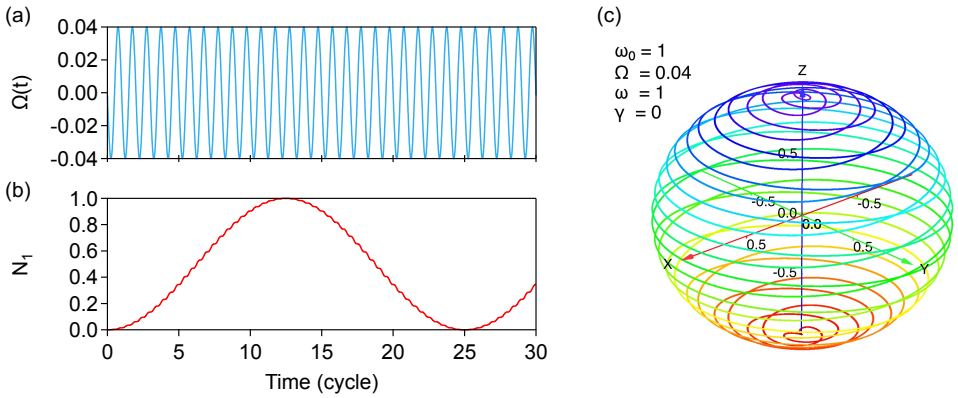

Figure 2.7: Ilustration of Rabi oscillation calculated by using eqs. (2.33)-(2.35). (a) Time profile of the Rabi frequency (electric field) used for the calculation. (b) Time evolution of N_1. The bottom axis corresponds to the number of the cycle of the electric field. (c) Orbital of Bloch vector in Bloch sphere. The axes X,Y and Z correspond to u, v, and w in eq. (2.36), respectively. The color of the orbital represents the value of $w = N_1 - N_2$. The calculation parameters are $\omega_0 = 1$, $\Omega_0 = 0.04$, $\omega = 1$ for gap frequency, peak Rabi frequency, and driving frequency, respectively.

appears near the peak of the applied electric field and suddenly vanishes in each cycle. This behavior corresponds to the fact that the Bloch-Siegert term becomes significant in a non-resonant electric field [3, 135]. The upper-level occupation does not remain after the pulse has passed. This is consistent with the energy conservation rule between the photons and electrons. The electrons cannot be excited into the upper energy state by absorbing the photons. In the limit of high Rabi frequency ($\Omega \gg \omega$), the electrons are highly excited by the carrier wave of the light field. This is called carrier-wave Rabi oscillation [3].

Next, we consider the effect of dephasing in the two-level system under the condition of non-resonant electric field. When the two-level system is not isolated but interacting with an external bath, the phase of the coherence is randomized due to the interaction. Such effect is phenomenologically included as a dephasing rate γ in the optical Bloch equations

$$\frac{d}{dt}P = -i\omega_0 P - \frac{\gamma}{\hbar}P + \frac{i}{\hbar}dE(t)(N_1 - N_2) \tag{2.37}$$

$$\frac{d}{dt}N_1 = \frac{i}{\hbar}2\mathrm{Im}[dE(t)P] \tag{2.38}$$

$$\frac{d}{dt}N_2 = -\frac{i}{\hbar}2\mathrm{Im}[dE(t)P] \tag{2.39}$$

where the transverse relaxation is set to 0 by assuming the relaxation is slow enough compared with the pulse duration. The dephasing reduces the magnitude of the coherence P. When there is a dephasing process in the two-level system, the electrons can absorb even the non-resonant photons.

Figure 2.8(d) shows the dephasing dependence of the length of the Bloch vector. The length of the Bloch vector is conserved if there is no dephasing (depicted with a red line in Fig. 2.8(d)). If there is a finite dephasing, the length of the Bloch vector is no longer

conserved and shortened in the electric field. Figure 2.8(e) shows the time evolution of the Bloch vector in the Bloch sphere. The shortening of the Bloch vector displaces it towards the w direction under the driving field. Accordingly, N_1 increases up to 0.5 in an electric field as shown in Fig. 2.8(f). The efficiency of the tunneling process that is dependent on the dephasing rate has already been studied in GaAs under strong THz field [136]. Around $N_1 = 0.5$ with large damping, electrons cannot be excited by the electric field since the source term (the third term of eq. (2.37)) becomes 0 at $N_1 = 0.5$, i.e., $(N_1 - N_2) = 0$. This is called phase-space filling effect, which is attributed to the Fermi-Dirac statistics of electrons.

The above example calculated in a two-level system also explains the time evolution of interband transition of Bloch electrons in a strong non-resonant driving field. In the case of Bloch electrons in solids, interband transitions are accompanied by their transitions in k-space. Due to the existence of the dephasing process, the fully quantum mechanical (coherent) time evolution of electrons is disturbed. Thus, incoherent electrons are accumulated in the upper energy state during a strong electric field driving. This carrier accumulation may break the time translational symmetry during the MIR field driving through many-body processes, such as phase-space filling and excitation-induced dephasing discussed in Chapter 4.

2.4 Summary

In this Chapter, we explained the theoretical formalisms of the Floquet theorem and DS. The application for the DS operation of the periodically driven system to radiated harmonic gives the polarization selection rules of HHG. Although a perfect time periodicity is assumed for the DS, the actual time evolution of the electronic state is not perfectly periodic. We showed examples of electron dynamics by using optical Bloch equations in a two-level system. Accumulation of the incoherent carriers and many-body effects may break the DS of the system driven by strong infrared ultrafast laser pulses. Chapter 4 shows how these accumulated incoherent electron-hole pairs affect the HHG in atomically thin semiconductors.

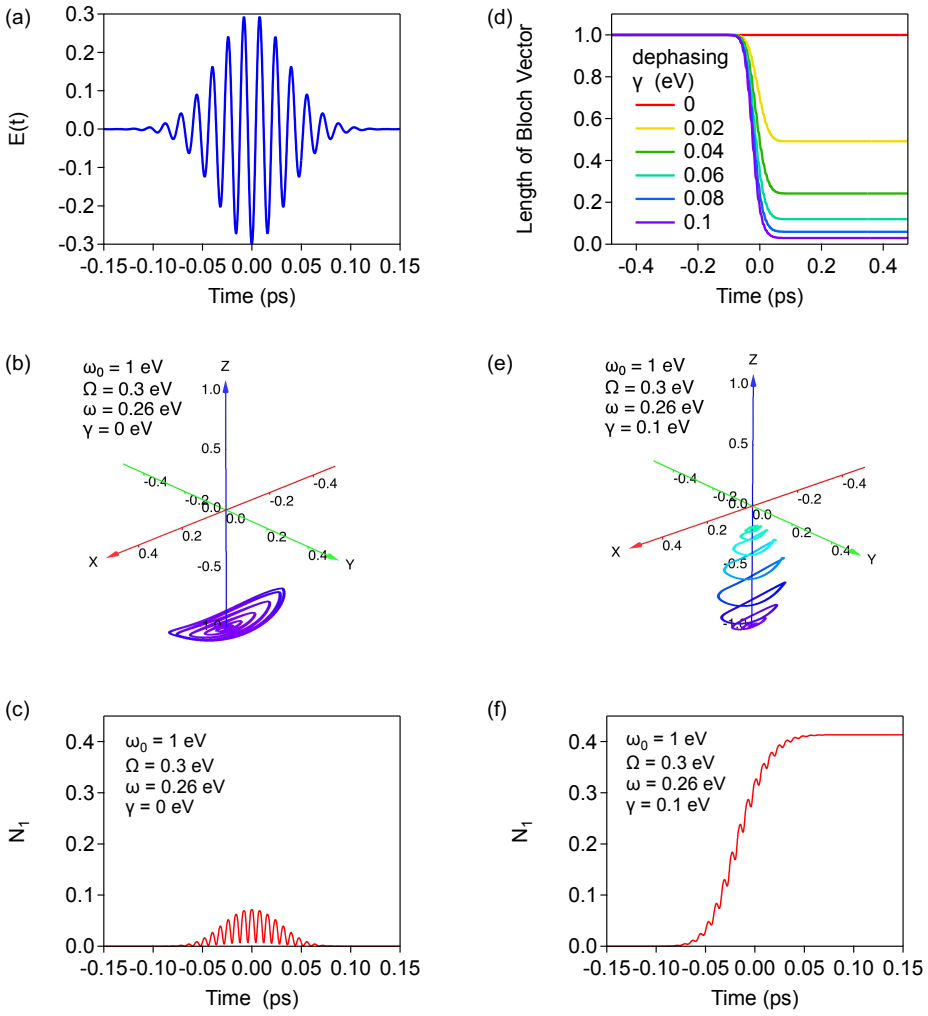

Figure 2.8: Example of solution for eqs. (2.33)-(2.35). (a) Time profile of the electric field used for the calculation. (b) Orbital of Bloch vector in Bloch sphere without dephasing. The axes X,Y and Z correspond to u, v, and w in eq. (2.36), respectively. The color of the orbital represents the value of $w = N_1 - N_2$. (c) Time evolution of N_1 corresponding to (b). (d) Dependence of the length of the Bloch vector on dephasing rate. (e) Orbital of Bloch vector in Bloch sphere at dephasing rate of 0.1 eV. (f) Time evolution of N_1 corresponding to (e). The calculation parameters are $\omega_0 = 1$ eV, $\Omega_0 = 0.3$ eV, $\omega = 0.26$ eV, for gap frequency, peak Rabi frequency, and driving frequency, respectively.

Chapter 3

Polarization selection rules of high order sideband generation

3.1 Introduction

Floquet engineering is a potential concept for coherent control of electronic states under a strong light field [101, 102, 129, 137–140]. The Floquet theoretical approach is useful for describing strong light-matter interactions at energy scales beyond which perturbation theory works [16]. In this nonperturbative regime, intense light is predicted to change the symmetry and topology of the states and in turn the electronic properties of solids [129, 137]. The Floquet state in solids has been verified through time and, angle-resolved photoemission spectroscopy [101,138], time-resolved absorption spectroscopy [139,140], and time-resolved transport measurements [102]. Its properties, such as nonperturbative electron dynamics during the period of the driving laser, can also be explored by using high-order harmonic generation (HHG) [36, 37, 52, 56], which is a coherent emission process from a Floquet system [28, 75, 92, 98, 105]. Here, we examine light scattering in a Floquet system by injecting an additional probe pulse. Compared with HHG, tuning of the polarization and frequency of the probe light may provide more detailed information about the symmetries and electronic structures. This process is nothing but high-order sideband generation (HSG) [13, 85, 86, 88].

In the following, we systematically present polarization selection rules, which is fundamental to probe the symmetry of the electronic states, for HSG in monolayer MoS_2 under a mid-infrared (MIR) driving field. In a Floquet system, the electronic properties are described by a unique class of symmetries, called dynamical symmetries (DSs), which unify the symmetries of the spatio-temporal profiles of the laser field and material [28, 92, 96, 98, 101, 105, 138]. It has been experimentally confirmed that DSs govern the band crossings of surface electrons in a light-driven topological insulator [94, 101] and determines the polarization selection rules for HHG in a circularly polarized light-driven crystalline solid [105]. Here, we introduce a new interpretation, i.e., HSG as “Raman scattering” of the MIR-driven Floquet state, and use the DS concept to achieve a full understanding of the polarization selection rules.

3.2 Sample

We have two ways to obtain monolayer TMDs: exfoliation or chemical vapor deposition. In this experiment, we prepared monolayer MoS_2 and $MoSe_2$ grown with the chemical vapor deposition (CVD) method on sapphire substrates. These atomically thin semiconductors allow us to avoid propagation effects in the HSG experiment. The monolayer flake size of MoS_2 was typically one hundred micrometers and $MoSe_2$ was typically tens of micrometers. HHG and HSG experiments are performed with strong laser power just below the damage threshold. Thus, in the experimental procedure, we have to check the damage threshold of the sample first, and then complete all experiments with carefully checking the damage. Therefore, in the experimental procedure, we need a large area of the sample or a number of samples. For this reason, CVD samples are better than exfoliated samples. Figure 3.1 shows the typical photograph of the sample of monolayer MoS_2. This sample was provided by Prof. Yasumitsu Miyata and Mr. Takahiko Endo at Tokyo Metropolitan University. The MoS_2 monolayers were prepared by using the method reported by Kojima, K. et al. [141]. The sample size is larger than the spot size of the MIR light at the focal plane. The side of the triangle grain is along the zigzag direction of the monolayer TMDs. The monolayer $MoSe_2$ was purchased from 2D Semiconductors, Inc.

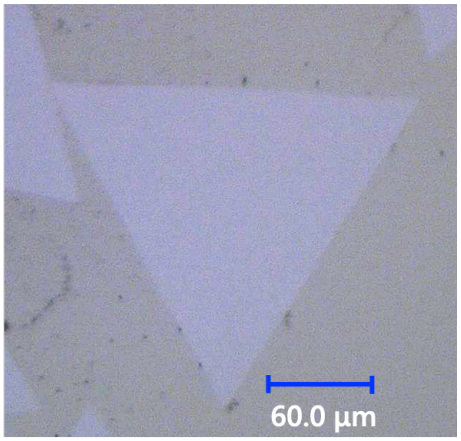

Figure 3.1: Photograph of monolayer MoS_2 used for the experiment provided by Prof. Yasumitsu Miyata and Mr. Takahiko Endo in Tokyo Metropolitan University. The monolayer MoS_2 is fabricated with chemical vapor deposition method on a sapphire substrate.

3.3 Experimental setup

Figure 3.2 shows a schematic diagram of the HSG measurement. We used intense MIR pulses (photon energy: $\hbar\omega_{MIR} = 0.26$ eV, pulse duration: 60 fs) to create a Floquet state in monolayer MoS_2. To achieve a nonperturbative regime without damaging the monolayer, we set the photon energy of the pulses to a much lower energy than the exciton energy of the monolayer (1.8 eV) [52]. In addition, we injected weak near-infrared (NIR) pulses nearly resonant with the bandgap energy (photon energy: $\hbar\omega_{NIR} = 1.55$ eV, pulse duration: 110 fs) into the MIR-driven system. We controlled the polarizations of the MIR and

NIR pulses by using liquid crystal retarders and resolved the polarization of the sidebands by using wave plates and polarizers. The sideband spectra were detected by a spectrometer equipped with a CCD camera. Throughout this paper, we denote the zigzag direction of monolayer MoS_2 as X and armchair direction as Y.

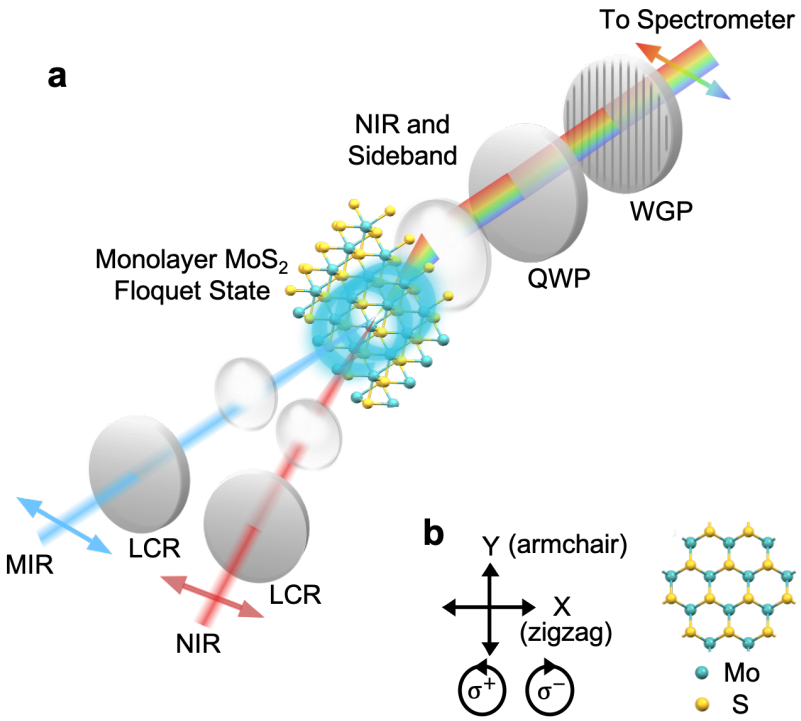

Figure 3.2: Schematic of high-order sideband generation (HSG) measurement. **a** Experimental setup (LCR liquid crystal retarder, QWP quarter wave plate, WGP wire grid polarizer). **b** The definition of the polarization. The X and Y directions correspond to the zigzag and armchair directions of monolayer MoS_2. Reproduced from K. Nagai *et al.*, Communications Physics **3**, 137 (2020). ©2020 The authors. Distributed under a Creative Commons Attribution 4.0 International license (CC BY 4.0) [1].

The detail of the experimental setup for the HSG measurements is shown in Fig. 3.3. Ultrafast laser pulses (photon energy 1.55 eV, 35 fs pulse duration, 1 kHz repetition rate, 7 mJ pulse energy) were derived from a Ti:sapphire based regenerative amplifier. Some of the total pulse energy (1 mJ) was used to generate signal and idler beams by an optical parametric amplifier (OPA, TOPAS-C, Light Conversion). The MIR pulses (photon energy 0.26 eV) were obtained by difference frequency generation (DFG) of the signal and idler beams in an $AgGaS_2$ crystal. After the DFG, the signal and idler beams were blocked by a long-pass filter (LPF) with a cutoff wavelength of 4 μm. The total MIR pulse energy measured just behind the LPF was 3-3.5μJ. Another part of the ultrafast laser pulses was passed through a bandpass filter (BPF) centered at 800 nm (bandwidth 10 nm) and used as the NIR probe pulses. The polarizations of the NIR and MIR pulses were controlled by a wire grid polarizer (WGP), a Glan laser polarizer (GLP), and liquid crystal variable retarders (LCR). The MIR pulses were focused by a ZnSe lens to a spot 60 μm in diameter (full width at half maximum). The spot size of the MIR pulse was

measured by the knife-edge method by assuming the gaussian profile. This spot size is smaller than the sample size of CVD grown monolayer MoS_2 shown in Fig. 3.1. Thus, our measurements were conducted for a single monolayer MoS_2. On the other hand, in the case of $MoSe_2$, multiple grains were contained in the spot size. The spot size of the NIR pulse was determined from the image on the camera in Fig. 3.4 that was built into the setup drawn in Fig. 3.3. The NIR pulses were passed through a fused-silica lens and reflected by a D-shaped mirror placed below the MIR beam. The NIR pulses were focused onto the sample almost coaxially with the MIR beams (approximately 4 degrees between the two beams). The pulse durations of NIR and MIR pulses were estimated to be 110 fs and 60 fs (full width at half maximum), respectively. The generated harmonics and sidebands were collected by a fused-silica lens and their spectra were analyzed by a grating spectrometer (iHR320, Horiba) equipped with a Peltier-cooled Si charge-coupled device camera (Syncerity CCD, Horiba). The NIR light was blocked by 750 nm and 550 nm short-pass filter (SPF) in front of the spectrometer. The polarization of the sidebands was resolved by a quarter-wave plate (Berek variable waveplate) and a wire grid polarizer. The retardance in the Berek variable waveplate is determined so that the linearly polarized second-order sideband becomes circularly polarized after passing through the waveplate. The relative angle between the crystal axis of the MoS_2 and laser polarization was roughly determined from the sample image obtained by the setup drawn in Fig. 3.3 and confirmed by the polarization selection rule of HHG [44, 52]. On the other hand, the angle of the $MoSe_2$ crystal was not determined. Thus, we only measured HSG for circularly polarized light in monolayer $MoSe_2$. The obtained spectra were corrected for the total efficiency including mirrors, a spectrometer, and a CCD camera. All the experiments were performed in the air at room temperature.

Experimental procedure to observe HHG and HSG

Below, we write down the experimental procedure to optimize the setup for HSG.

(1). The position of the sample in its depth direction was determined by maximizing the harmonic intensity from the sample. A bulk GaSe sample was used for the reference sample since it has high efficiency for HHG.
(2). The position of the GaSe sample was monitored by using the microscope system in Fig. 3.4 that was built into the setup drawn in Fig. 3.3.
(3). The position in the depth direction of the objective lens mounted on a manual stage was adjusted to make the sample image on the scientific camera.
(4). The position of the MIR beam spot in the plane parallel to the sample was adjusted by monitoring the HHG and luminescence with the camera.
(5). The bulk GaSe was replaced by the monolayer sample and its position in the sample plane is adjusted by the manual stage for the sample mount.
(6). Maximize the HHG in the sample.
(7). The NIR beam is focused onto the sample so that it overlaps with the MIR beam spot.
(8). The temporal overlap was determined by moving the delay stage so that the second-order sideband was generated. (not to set the position to the satellite peak due to multi-reflection from the optical system.)
(9). The time origin was precisely determined by maximizing the first-order sideband intensity. (Although the intensity of the second-order sideband is larger than that of the

first order, it contains the third-order nonlinear optical signal from the sapphire substrate. Its time-delay dependence shows a different maximum position from that of the first-order sideband. We confirmed that the intensity of the second-order sideband from the substrate under linearly polarized excitation was one order of magnitude smaller than that from the monolayer sample when the time-delay is adjusted for the first-order sideband.)

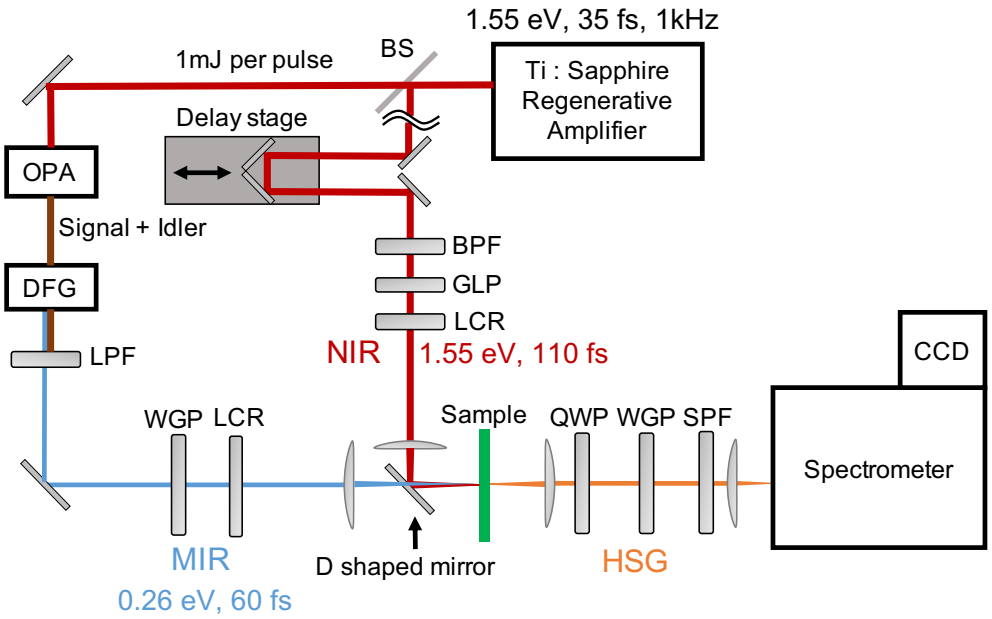

Figure 3.3: Experimental Setup. (BS: beam splitter, BPF: band pass filter, GLP: Glan laser polarizer, LCR: liquid crystal retarder, OPA: optical parametric amplifier, DFG: difference frequency generation, LPF: long pass filter, WGP : wire grid polarizer, QWP : quarter wave plate, SPF : short pass filter). Reproduced from the supplemental document of K. Nagai *et al.*, Communications Physics **3**, 137 (2020). ©2020 The authors. Distributed under a Creative Commons Attribution 4.0 International license (CC BY 4.0) [1].

Compensation of chirp of MIR pulse duration

The efficiency of the high harmonics is highly dependent on the time profile of the MIR pulse since HHG is a highly nonlinear process. The time profile is modulated when the MIR pulse passes through the filters and LCR due to the group velocity dispersion in the media. Thus, the dispersion of the MIR pulse was compensated by inserting CaF_2 plates into the optical path of the MIR pulse. The total thickness of the CaF_2 was determined to maximize the efficiency of HHG from the monolayer sample.

Correction of measured spectra

The spectra shown in this thesis are corrected from the spectra measured by a CCD camera. The corrections are summarized here.

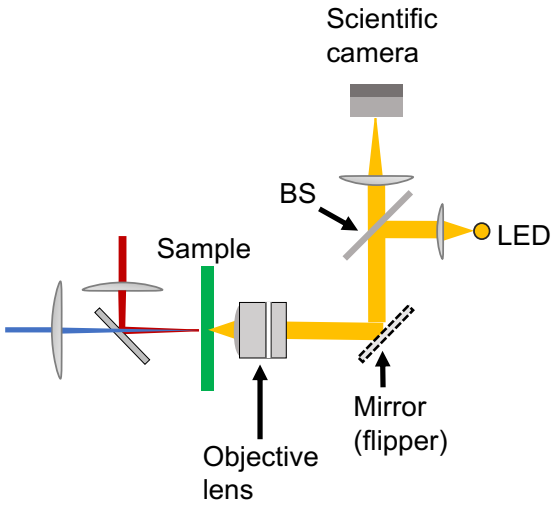

Figure 3.4: Experimental Setup for sample monitoring (BS: beam splitter). The objective lens is placed on a flipper mount and can be switched with the fused silica collection lens in Fig. 3.3.

(1). Correction of the diffraction efficiency of the grating in the spectrometer and correction of the quantum efficiency of the CCD camera.
(2). Correction of the reflection efficiency of the two aluminum mirrors on the detection side (S and P polarization, respectively).

The data for the correction (1) is obtained by directly measuring the spectra of a Halogen lamp for calibration. The reflection efficiency of the mirrors are obtained from the specification sheet of the aluminum mirrors.

Estimation of pulse intensity at the sample surface

The method of estimating the peak intensity of the incident MIR and NIR pulses is described here.
(1). The laser pulse energy was obtained by dividing the power measured using a photo sensor (for NIR) and a thermal sensor (for MIR) purchased from Thorlabs, Inc. by the repetition rate of the regenerative amplifier, 1 kHz.
(2). The peak intensity of incident laser pulse in vacuum was calculated by assuming the Gaussian spatial and temporal profiles.
(3). The peak intensity inside the sample was calculated by multiplying it by the transmittance $|t|^2$ at the interface between the air and the substrate: [142]

$$|t|^2 = |\frac{2}{n_S + 1}|^2 \tag{3.1}$$

where n_S is the refractive index of the substrate. The procedure (3) was not applied for the results for Chapter 3, but Chapter 4.

3.4 Experimental results

3.4.1 Extraction of HSG spectra

We observed HHG spectra at photon energies of $m\hbar\omega_{MIR}$ (m : integer) by irradiating the monolayer with MIR pulses and observed the HSG spectra at photon energies of $\hbar\omega_{NIR} + m\hbar\omega_{MIR}$ (m: integer) by simultaneously applying NIR pulses. Therefore, we obtained the HSG contribution by subtracting the HHG component from the spectra.

Figure 3.5**a** shows total spectra of HSG and HHG (green) and HHG spectra (black) under linearly polarized excitation pulses observed from monolayer MoS_2. The polarization was along the X-direction. The HHG spectra were obtained in the condition that NIR pulses were 10 ps delayed from the MIR pulses. In our experiment, NIR photon energy is about six times larger than the MIR photon energy. Thus, we observed seventh order harmonics at the frequency close to that of the first order sideband. We obtained HSG spectra clearly by subtracting HHG spectra. Figure 3.5**b** shows the spectra under circularly polarized excitation pulses with the same excitation power. In this case, we did not observe HHG. This result is consistent with the previous paper [52]. The HHG from the sapphire substrate was not detectable in our experiment. This may be due to the large difference of the bandgap energy between the TMDs and sapphire. On the other hand, the second-order sideband from the substrate was observed to be typically an order of magnitude smaller than that from the monolayer. This contribution is not subtracted from the displayed spectra. For example, the double peak structure in the second order sideband in Fig. 3.5**b** is due to the signal from the substrate.

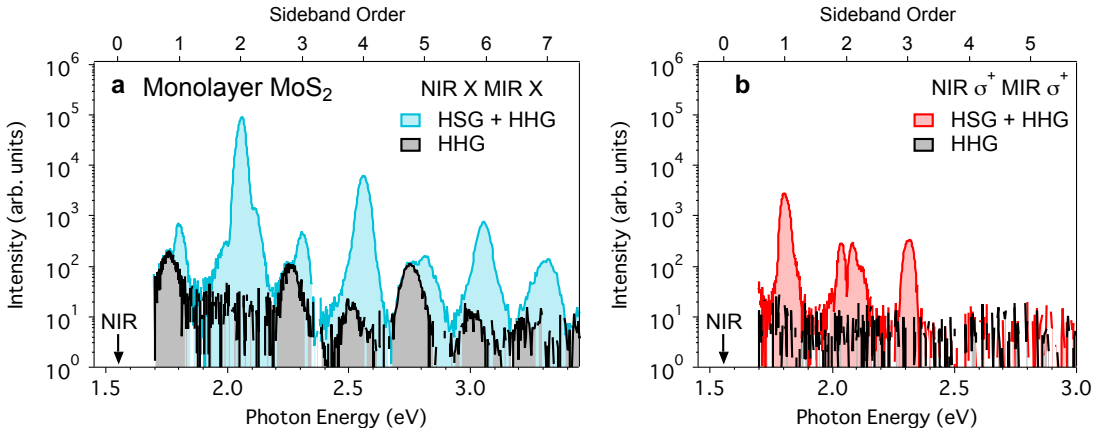

Figure 3.5: Extraction of high-order sideband generation (HSG) spectra. **a** Total spectra of HSG and high-order harmonic generation (HHG) (color) and HHG spectra (black) under linear polarization excitation. **b** Same as a under circular polarization excitation. Reproduced from the supplemental document of K. Nagai *et al.*, Communications Physics **3**, 137 (2020). ©2020 The authors. Distributed under a Creative Commons Attribution 4.0 International license (CC BY 4.0) [1].

3.4.2 HSG spectra obtained from monolayer MoS_2

Figure 3.6 shows polarization-unresolved HSG spectra under linearly and circularly polarized excitation with a MIR-pulse peak intensity of 0.5 TW cm^{-2} and NIR-pulse peak intensity of 0.5 GW cm^{-2}. Here, sidebands up to the seventh order appear under linearly polarized excitations. In contrast, sidebands only up to third order appear under circularly polarized excitation. This difference may arise from the different resultant kinetic energies that coherent electron-hole pairs obtain from linearly and circularly polarized laser fields [13, 86]. On the other hand, we could not observe the lower energy sidebands than NIR photon energy. This may be because the lower energy side is far from the interband resonance of the monolayer MoS_2.

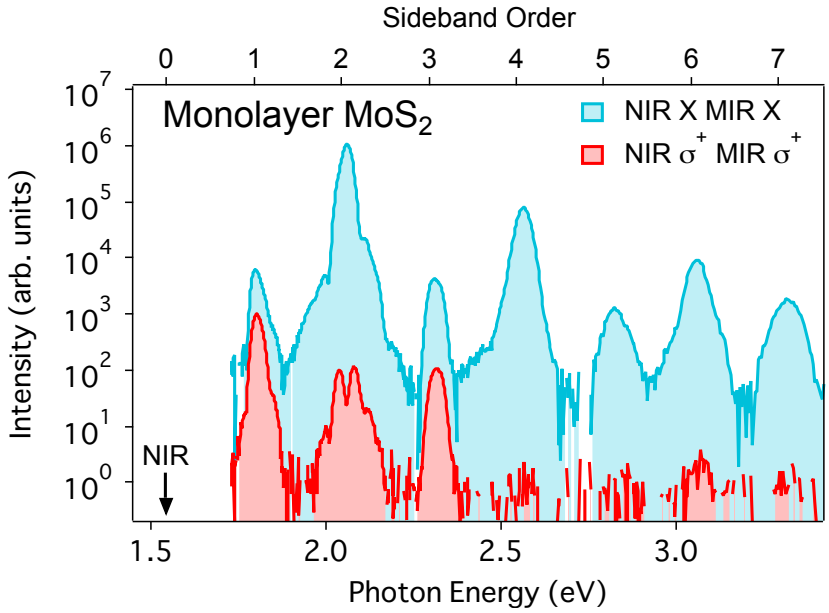

Figure 3.6: High-order sideband generation (HSG) spectra from monolayer MoS_2. Polarization-unresolved HSG spectra measured under linearly polarized (cyan, X-polarized near-infrared (NIR) and mid-infrared (MIR) pulses) and circularly polarized excitation (red, σ^+-polarized NIR and MIR pulses). The intensity of the cyan spectrum is multiplied by 100 for clarity. The black arrow shows the photon energy of the NIR pulses. Reproduced from K. Nagai *et al.*, Communications Physics **3**, 137 (2020). ©2020 The authors. Distributed under a Creative Commons Attribution 4.0 International license (CC BY 4.0) [1].

Nonperturbative aspects induced by MIR light appear in both the spectral shape and excitation power dependence. One such aspect is the non-exponential decay with increasing order in the spectra. Moreover, another aspect appears in the excitation power dependence shown in Fig. 3.7. According to the perturbation theory, the n-th order harmonic intensity is proportional to the n-th power of the incident MIR intensity since the n-th order nonlinear polarization radiates the harmonics. However, the MIR power dependence deviates from the power-law derived from perturbation theory under both linearly and circularly polarized excitations (as shown in Figure 3.7**a**,**b**). On the other hand, the intensity of the sideband is proportional to the NIR probe power (Fig. 3.7**c**,**d**). This indicates the

NIR pulses can be treated as a perturbation.

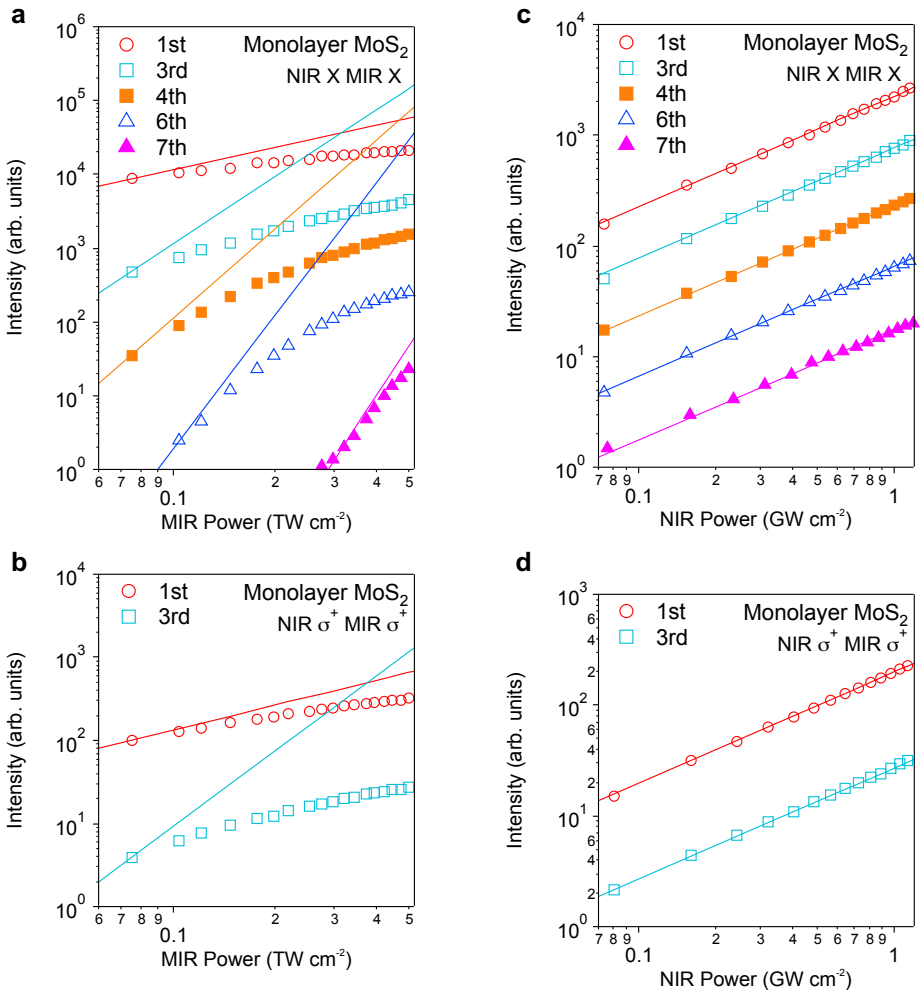

Figure 3.7: Excitation power dependence of high-order sideband generation (HSG) in monolayer MoS2. **a,b** Mid-infrared (MIR) power dependence of HSG under linearly and circularly polarized light. **c,d** Near-infrared (NIR) power dependence of HSG under linearly and circularly polarized light. The power shown in the bottom axis is the peak power of the incident pulse at the focal point in vacuum. The solid lines are eye guides that show the power law. Reproduced from the supplemental document of K. Nagai *et al.*, Communications Physics **3**, 137 (2020). ©2020 The authors. Distributed under a Creative Commons Attribution 4.0 International license (CC BY 4.0) [1].

3.4.3 Polarization selection rule of HSG

Figures 3.8**a-d** shows circular (σ^+, σ^-) polarization-resolved sideband spectra obtained from different combinations of σ^+- and σ^--polarized excitations. The polarization of the sideband depends on the order and the polarization of the excitation pulses. Since we obtained the same result from monolayer $MoSe_2$, which has the same crystal structure,

the selection rules are determined only by the symmetry of the crystal and polarization of the light (Fig. 3.9).

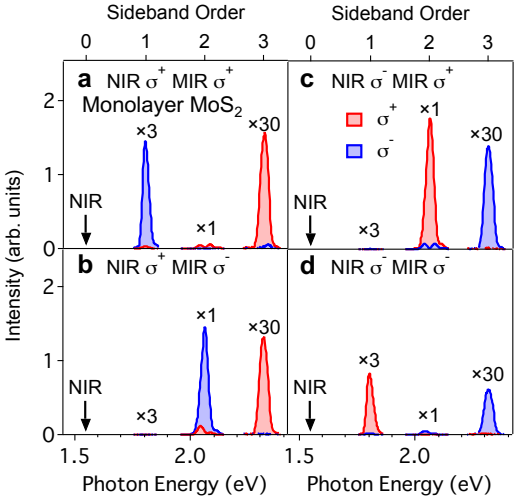

Figure 3.8: Circular polarization-resolved high-order sideband generation (HSG) spectra from monolayer MoS_2. Red and blue shaded areas indicate σ^+-polarized and σ^--polarized spectra, respectively. The sidebands are generated by **a** σ^+-polarized near- infrared and σ^+-polarized mid-infrared pulses (σ^+, σ σ^+), **b** (σ^+, σ^-), **c** (σ^-, σ^+), **d** (σ^-, σ^-). Each order of the sideband is scaled with the indicated number. Reproduced from K. Nagai *et al.*, Communications Physics **3**, 137 (2020). ©2020 The authors. Distributed under a Creative Commons Attribution 4.0 International license (CC BY 4.0) [1].

Furthermore, we systematically examined the linear polarization selection rules. Figures 3.10**a-d** show linear polarization-resolved sideband spectra obtained from different combinations of X and Y-polarized excitations. In particular, when MIR driving pulses are X-polarized (Figs. 3.10**a**,**b**), odd-order sidebands are emitted with a perpendicular polarization to that of NIR pulses and even-order sidebands are emitted with a parallel polarization. On the other hand, when the MIR driving pulses are Y-polarized (Figs. 3.10**c**, **d**), the polarization of the sideband is parallel to that of NIR pulses for all orders.

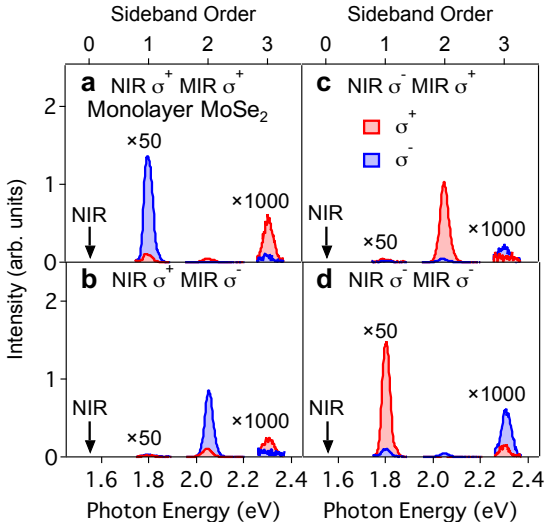

Figure 3.9: Circular polarization-resolved high-order sideband generation (HSG) spectra from monolayer $MoSe_2$. Red and blue shaded areas indicate σ^+-polarized and σ^--polarized spectra, respectively. The sidebands are generated by **a** σ^+-polarized near- infrared and σ^+-polarized mid-infrared pulses (σ^+, σ^+), **b** (σ^+, σ^-), **c** (σ^-, σ^+), **d** (σ^-, σ^-). Each order of the sideband is scaled with the indicated number. Reproduced from the supplemental document of K. Nagai *et al.*, Communications Physics **3**, 137 (2020). ©2020 The authors. Distributed under a Creative Commons Attribution 4.0 International license (CC BY 4.0) [1].

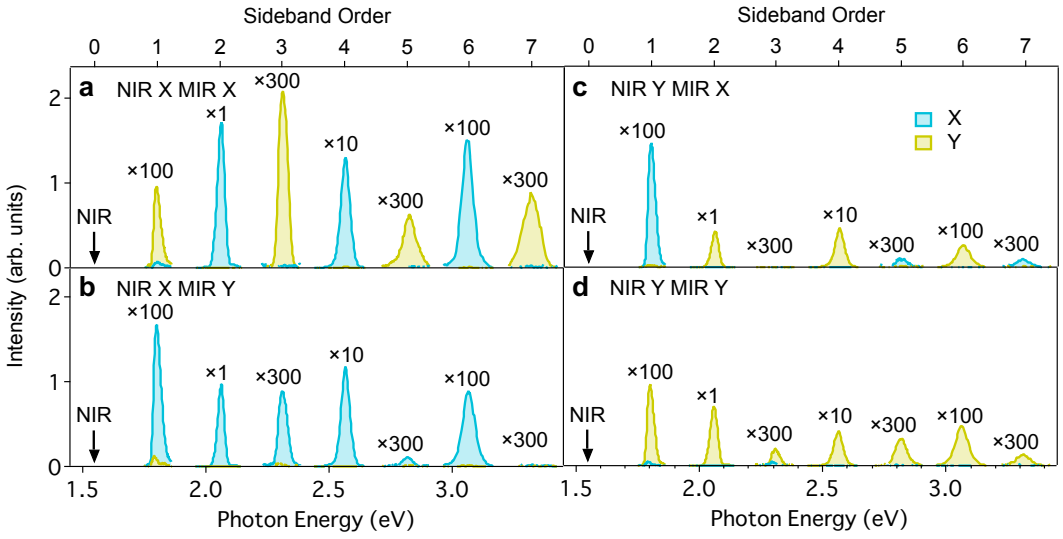

Figure 3.10: Linear polarization-resolved high-order sideband generation (HSG) spectra from monolayer MoS_2. Cyan and yellow areas indicate X-polarized and Y-polarized spectra, respectively. The sidebands are generated by **e** (X, X), **f** (X, Y), **g** (Y, X), **h** (Y, Y). Each order of the sideband is scaled with the indicated number. Reproduced from K. Nagai *et al.*, Communications Physics **3**, 137 (2020). ©2020 The authors. Distributed under a Creative Commons Attribution 4.0 International license (CC BY 4.0) [1].

3.5 Theory

3.5.1 Microscopic description of HSG using Floquet theorem

To explain these selection rules, we propose a simple scheme for symmetry analysis of HSG using the "Raman tensor" and DSs. The conceptual figure of the "Raman scattering" description is depicted in Fig. 3.11. The MIR-light driven electronic state in solids is the scattering center. The NIR light is treated as an incident light, and sidebands are treated as a scattered light from the center.

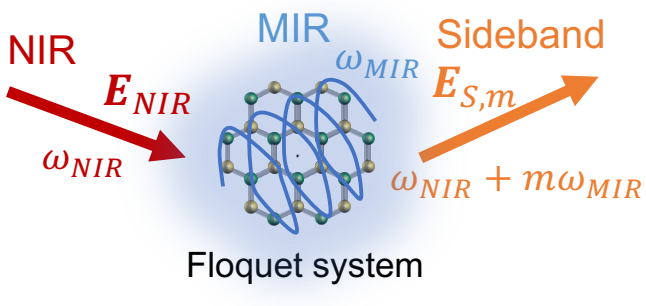

Figure 3.11: Conceptual figure for Raman scattering process in mid-infrared (MIR)-driven Floquet state. The electric fields of the incident near-infrared (NIR) and scattered sidebands are denoted by $\mathbf{E}_{NIR}$, $\mathbf{E}_{S,m}$. The angular frequency of the MIR and NIR, and sidebands are denoted by ω_{MIR}, ω_{NIR}, and $\omega_{NIR} + m\omega_{MIR}$, respectively

In the previous report, HSG selection rules were explained in terms of the symmetry of microscopic intraband dynamics of electron-hole pairs in momentum space [13]. However, it is difficult to extend this microscopic explanation to the circular polarization case or to polarization selection rules in other materials. Below, we show that DS gives us a general tool for symmetry analysis of HSG. To justify the "Raman-scattering" description, we consider a microscopic model of HSG.

We start with a general Hamiltonian of a single electron interacting with an electric field in a solid. Then, we apply the Floquet theorem by assuming periodicity of the MIR driving field and fully coherent time evolution of the system, and by using the perturbation theory for the weak NIR pulses. This assumptions lead to the "Raman-scattering" description.

A single electron Hamiltonian with mass m_e in a crystalline solid interacting with a MIR electric field is given by

$$\hat{H}_0(t) = \frac{1}{2m_e}\left(\hat{\mathbf{p}} - e\mathbf{A}(t)\right)^2 + U(\hat{\mathbf{r}}), \tag{3.2}$$

where e is the electron charge, $\mathbf{A}(t)$ is the vector potential of the external MIR field and $U(\hat{\mathbf{r}})$ is periodic potential in the crystalline solid. Here the spatial distribution of $\mathbf{A}(t)$ is neglected by applying long wavelength approximation. Let us consider the additional

weak NIR electric field, which perturbs the above system. The total Hamiltonian is given by

$$\hat{H}_0(t) = \frac{1}{2m_e}\left(\hat{\mathbf{p}} - e\mathbf{A}(t) - e\delta\mathbf{A}_{NIR}(t)\right)^2 + U(\hat{\mathbf{r}}), \tag{3.3}$$

where $\delta\mathbf{A}_{NIR}(t)$ is the vector potential of the weak NIR field. By using Coulomb gauge $\nabla\cdot\delta\mathbf{A}_{NIR} = 0$ and neglecting the second order of $\delta\mathbf{A}_{NIR}(t)$, the total Hamiltonian is given by

$$\begin{aligned}\hat{H}(t) &= \frac{1}{2m_e}\left(\hat{\mathbf{p}} - e\mathbf{A}(t) - e\delta\mathbf{A}_{NIR}(t)\right)^2 + U(\hat{\mathbf{r}}), \\ &= \hat{H}_0(t) + \delta\mathbf{A}_{NIR}(t)\cdot\hat{\mathbf{J}},\end{aligned} \tag{3.4}$$

where

$$\hat{\mathbf{J}} = -\frac{e}{m_e}\left(\hat{\mathbf{p}} - e\mathbf{A}(t)\right) = \frac{e}{m_e}\left(i\hbar\nabla + e\mathbf{A}(t)\right) = \frac{\partial\hat{H}_0(t)}{\partial\mathbf{A}(t)} \tag{3.5}$$

is defined as the current operator in the velocity gauge. We regard $\delta H = \delta\mathbf{A}_{NIR}(t)\cdot\hat{\mathbf{J}}$ as the perturbation Hamiltonian. First, we consider MIR-driven system $\hat{H}_0(t)$. In our experimental condition, the MIR pulses are intense, coherent laser pulses and have several cycles within their pulse durations. Thus, to simplify the description of HSG, we assume the time periodicity of the MIR field and apply the Floquet theorem explained in Chapter 2 [127]. Note that the Floquet concept is valid in both perturbative and nonperturbative regime. With this assumption, the Hamiltonian $\hat{H}_0(t')$ satisfies the periodicity of the MIR field

$$\hat{H}_0(t) = \hat{H}_0(t + 2\pi/\omega_{MIR}) \tag{3.6}$$

with angular frequency of the MIR light ω_{MIR}. We assume that the electronic system lies in a Floquet eigenstate $|i_F(t)\rangle$ at $t = -\infty$. Next, we consider the temporal evolution of the total system perturbed by the NIR field. Schrödinger equation under the Hamiltonian $H(t)$ is given by

$$i\hbar\frac{\partial}{\partial t}|\Psi(t)\rangle = \left(\hat{H}_0(t) + \delta\hat{H}(t)\right)|\Psi(t).\rangle \tag{3.7}$$

We assume the following ansatz for the wave function:

$$|\Psi(t)\rangle = e^{-i\frac{\varepsilon_{i_F}}{\hbar}t}|i_F(t)\rangle + \sum_{e_F\neq i_F} C_{e_F}(t)\, e^{-i\frac{\varepsilon_{e_F}}{\hbar}t}|e_F(t)\rangle, \tag{3.8}$$

where $|e_F(t)\rangle$ denotes other Floquet eigenstates than $|i_F(t)\rangle$. Here, the coefficient $C_{e_F}(t)$ is small because the NIR light is weak. By considering the first order perturbation, we obtain

$$C_{e_F}(t) = -\frac{i}{\hbar}\int_{-\infty}^{t} dt' e^{i\omega_{ei}t'}\left\langle e_F(t')\right|\frac{\partial\hat{H}_0(t')}{\partial\mathbf{A}(t')}\left|i_F(t')\right\rangle\delta\mathbf{A}_{NIR}(t') \tag{3.9}$$

with $\hbar\omega_{ei} = \varepsilon_{e_F} - \varepsilon_{i_F}$. Here we used the orthogonality of the Floquet eigenstates (that is non-trivial but can be proved). We calculate HSG by considering current induced in the perturbed state $|\Psi(t)\rangle$. The expectation value of the current is given by

$$\begin{aligned}\mathbf{J}(t) &= \left\langle \Psi(t) \left| \hat{\mathbf{J}} \right| \Psi(t) \right\rangle \\ &\simeq \left\langle i_F(t) \left| \hat{\mathbf{J}} \right| i_F(t) \right\rangle + \sum_{e_F \neq i_F} \left(C_{e_F}(t) e^{-i\omega_{ei}t} \left\langle i_F(t) \left| \hat{\mathbf{J}} \right| e_F(t) \right\rangle + c.c. \right), \end{aligned} \tag{3.10}$$

where the second order term of $C_{e_F}(t)$ is neglected. The first term, which is independent of the NIR light field, contributes to HHG [75]. HSG is induced by the second term ($\mathbf{J}_{SG}(t)$) that is proportional to the NIR light field. By substituting eq. (3.9) into eq. (3.10), μ-th component of the polarization current $\mathbf{J}_{SG}(t)$ is given by

$$J_{SG,\mu}(t) = -\frac{i}{\hbar} \sum_{\nu} \sum_{e_F \neq i_F} \int_{-\infty}^{t} dt' e^{-i\omega_{ei}(t-t')} \chi^{e_F}_{\mu,\nu}(t,t') \, \delta A_{NIR,\nu}(t') + c.c. \tag{3.11}$$

with

$$\chi^{e_F}_{\mu,\nu}(t,t') = \left\langle i_F(t) \left| \frac{\partial \hat{H}_0(t)}{\partial A_\mu(t)} \right| e_F(t) \right\rangle \left\langle e_F(t') \left| \frac{\partial \hat{H}_0(t')}{\partial A_\nu(t')} \right| i_F(t') \right\rangle . \tag{3.12}$$

It can be shown that the $J_{SG}(t)$ emits the electric field that has the sideband frequency components (see Appendix A.2).

Equation (3.11) justifies the " Raman scattering " process description depicted in Fig. 3.12. Figure 3.12(a) shows the energy diagram of the conventional Raman scattering process. In conventional Raman scattering (inelastic scattering) in solids, incident light coherently excites an electron from the initial state to an excited state and the electron simultaneously relaxes back to the final state by emitting lower-frequency or higher-frequency light (so-called Stokes and anti-Stokes Raman scattering, respectively). The energy difference between the incident and emitted light is transferred into the solids as the energy of phonons or electrons etc. Figure 3.12(b) shows the energy diagram of the " Raman scattering " process in Floquet systems. In this picture, a NIR photon coherently excites an electron from the initial to an intermediate Floquet state, and the electron simultaneously relaxes back to the initial state by emitting a sideband photon. In this interpretation, the high-order sideband corresponds to " multi-photon anti-Stokes Raman scattering ".

3.5.2 Symmetry constraint on " Raman tensor "

The second rank tensor $\chi^{e_F}_{\mu,\nu}(t,t')$ corresponds to the response function of the Floquet system, which gives the relation between $\mathbf{J}_{SG}(t)$ and $\delta\mathbf{A}_{NIR}(t)$. It should be noticed that not the polarization current $\mathbf{J}_{SG}(t)$ but $\chi^{e_F}_{\mu,\nu}(t,t')$ follows the DS of the MIR-driven Floquet system in the case of HSG selection rule. This is in contrast with the case of HHG selection rules shown in Chapter 2 [98], where the current has the same DS as the Floquet system. One simple way to describe the symmetry restriction on $\mathbf{J}_{SG}(t)$ and $\delta\mathbf{A}_{NIR}(t)$ is to consider a second rank tensor $\mathbf{J}_{SG}(t)\,\delta\mathbf{A}^{\dagger}_{NIR}(t)$. One can derive the invariance of this tensor under the DS operation when $\delta\mathbf{A}_{NIR}(t)$ is an " eigenvector " of the DS operation (see Appendix A.3).

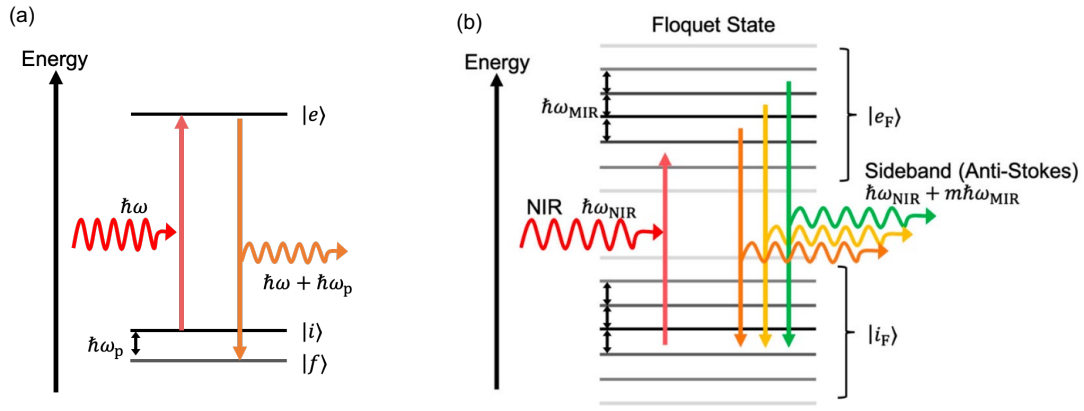

Figure 3.12: Energy level diagram of conventional Raman scattering process. (a) conventional Raman scattering. The energies of the incident photon and scattered photon are written as $\hbar\omega$ and $\hbar\omega + \hbar\omega_p$, respectively. The vertical arrows represent electronic transitions between the initial $|i\rangle$, excited $|e\rangle$ and final state $|f\rangle$ state. (b) Raman scattering process in mid-infrared (MIR)-driven Floquet state. The energies of the near-infrared (NIR) photon and scattered m-th order sideband photon are written as $\hbar\omega_{NIR}$ and $\hbar\omega_{NIR} + m\hbar\omega_{MIR}$, respectively. The vertical arrows represent electronic transitions between the initial Floquet state $|i_F\rangle$ and intermediate Floquet state $|e_F\rangle$. Ladder-like levels with spacing of the MIR photon energy ($\hbar\omega_{MIR}$) denote the quasi-energy levels of the Floquet states. Reproduced from K. Nagai *et al.*, Communications Physics **3**, 137 (2020). ©2020 The authors. Distributed under a Creative Commons Attribution 4.0 International license (CC BY 4.0) [1].

$\mathbf{J}_{SG}(t)$ and $\delta\mathbf{A}_{NIR}(t)$ are directly related to the electric fields of the m-th order sideband $\mathbf{E}_{SG,m}(t)$ and the NIR light $\mathbf{E}_{NIR}(t)$. Therefore, the symmetry restriction can be written in terms of a " Raman tensor " as follows:

$$\mathscr{R}_m(t) = \mathbf{E}_{SG,m}(t)\mathbf{E}^{\dagger}_{NIR}(t) = \begin{pmatrix} E_{SG,m,x}(t)E^{*}_{NIR,x}(t) & E_{SG,m,x}(t)E^{*}_{NIR,y}(t) \\ E_{SG,m,y}(t)E^{*}_{NIR,x}(t) & E_{SG,m,y}(t)E^{*}_{NIR,y}(t) \end{pmatrix}, \quad (3.13)$$

where $E_{SG,m,x}$ and $E_{NIR,x}$ ($E_{SG,m,y}$ and $E_{NIR,y}$) denote the X (Y) component of the electric fields of the m-th order sideband and NIR light, respectively. Here, the direction of the electric field is restricted to being in a two-dimensional space parallel to the monolayer sample in our experimental setup. The " Raman tensor " satisfies the DS of the Floquet system:

$$\hat{X}\mathscr{R}_m(t) = \mathscr{R}_m(t), \quad (3.14)$$

where $\hat{X}$ is a DS operation. Equation (3.14) determines the polarization selection rules of HSG. This equation also supplies a physical insight of HSG selection rules, where the DS of the Floquet system determines the relation between incident and scattered lights. This is similar to the conventional Raman scattering in crystalline solids, where the tensor has the symmetry of the solid and determines the selection rules [143].

3.5.3 Dynamical symmetry operation for the Floquet system

The DS operation of the Floquet system is determined by the symmetry of the monolayer TMDs and the MIR-driving field. Thus, the DS of the system under circularly polarized MIR light is different from that under linearly polarized MIR light.

In this section, DSs under linearly and circularly polarized light in TMDs are derived. To derive all selection rules, all symmetry operations should be considered. The DS operations of the MIR-driven Floquet system in solids are derived as the following procedure:

1. Identify the symmetry of crystal only
2. Identify the symmetry of MIR light only
3. Identify the intersection of the DS groups of the crystal and MIR field

Crystal symmetry of monolayer TMDs

The symmetry operations of crystalline solids are well classified by the crystallographic point group. Monolayer MoS_2 and $MoSe_2$ belong to D_{3h} point group. In our experimental condition, the symmetry in the 2D space parallel to the sample plane is enough to describe the selection rules. The point group to describe the symmetry in the 2D space is generated by two operations $\hat{R}_3$ and $\hat{\sigma}_v$, where $\hat{R}_3$ is a rotation by $2\pi/3$ and $\hat{\sigma}_v$ is a mirror operation for the Mo-S direction in the crystal. Since the symmetry of the crystal is time-independent, the DS groups of the monolayers are generated by $\hat{R}_3$, $\hat{\sigma}_v$, infinitesimal temporal translation, and time-reversal operation.

Dynamical symmetry of MIR light

We describe DS in the product space of time and the 2D space where the polarization is defined. In the following, we determine the DS of the MIR field by checking the invariance under all DS operations given by Neufeld, O. et al. [98].

Case 1— Circularly polarized MIR light We write the electric field of circularly polarized light as follows:

$$\mathbf{E}(t) = \begin{pmatrix} \sin(\omega_{MIR} t) \\ -\sigma_M \cos(\omega_{MIR} t) \end{pmatrix}. \tag{3.15}$$

In this representation, DS group of the MIR light is generated by

$$\hat{D}_y = \hat{T} \cdot \hat{\sigma}_y \tag{3.16}$$

$$\hat{C}_{n,\sigma_M} = \hat{\tau}_{-n\sigma_M} \cdot \hat{R}_n \ (n \to \infty), \tag{3.17}$$

where $\hat{T}$ is time-reversal symmetry operation, $\hat{\sigma}_y$ is mirror symmetry operation with respect to y axis, $\hat{R}_n$ is the spatial rotation by $2\pi/n$, $\hat{\tau}_n$ is the temporal translation by T/n $(T = 2\pi/\omega_{MIR})$, and $\sigma_M = \pm 1$ represent left and right circular polarization of the MIR light respectively. $\hat{C}_{n,\sigma_M}(n \to \infty)$ denotes a DS operation with the infinitesimal spatial rotation and infinitesimal temporal translation.

Case 2— Linearly polarized MIR light We write the electric field of x-polarized light as follows:

$$\mathbf{E}(t) = \begin{pmatrix} 1 \\ 0 \end{pmatrix} \sin(\omega_{MIR} t). \tag{3.18}$$

In this representation, DS group of the MIR light is generated by the following operations

$$\hat{\sigma}_x \tag{3.19}$$

$$\hat{C}_2 \tag{3.20}$$

$$\hat{D}_y \tag{3.21}$$

$$\hat{Z}_y = \hat{\tau}_2 \cdot \hat{\sigma}_y \tag{3.22}$$

$$\hat{H}_x = \hat{T} \cdot \hat{\tau}_2 \cdot \hat{\sigma}_x \tag{3.23}$$

$$\hat{Q} = \hat{T} \cdot \hat{R}_2 \tag{3.24}$$

Similarly, the DS group of the y-polarized light MIR light can be written by substituting x and y.

Dynamical symmetry of MIR driven Floquet state in monolayer TMDs

The DS group of the MIR-driven Floquet state in monolayer TMDs is the intersection of the DS groups of the crystal and MIR field. By comparing the DS groups discussed above, the generators of the DS group of the MIR-driven Floquet state are the followings:

Case 1— Circularly polarized MIR light

$$\hat{C}_{3,\sigma_M}, \hat{D}_y \tag{3.25}$$

Case 2-1— x-polarized MIR light

$$\hat{D}_y, \hat{Z}_y \tag{3.26}$$

Case 2-2— y-polarized MIR light

$$\hat{\sigma}_y, \hat{H}_y \tag{3.27}$$

Here, we show the examples of above operations about $\hat{C}_{3,\sigma_M}$, $\hat{Z}_y$ and $\hat{\sigma}_y$ through schematic figures. Figure 3.13(a) shows how the spatial rotation $\hat{R}_3$ changes the combined system of monolayer TMDs and circularly polarized light. Although the crystal of monolayer TMDs is unchanged under $\hat{R}_3$, the phase of the electric field is shifted by $2\pi/3$. Thus, consequent operation of the temporal translation $\hat{\tau}_{-n\sigma_M}$ restores the system to its original state. Therefore, $\hat{C}_{3,\sigma_M}$ is the DS operation for this case. Figure 3.13(b) shows how the mirror operation $\hat{\sigma}_y$ changes the system under X- or Y-polarized MIR light. The crystal is unchanged under $\hat{\sigma}_y$. The electric field of the X- and Y-polarized light is respectively reversed and unchanged. Thus, the consequent operation of the temporal translation $\hat{\tau}_2$ for X-polarized case restores the system to its original state. Therefore, $\hat{Z}_y$ and $\hat{\sigma}_y$ is the DS operation in X- and Y-polarized cases, respectively.

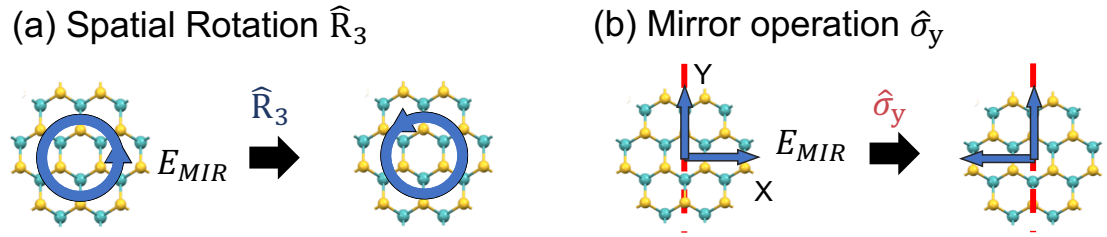

Figure 3.13: Example of DS operation for combined system of mid-infrared (MIR) electric field and monolayer TMDs. (a) Spatial rotation $\hat{R}_3$ for σ^+ circularly polarized case. (b) Mirror operation $\hat{\sigma}_y$ for X- or Y-polarized case. The light blue arrows represents the direction of temporal oscillation of the MIR electric field. The red lines represents the mirror plane.

3.5.4 Dynamical symmetry operation and selection rule of HSG

As shown above, each Floquet system under circularly or linearly polarized field has two DS operations. We derived the symmetry constraint on the selection rules for all symmetry operations, which are summarized in Table 3.1. The detailed derivation of the selection rules is shown in Appendix A.4.

In all cases, one operator more strictly restricts the selection rules than the other operator does. Under circularly polarized light, the DS operator that determines the selection rule is

$$\hat{C}_{3,\sigma_M} = \hat{\tau}_{-3\sigma_M} \cdot \hat{R}_3, \tag{3.28}$$

Table 3.1: DS operation and selection rule of high-order sideband generation. Reproduced from the supplemental document of K. Nagai *et al.*, Communications Physics **3**, 137 (2020). ©2020 The authors. Distributed under a Creative Commons Attribution 4.0 International license (CC BY 4.0) [1].

Dynamical symmetry operation	**Selection rule of HSG**
$\hat{D}_{\mathrm{y}}$	x or y- polarized NIR light ↓ Elliptically polarized sideband light with major or minor axis parallel to the x-axis
$\hat{C}_{n,\sigma_{\mathrm{M}}}$	Circularly polarized NIR light with helicity σ_{N} ↓ Circularly polarized $(\sigma_{\mathrm{M}}(-\sigma_{\mathrm{N}} \pm 1) + nN)$ –th (N : integer) order sideband light with helicity (± 1)
$\hat{Z}_{\mathrm{y}}$	x or y- polarized NIR light ↓ Odd order sideband light polarized perpendicularly to NIR light Even order sideband light polarized in parallel with NIR light
$\hat{\sigma}_{\mathrm{y}}$	x or y- polarized NIR light ↓ Sideband light polarized in parallel with NIR light
$\hat{H}_{\mathrm{y}}$	x or y- polarized NIR light ↓ Elliptically polarized sideband light with major or minor axis parallel to the x-axis

where $\sigma_M = \pm 1$ is the polarization of the MIR driving pulses, $\hat{\tau}_n$ is a temporal translation by T/n (T : the period of the MIR light field) and $\hat{R}_3$ is a spatial rotation by $2\pi/3$. The angle of $2\pi/3$ reflects the three-fold rotational symmetry of the crystal. From equation (3.14) and (3.28), the circular polarization selection rule of the m-th order sideband is derived as

$$m\sigma_M + \sigma_N - \sigma_S^m = 3N, \tag{3.29}$$

where $\sigma_N, \sigma_S^m = \pm 1$ denotes the polarization of the NIR and m-th order sideband, respectively, and N is an integer (see Appendix A.4). Equation (3.29) is consistent with all experimental results in Fig. 3.8.

Equation (3.29) represents the angular momentum conservation rule of light modified in crystalline solids [105, 132, 133]. The $\sigma^+(\sigma^-)$-polarized light can be considered to have spin $+\hbar(-\hbar)$. The left-hand side of equation (3.29) shows the difference between the total spin of the incident photons and the spin of the emitted m-th order sideband photon. Although the right-hand side should be zero in isotropic media, $3N\hbar$ is allowed in monolayer MoS_2, which has three-fold rotational symmetry, due to the rotational analog of the Umklapp process.

The linear polarization selection rule can be derived similarly. The DS of the Floquet system depends on whether the polarization of the MIR pulses is in the X or Y direction, reflecting the mirror symmetry with respect to the Y direction of monolayer MoS_2. The following DS operations determine the selection rules, respectively:

$$\hat{Z}_y = \hat{\tau}_2 \cdot \hat{\sigma}_y \tag{3.30}$$

$$\hat{\sigma}_y, \tag{3.31}$$

where $\hat{\sigma}_y$ means reflection with respect to the Y-direction. Because of the temporal term in equation (3.31), the polarizations of the odd- and even-order sidebands are perpendicular to each other in the X-polarized case. On the other hand, all sidebands have the same polarization in the Y-polarized case (see Appendix A.4). This is consistent with the experimental results in Fig. 3.10. Table 3.2 summarizes the polarization selection rules in each configuration.

3.6 Discussion

3.6.1 Comparison with previous report

Odd-order sidebands in monolayer WSe_2 with Y-polarized MIR pulses were not observed in the previous report, although they were observed in our experiment [13]. This fact does not contradict our selection rules. The difference in the intensity of odd-order sidebands may be attributed to the microscopic electron dynamics depending on the frequency of the excitation pulses. In previous works, the driving field is considered only to induce intraband acceleration of electron-hole pairs. In this work, due to the relatively higher frequency of the MIR pulse, the driving field may also contribute to coherent electron-hole-pair creation, i.e., interband transition, giving rise to the increase of the intensity of the odd-order sidebands. In terms of the “ Raman scattering ” description, the driving field may create a different Floquet state depending on its frequency and determine the efficiency of the scattering process.

Table 3.2: Polarization selection rule of high-order sideband generation in monolayer MoS_2. Allowed polarizations of the sideband are presented for each combination of near-infrared (NIR) and mid-infrared (MIR) polarization. " − " indicates the forbidden sideband order. Reproduced from K. Nagai *et al.*, Communications Physics **3**, 137 (2020). ©2020 The authors. Distributed under a Creative Commons Attribution 4.0 International license (CC BY 4.0) [1].

NIR	σ^+	σ^+	σ^-	σ^-
MIR	σ^+	σ^-	σ^+	σ^-
1st	σ^-	−	−	σ^+
2nd	−	σ^-	σ^+	−
3rd	σ^+	σ^+	σ^-	σ^-
NIR	**X**	**Y**	**X**	**Y**
MIR	**X**	**X**	**Y**	**Y**
Odd	Y	X	X	Y
Even	X	Y	X	Y

Therefore, our results are fully consistent with our work and the previous work in monolayer TMDs [13]. This strongly supports the validity of the DS in strongly light-driven electronic systems in semiconductors.

3.6.2 Application of dynamical symmetry analysis of high harmonic generation

It is noteworthy that equation (3.29) cannot be derived from the DS of the MIR- and NIR-driven crystal using the same analysis as that in the HHG selection rule [98]. The application of such a DS analysis gives few symmetry restrictions on HSG selection rules. Similar to the DS analysis of HHG under two-color laser field [95], one can consider the DS of the crystal under the sum of the MIR and NIR laser field. However, except the case where the frequency of the two-color laser has a simple integer ratio (or a rational ratio), it is hard to find a DS operation that governs the light-driven system, giving rise to no restriction for the polarization selection rule.

To demonstrate this issue, we will show the selection rule in the special case where frequencies of the two-color laser have a simple integer ratio. Even in such a case, the DS of the MIR- and NIR-driven system provides only looser selection rules than that given by the DS analysis on the "Raman tensor" shown in this study. Let us take the frequency of the NIR field to have a six times larger value than that of the MIR field and both fields to have circular polarizations. We write the two-color field as

$$\mathbf{E}(t) = \begin{pmatrix} \sin(\omega_{MIR}t) + \sin(6\omega_{MIR}t) \\ -\sigma_M \cos(\omega_{MIR}t) - \sigma_N \cos(6\omega_{MIR}t) \end{pmatrix}. \tag{3.32}$$

The DS group of the two-color field is generated by

$$\hat{D}_y,\ \hat{C}_{5,\sigma_M} \quad (\sigma_N = \sigma_M) \tag{3.33}$$

$$\hat{D}_y,\ \hat{C}_{7,\sigma_M} \quad (\sigma_N = -\sigma_M) \tag{3.34}$$

Thus, the intersection of the DS group with that of the crystal is only generated by $\hat{D}_y$. According to Table 3.1, $\hat{D}_y$ does not restrict the circular polarization selection rule observed in this work. In this study, the intensity of the NIR field is restricted to the perturbative regime, and HSG is treated as a light scattering process in a MIR-driven Floquet system, which allows us to describe the HSG selection rules.

3.6.3 Validity of dynamical symmetry in solids

In our theoretical formalism, dephasing and relaxation are not included, which may affect the time-translation symmetries [58]. However, the effect of the dephasing on DS should be negligible as the selection rules are well explained by the DS without dephasing in this study. The dephasing effect should be more important and relevant for HHG and HSG in the metallic or strongly correlated electronic system where the electron-electron scattering takes place much faster than that in semiconductors.

In addition, it is noteworthy that the DS operations that govern the selection rules do not include the time-reversal operation but include the time-translational symmetry. In this study, it is unclear whether the time-reversal operation is valid in the strongly MIR-light-driven system, e.g., $\hat{D}_y$ and $\hat{H}_y$. The HSG selection rules derived from these operations are looser than that derived from $\hat{C}_{3,\sigma_M}$, $\hat{Z}_y$ and $\hat{\sigma}_y$ as shown in Appendix A.4. Further study should explore whether such DS holds for solids, considering the relationship with pulse duration and material properties.

3.6.4 Raman scattering description and sideband intensity

The physical picture of HSG as a Raman scattering in Floquet systems is also related to understanding the intensity distribution of the sidebands. In the case of conventional Raman scattering by phonons, the intensity of the Stokes and anti-Stokes lines can be explained by the thermal distribution of the phonon. However, in the case of HSG, we have to consider ladder-like structures of the Floquet states depicted in Fig. 3.12 and the transition between the states. In addition, we have to consider all the electronic band structures related to the transitions around the sideband peak energy. Thus, our physical picture of HSG does not offer a simple understanding of sideband intensity in HSG. However, this picture provides an intuitive understanding of the polarization selection rule.

3.7 Summary

In conclusion, we have systematically determined the circular and linear polarization selection rules of HSG in monolayer MoS_2. By combining the concepts of Floquet and perturbation theory, we devised a new description of HSG as a “Raman scattering” in the MIR-driven Floquet state and revealed that the selection rules of HSG can be comprehensively understood in terms of DS. DS has the potential to describe topological phases and classify Floquet systems such as Floquet topological insulators [96, 137]. Thus, our results pave the way for experimental studies of electronic structures and their topological properties of Floquet systems through light-scattering experiments and DS analyses.

Chapter 4

Effect of incoherent electron-hole pair on HHG

4.1 introduction

Nonperturbative light-matter interactions of electrons in solids reveal a variety of coherent dynamics that cannot be understood within the framework of perturbation theory [8, 33]. A basic understanding of the mechanism underlying HHG is crucial for the study of non-perturbative light-matter interaction in solids. A number of theoretical studies have treated light-driven coherent electrons and holes to describe the mechanism in terms of intraband and intraband mechanisms [38, 40]. Theoretically, harmonics above the band gap energy are mainly generated by the interband mechanism in an MIR field [68]. On the other hand, the intraband mechanism mainly contributes to lower order harmonics [68]. In solids, many-body effects beyond the above single-active electron picture, such as electron-electron scattering, may strongly affect the properties of HHG [38, 41, 68]. However, achieving a deeper understanding of the HHG mechanism, such as one disentangling the contributions of the different processes, remains a challenge because of the inseparable carrier generation and acceleration processes due to a single MIR pulse.

4.1.1 Many-body effects in HHG

Many-body effects are one of the current research targets of solid-state HHG. In atomic gases, the electron-electron correlation is a minor effect and almost all characteristics can be explained by single-electron dynamics based on the three-step model [24] except for the case in xenon gases [144, 145]. In contrast, in solids, many-body effects become remarkable due to a large number of electrons simultaneously excited in a solid.

The importance of many-body effects has been pointed out by theoretical studies at various levels [74, 86, 90, 146–152]. For example, the scattering of electron-hole pairs randomizes the phase of the interband polarization and the carrier distributions in k-space. These processes create incoherent carriers, as has been confirmed by the appearance of photoluminescence in HHG measurements [37, 38]. Such scattering processes have been discussed phenomenologically by using numerical calculations [38, 41, 68]. Especially, the dephasing process that occurs in a sub-cycle timescale of the driving field is usually used to obtain clean harmonic spectra [67, 153].

4.1.2 Photo-carrier doping experiment

Here, a photo-carrier-doping experiment would be particularly useful for clarifying the HHG mechanism [154]. Photo-carrier doping can be used to separately control the extent of carrier generation and thereby clarify the roles of the excited carriers. Figure 4.1 schematically shows a photo-carrier doping experiment. A near-infrared (NIR) pulse is applied to a sample to create electron-hole pairs. After a long enough time passes for the electron-hole pairs to become incoherent, a strong MIR pulse is applied to the sample to generate high harmonics. These photo-carriers add to the incoherent carriers excited by the MIR pulse, and they enhance or suppress the harmonic intensity (Fig. 4.2).

The photo-carrier doping may enhance the intraband current by increasing the total number of incoherent carriers driven by the strong field as suggested by a gating experiment [84]. The magnitude of the intraband contribution in the HHG process can be estimated from the extent of harmonic intensity enhancement. In contrast, the photo-carriers may suppress the interband polarization since they disturb the carrier generation process in the MIR field (through the phase-space filling effect explained in Chapter 2). This effect is deemed to be a major factor in the experimentally observed reduction of harmonics [154]. Photo-carrier doping may also promote excitation-induced dephasing (EID), which is a carrier density-dependent electron-electron scattering effect, and also suppress the interband polarization [155]. This effect has been used to explain the broadening of the homogeneous linewidth of excitons in semiconductors [156–158]. We thus should be able to address the mechanism on HHG by experimentally evaluating changes in harmonic intensity due to photo-carrier doping and systematically examining the above effects in a theoretical calculation. Such a systematic study has not been performed until now.

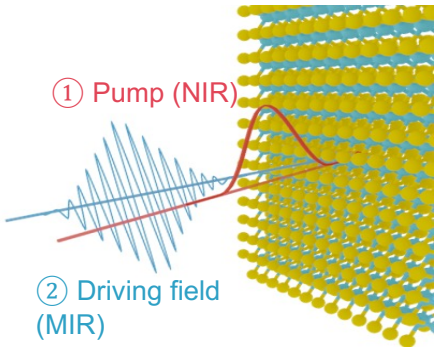

Figure 4.1: Schematic configuration for measurement of effect of photo-carrier doping on HHG. First, photo-carriers are generated by a near-infrared (NIR) pulse. After a long enough time passes for the photo-carriers to become incoherent, high harmonics are generated by a strong mid-infrared (MIR) driving field.

4.1.3 Purpose and composition

In this study, we conducted pump-probe experiments and numerical simulations to explore the effect of incoherent electron-hole pairs on HHG. The photo-carrier-doping experiment indicated an enhancement of harmonics at fifth order and reductions at seventh

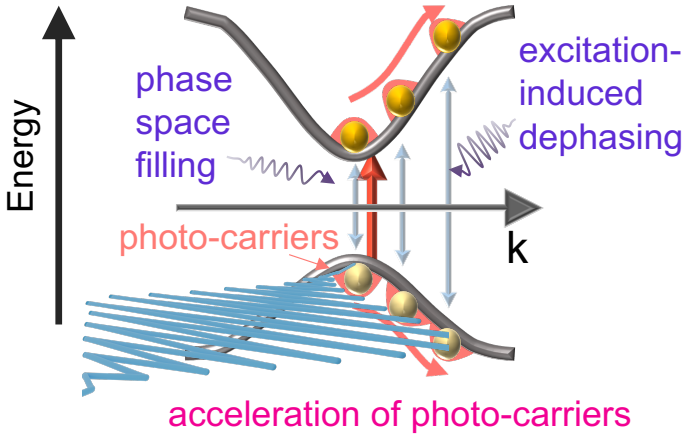

Figure 4.2: Schematic diagram of photo-carrier doping effect. Intraband current may be enhanced due to acceleration of the photo-carriers in the MIR field. Interband polarization may be suppressed due to phase-space filling and excitation-induced dephasing.

and higher orders. The numerical calculations incorporating the distribution of the photo-carriers and electron-electron scattering systematically explored the effect of incoherent carrier doping. We found that the lower order harmonics below the bandgap are enhanced by intraband acceleration of the incoherent photo-carriers, whereas the enhancement is dampened by a momentum relaxation process. We also found that the origin of the suppression of interband polarization above the bandgap is EID rather than the phase-space filling effect. Our numerical calculations suggest that incoherent carriers generated by a strong driving field should strongly suppress the efficiency of generating higher-order interband harmonics.

This chapter is organized as follows. Section 4.2 and 4.3 describes our samples and the experimental setup. Section 4.4.1 presents the results of pump-probe spectroscopy experiments to estimate the photo-carrier density inside the sample against the pump fluence and pump-probe time delay. Section 4.4.2 describes the experimental investigation of the photo-carrier doping effect of the photo-carriers on the harmonic generation. The method of the numerical simulation is presented in Section 4.5, and the results of the full calculation are shown in Section 4.6.1. The effects of the initial carriers, momentum relaxation, EID, and excitons on the photo-carrier doping are systematically discussed by using switch-off analyses in Section 4.6.2. Section 4.6.3 discusses contributions of incoherent carriers generated by the MIR driving field.

4.2 Sample

We purchased a bulk WSe_2 crystal from 2D Semiconductors Inc.. We fabricated an isolated monolayer WSe_2 sample on a sapphire substrate by using the mechanical exfoliation and dry transfer method (Fig. 4.3). The sample preparation was performed by Dr. Satoshi Kusaba by the following procedure.

1. Prepare a bulk sample and exfoliate it with adhesive tape in air.
2. Peel back and forth between the tapes until the monolayer appears on the tape. Monolayer samples were determined from the optical image of the microscope on the tape.
3. Transfer the monolayer onto a sapphire substrate.
4. With the tape stuck to the substrate, place the substrate on a hot plate and heat it at 60°C for about 10 minutes. This weakens the adhesion between the sample and the tape.
5. Slowly remove the tape from the substrate on the hot plate.

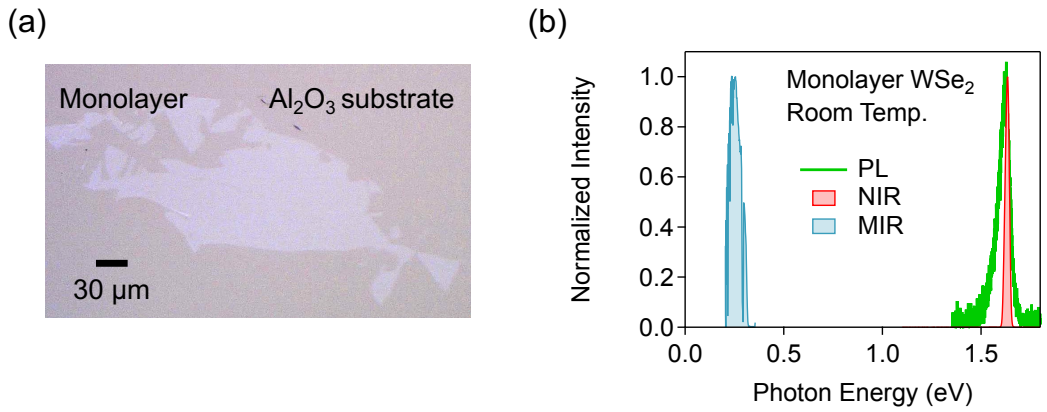

Figure 4.3: Sample and experimental setup. (a) Photograph of WSe_2 monolayer sample on sapphire substrate. (b) Photoluminescence spectrum of monolayer WSe_2 and mid-infrared and near-infrared pulse spectra.

The photoluminescence (PL) spectra were taken by a commercial micro PL spectrometer (NanoFinder30, Tokyo Instruments Inc.) at room temperature. The wavelength of the excitation laser was 532 nm. The PL spectra were used to determine the photon energy for the photo-carrier doping. A typical PL spectrum of the monolayer WSe_2 sample is shown in Fig. 4.3(b), which was obtained after the HHG measurement. The PL peak is located at 1.63 eV, which corresponds to the A-exciton energy of the monolayer WSe_2 [112]. The position of the A-exciton energy of monolayer WSe_2 is lower than that of monolayer MoS_2 as shown in Fig. 1.12. Thus, we can excite this A exciton, with the frequency of the fundamental light from our Ti:sapphire regenerative amplifier. This is the reason why monolayer WSe_2 was used for this experiment. In the following, the A-exciton energy is defined as the absorption edge.

To evaluate the sample degradation under the strong MIR irradiation, we confirmed the PL spectra at 293 K and 6 K before and after HHG measurements as shown in Figs. 4.4(a) and 4.4(b). At both temperatures, we observed a clear decrease in the PL intensity due to the MIR irradiation. Before the MIR irradiation (red), PL peaks, including the exciton (X_0), charged exciton (X*), and possibly the intervalley exciton or dark exciton phonon replica peaks (X_i), are obtained at 6 K [159]. After finishing all experimental procedures (blue), only the broad PL peak of the localized excitons (Loc.) is observed at 6 K and intensity of the localized exciton luminescence decreases drastically at 293 K. These results indicate that defect formation should take place extensively by the strong MIR pulses. However, it is noteworthy that we found no clear decrease in HHG efficiency

throughout our HHG measurement. This is because the efficiency of PL, which is accompanied by the diffusion process, is more sensitive to the defect density than the efficiency of HHG.

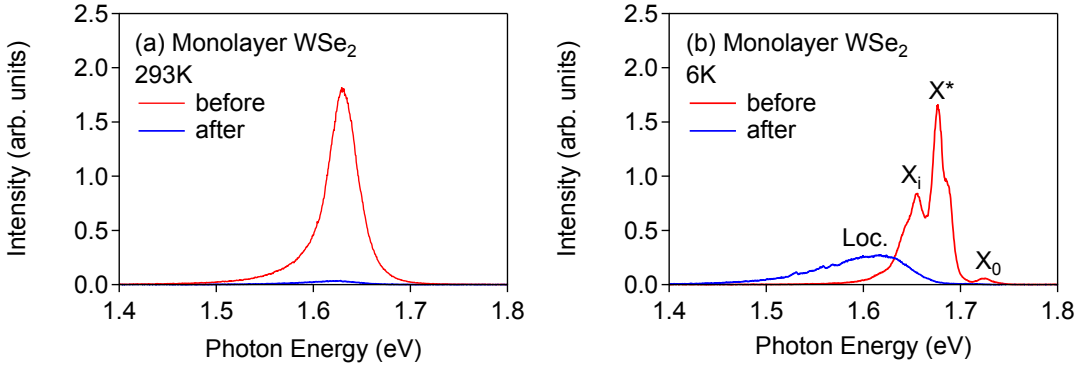

Figure 4.4: Photoluminescence (PL) spectra of monolayer WSe_2 before (blue) and after (red) the irradiation of strong mid-infrared (MIR) pulses at (a) 293K and (b) 6K. The sample was loaded in a flow liquid helium cryostat and the spectra are obtained by a commercial micro-PL spectrometer (NanoFinder30, Tokyo Instruments Inc.). The PL intensity decreases from before to after the MIR irradiation at both temperatures. The PL spectrum at 6K before the MIR irradiation exhibits sharper peaks than that after the MIR irradiation, including free exciton (X_0), charged exciton (X*) and possibly intervalley exciton or dark exciton phonon replica (X_i). The PL spectrum after the MIR irradiation is dominated by the broad peak of the localized excitons (Loc.).

4.3 Experimental setup

Figure 4.3(a) shows the optical setup for degenerate NIR pump-probe spectroscopy of the photo-carrier dynamics. Part of the output from a Ti:sapphire based regenerative amplifier (photon energy 1.55 eV, 35 fs pulse duration, 1 kHz repetition rate, 7 mJ pulse energy) was passed through a bandpass filter to choose the resonant photon energy with the A-exciton energy (1.63 eV, bandwidth: 10 nm). The spectrum of the NIR pulse is shown in Fig. 4.3(b). This bandwidth corresponds to a pulse duration of 100 fs. The pump and probe beams were set to have linear polarizations perpendicular to each other. The spot sizes of the pump and probe NIR pulses in the focal plane were respectively 60 μm and 30 μm, full width at half maxima (FWHM) assuming a Gaussian profile. The pump beam was dumped by an iris and a polarizer after it went through the sample. The transmitted probe beam was detected by a photo-detector and read out by a lock-in amplifier tuned at a chopper frequency of 500 Hz.

Figure 4.5(b) shows the setup for the optical pump and HHG-probe measurement to examine the effect of photo-carrier doping on the HHG. The setup is basically the same as the one in Chapter 3. The same regenerative amplifier was used to pump an optical parametric amplifier (TOPAS-C, Light Conversion). Strong MIR pulses (photon energy

0.26 eV) were obtained by difference frequency generation (DFG) of the signal and idler beams in an $AgGaS_2$ crystal. The signal and idler beams were blocked by a long-pass filter (LPF) with a cutoff wavelength of 4 μm. The spectrum of the MIR pulse is shown in Fig. 4.2(b). The photon energy far below the resonance with the absorption edge of the monolayer WSe_2 was chosen to avoid damaging the sample in the strong field. The pulse duration was estimated to be 60 fs in a cross-correlation measurement as shown in Appendix A.1. The same NIR pump pulses as in Fig. 4.5(a) were used for the photo-carrier doping. The NIR and MIR pulses had a linear polarization parallel to each other. The NIR light was spatially separated and blocked by an iris placed behind the sample. The NIR and MIR pulse spot sizes were 60 μm and 30 μm (FWHM), respectively. High harmonics were spectrally resolved by a grating spectrometer (Kymera 193i, Andor) and measured by a Si charge-coupled device camera (DU920P-OE, Newton). The scattered component of the NIR light was blocked by a 750-nm short-pass filter (SPF) when measuring the seventh and higher order harmonics or by an 850-nm LPF when measuring the fifth-order harmonics. The efficiency of the spectrometer is corrected by the same procedure as that in Chapter 3. All the degenerate pump-probe measurements and HHG measurements were performed in air at room temperature.

4.4 Experimental results

4.4.1 Degenerate NIR pump-probe measurement

We performed a degenerate NIR pump-probe experiment to estimate the photo-carrier density for the excitation condition resonant with the A-exciton energy. Figure 4.6 shows the dependence of the differential transmission signal on the time delay. The differential transmission (ΔT) is normalized by the transmission of the probe pulse without the pump pulse (T). The inset in Fig. 4.6 shows the overall measured data at four excitation fluences at 40, 80, 160, 320 μJ cm^{-2}. Increases in transmission ($\Delta T/T > 0$) were obtained in all experiments. This indicates the absorption saturation of the probe pulse was due to the phase-space filling effect. The spike-like signal observed near the time origin may reflect a coherent nonlinear process caused by the pump and probe pulses. Thus, we only evaluated the decay curves after the spikes shown in the main panel of Fig. 4.6.

The decay rate of $\Delta T/T$ increases with increasing pump fluence. This indicates that the relaxation process becomes faster nonlinearly with respect to the carrier density. The exciton-exciton annihilation (EEA) process occurs in TMDs around an excitation fluence 40 μJ cm^{-2}, as reported by Refs. [124,160]. The EEA process is the carrier decay mechanism different from the ordinary recombination of electron-hole pair. When two excitons collide, the energy of the one exciton is transferred into the other exciton with conserving total energy and momentum of the excitons. Thus, the probability of the EEA process is proportional to the square of the exciton density. In addition, $\Delta T/T$ does not increase proportionally to the pump fluence, which indicates saturation of the carrier generation by the pump pulse. This saturation arises from the phase-space filling effect for the NIR pump pulse.

By considering these two effects, we fitted the data with the following function:

$$\frac{\Delta T}{T} = \frac{\hbar\omega_N}{F_S}\frac{2}{n_S+1}N(t) \tag{4.1}$$

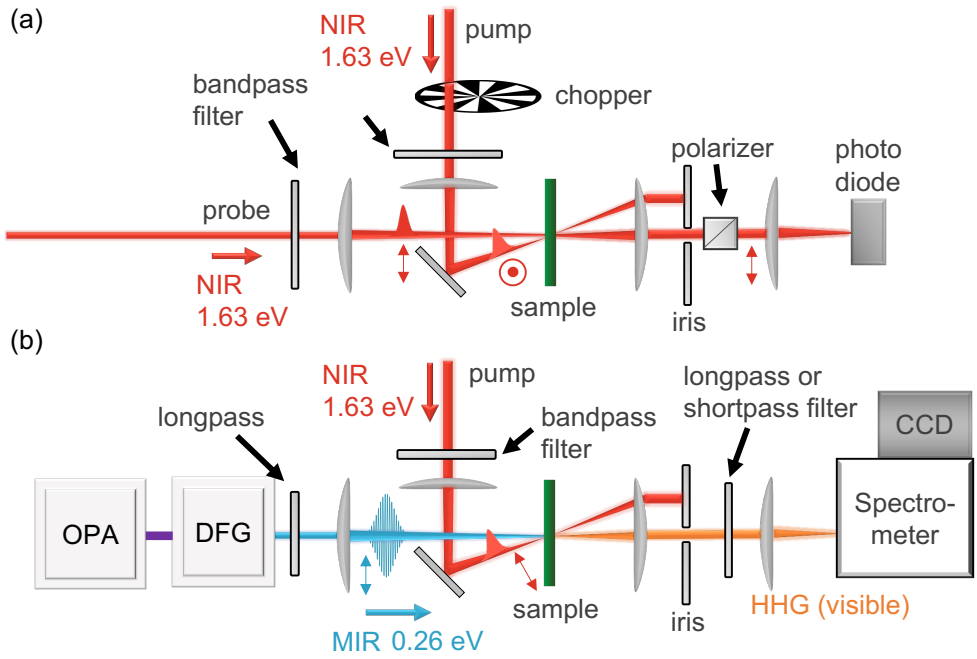

Figure 4.5: Experimental setup. (a) Experimental setup of degenerate near-infrared pump-probe measurement. The laser source is a Ti:sapphire regenerative amplifier (photon energy 1.55 eV, 35 fs pulse duration, 1 kHz repetition rate, 7 mJ pulse energy). The near-infrared (NIR) pump and probe beams passed through bandpass filters (1.63 eV) and are incident on the sample with perpendicular polarizations to each other. The transmittance of the probe beam is measured by a photo diode and read out by a lock-in amplifier. (b) Experimental setup for measuring the effect of photo-carrier doping on high harmonic generation (HHG). The NIR pump (1.63 eV) and strong mid-infrared (MIR) beams (0.26 eV) are incident on the sample with parallel polarizations to each other. The harmonic spectra are resolved by a spectrometer and measured by a Si-CCD camera (OPA: optical parametric amplifier, DFG: difference frequency generation).

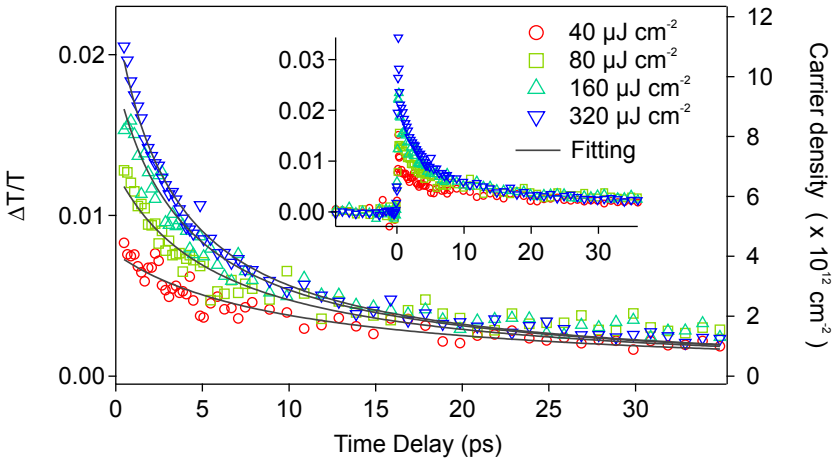

Figure 4.6: Photo-carrier relaxation dynamics at room temperature. (a) Dependence of normalized differential transmission on time delay for four excitation fluences (40, 80, 160, 320 μJ cm^{-2}). Black solid lines are fitting curves assuming the exciton-exciton annihilation (EEA) process and absorption saturation of the pump pulse. Inset : full range data. The fitting result of the EEA rate is $k_A = (2.46 \pm 0.10) \times 10^{-2}$ cm^2 s^{-1} and the saturation fluence is $F_S = (1.014 \pm 0.039) \times 10^2$ μJ cm^{-2}. The right axis represents the corresponding carrier density. The carrier density of 1.1×10^{13} cm^{-2} is close to the carrier number of 0.01 per unit cell.

where

$$N(t) = \frac{N_0}{1 + k_A N_0 t}, \tag{4.2}$$

is the carrier (exciton) density in the 2D sample plane at the time delay t assuming the EEA process and

$$N_0 = \frac{A F_S}{\hbar\omega_N} \left(1 - \exp\left(-\frac{F_N}{F_S}\right)\right) \tag{4.3}$$

is the carrier density at the time origin considering the saturation of the carrier generation by the pump pulse (a detailed derivation is given in Appendix A.1). $\hbar\omega_N = 1.63$ eV is the photon energy of the NIR pulse, F_S is the saturation fluence, F_N is the pump fluence, k_A is the EEA rate, A is the absorbance of the monolayer WSe_2, and $n_S = 1.76$ is the refractive index of the sapphire substrate [161]. A global fitting using eqs. (4.1)-(4.3) was performed on the four measured data with F_S, k_A, A as common free parameters. The fitting results are summarized in the Table 4.1.

Table 4.1: Fitting results for Figure 4.6

parameter	fitting result
A	0.03220 ± 0.00070
k_A	$(2.46 \pm 0.10) \times 10^{-2}$ cm^2 s^{-1}
F_S	$(1.014 \pm 0.039) \times 10^2$ μJ cm^{-2}

The fitting results are displayed in Fig. 4.6 by black curves. The fitting curves successfully explain the all decay curves. The fitting results are summarized in Table 4.1. The rate $k_A = (2.46 \pm 0.10) \times 10^{-2}$ cm^2 s^{-1} matches well with that reported in Refs. [124,160]. In general, the EEA is dependent on the surrounding environment for the monolayer [162]. Our result is in particular consistent with the value reported for monolayer WSe_2 on a sapphire substrate. Furthermore, this result validates the estimation of the photo-carrier density. The right axis in Fig. 4.6 shows the carrier density estimated using eq. (4.1) and the fitting result of $F_S = (1.014 \pm 0.039) \times 10^2$ μJ cm^{-2}. The estimated carrier density in Fig. 4.6 is smaller than the value at which the bandgap renormalization becomes remarkable in monolayer TMDs ($N > 10^{13}$-10^{14} cm $^{-2}$) [125]. In the next section, we will mainly examine the results on photo-carrier doping at a pump fluence of 40 μJ cm^{-2} (corresponding to the red circle in Fig. 4.6) to avoid dealing with the bandgap renormalization.

4.4.2 Measurement for photo-carrier doping effect on HHG

Figure 4.7(a) shows the fifth to twelfth HHG spectra with and without photo-carrier doping. The polarization of the driving MIR pulses was along the zigzag direction (inset of Fig. 4.7(a)). The crystal axis was determined by the polarization selection rules of HHG [44, 52]. The peak intensity of the MIR pulse was 0.092 TW cm^{-2} inside the sample, which was calculated by considering the incident pulse intensity, spot sizes, pulse duration and refractive index of the sapphire substrate [161]. Even-order harmonics appeared because of the broken inversion symmetry of the monolayer [44, 52]. The time delay was set at 1 ps to prevent consecutive pulses from overlapping, and the pump fluence was set to 40 μJ cm^{-2}, which corresponds to a photo-carrier density of 3.7×10^{12} cm^{-2}. We observed a clear difference in harmonic intensity induced by the pump pulse. Figure 4.7(b) shows the differential harmonic intensity normalized by the each order of harmonic intensity ($\Delta I/I$). The intensity I is calculated by averaging the harmonic spectra over their spectral widths (FWHM). In the energy region lower than the absorption edge (1.63 eV), we observed a small increase in the intensity of the fifth order harmonics. A previous experiment using a bulk crystal did not find any enhancement due to photo-carrier doping; instead, a suppression was observed [154]. In our case, the enhancement may be due to our use of an ideally thin sample. In contrast, the higher order harmonics are clearly suppressed, and the degree of suppression becomes larger as the order increases. We found no clear difference between odd and even harmonics. Figures 4.7(c) and 4.7(d) show results for measurement in the armchair direction (see Fig. 4.7(d) inset). The differential harmonic intensity in Fig. 4.7(d) shows a similar trend to the one for the zigzag direction. These results suggest that the differential harmonic intensity is determined solely by the energy of the harmonics relative to that of the absorption edge.

To confirm the relation between the HHG and photo-carrier dynamics, we measured the differential harmonic intensity as a function of the time delay using zigzag and armchair polarized pulses at 40 μJ cm^{-2} (Figs. 4.8(a) and 4.8(b)). A positive time delay means that the NIR pump pulse arrives at the sample before the MIR pulses. In both experiments, the signal appeared as a staircase around the time origin, and it decreased on a timescale of about 10 ps. This timescale well matches the one of the photo-carrier dynamics in Fig. 4.6.

To evaluate the dependence of the differential harmonic intensity on the photo-carrier

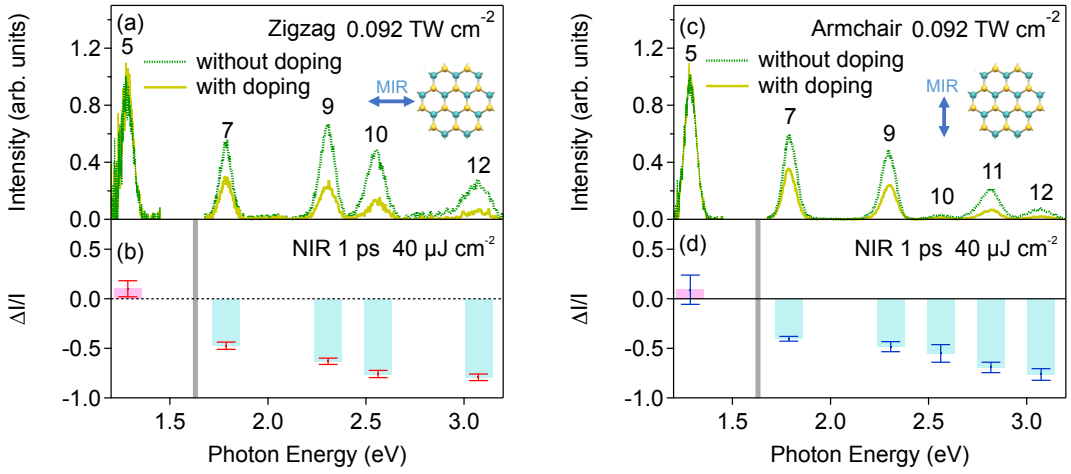

Figure 4.7: Effect of photo-carrier doping on high harmonic generation in monolayer WSe_2 at room temperature. (a,d) Harmonic spectra induced by intense mid-infrared (MIR) pulse polarized along (a) zigzag and (d) armchair direction. Green dotted and yellow solid spectra were respectively obtained without and with near-infrared (NIR) pump pulses. The inset is a top view of the crystal structure of monolayer WSe_2 and the light blue arrow represents the polarization of the MIR pulses. (b,d) NIR-pump-induced differential harmonic intensity under (b) zigzag and (d) armchair polarized MIR pulses. The time delay and the NIR pump fluence were set to 1 ps and 40 μJ cm^{-2}, respectively. The error bars represent standard deviations. The indicated numbers in (a) and (c) represent the order of the harmonics. The gray lines in (b) and (e) show the A-exciton energy where the photo-carriers are excited by the NIR pulses.

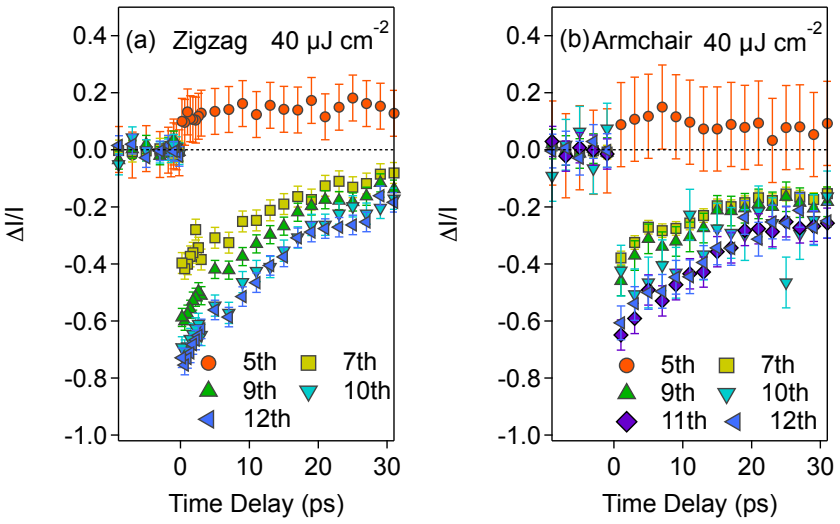

Figure 4.8: Dependence of the differential harmonic intensity on time delay under (a) zigzag and (b) armchair polarized mid-infrared pulses with pump fluence of 40 μJ cm^{-2}. The error bars represent standard deviations calculated by assuming that the deviations are independent of the time delay.

density, we converted the NIR fluence dependence and the time delay dependence by using the fitting results of eqs. (4.1)-(4.3). The dependences in Figs. 4.9(a) and 4.9(b).were obtained at a delay of 1 ps and at an NIR pump fluence of 320 μJ cm^{-2}, respectively. The figures show good agreement between the data and indicate that the observed differential HHG signal is determined only by the carrier density at the time when the MIR pulses arrive, and other photo-excitation effects on HHG are negligible. We observed a monotonic decrease for higher order harmonics but a non-monotonic trend for the fifth-order harmonics at higher pump fluences. For the carrier density estimation, we neglected the effect of the multiple reflections from our optical system that cause the small dip near 7 ps in Fig. 4.9(b).

Since the MIR field itself creates electron-hole pairs, the effects of the photo-carriers generally depends on the MIR intensity and underlying HHG mechanism. We measured the MIR intensity dependence of the differential harmonic intensity using zigzag polarized pulses, as shown in Fig. 4.10. The photo-carrier density was estimated to be 3.7×10^{12} cm^{-2} under a pump fluence of 40 μJ cm^{-2} and delay of 1 ps. There was no significant change in differential harmonic intensity with respect to the MIR intensity, especially for the seventh and higher harmonics. The increase in the fifth order was relatively large at lower MIR intensities. The signal-to-noise ratio became worse at intensities below 0.04 TW cm^{-2}. These experimental data will be compared with the numerical simulations in Sections 4.6.1 and 4.6.3.

We concluded that the observed decreases in harmonic intensity were not due to screening of the MIR field by the photo-carriers. We measured the transmittance of the MIR pulses under the same conditions as those of the experiment in Fig. 4.7(b). The transmission loss due to the photo-carrier doping was less than 1%. This effect is not large enough to reduce HHG, given that the HHG is proportional to the cube of the MIR intensity [44, 52].

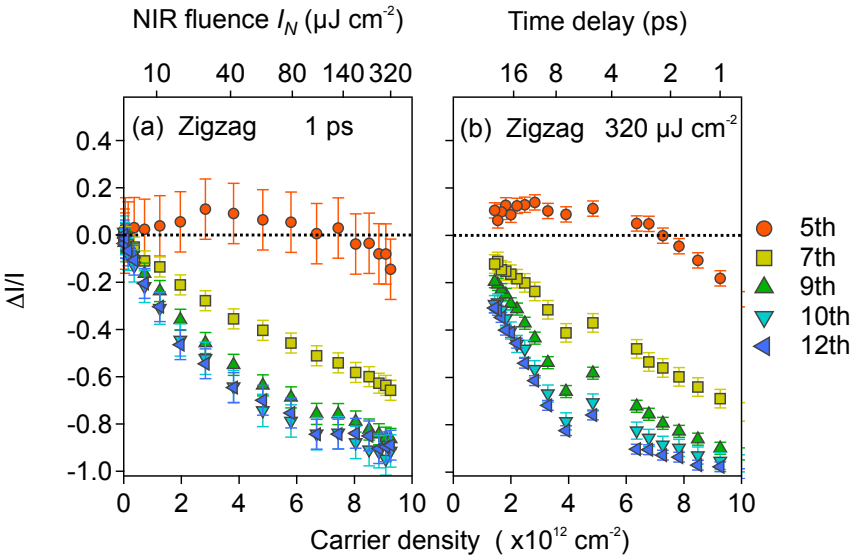

Figure 4.9: Photo-carrier density dependence of differential harmonic intensity. (a) The dependence of the near-infrared (NIR) pump fluence at a time delay of 1 ps and (b) the dependence on the time delay at pump fluence of 320 μJ cm^{-2} are converted into carrier density dependences. The carrier density was estimated from the fitting results in Fig. 4.6. The mid-infrared polarization is along the zigzag direction. The error bars represent standard deviations calculated by assuming that the deviations are independent of the time delay and NIR pump fluence.

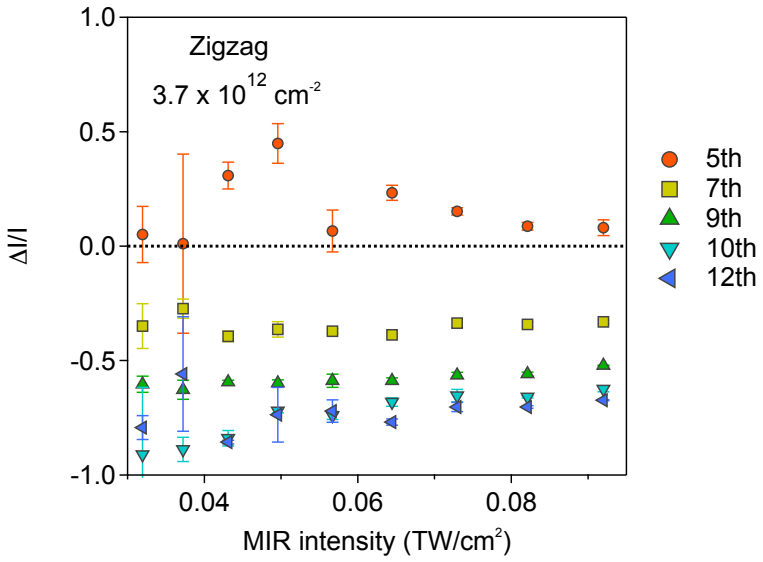

Figure 4.10: Mid-infrared (MIR) intensity dependence of differential harmonic intensity under photo-carrier doping. The polarization of the MIR pulse is along the zigzag direction. The error bars represent standard deviations of the mean value from five measurements under identical conditions.

The same experiments were also performed for a multilayer sample and we found a similar result to the monolayer shown in Appendix B.2.

4.5 Method of numerical calculation

Here, we analyze the photo-carrier doping effect on HHG by numerical simulation. Several numerical methods have been proposed to calculate HHG spectra, such as time dependent Schrödinger equation (TDSE) [69], semiconductor Bloch equation (SBE) [67, 72], and time-dependent density functional theory [73, 74]. In this work, we focus on the analysis with SBE. The TDSE is based on the single active electron approximation and in turn, neglects the effect of many body interactions in solids. On the other hand, the TDDFT can include the effect of electronic correlations. However, it requires a high calculation cost. The SBE can include two-particle correlations, e.g. excitonic effect, and phenomenologically treat other many body effects.

4.5.1 Derivation of Semiconductor Bloch equation

In this section, we drive the semiconductor Bloch equation (SBE) [163]. The Hartree-Fock approximation is used to obtain the single-electron approximation [164]. We consider the electronic state when all the bands below the valence band are fully occupied by electrons as the ground state of the system. Interacting electron Hamiltonian is generally written as

$$H = \int d^3\mathbf{r}\hat{\psi}^\dagger(\mathbf{r})H_1\hat{\psi}(\mathbf{r}) \tag{4.4}$$

$$+ \frac{1}{2}\int d^3\mathbf{r}\int d^3\mathbf{r}'\hat{\psi}^\dagger(\mathbf{r})\hat{\psi}^\dagger(\mathbf{r}')H_2\hat{\psi}(\mathbf{r}')\hat{\psi}(\mathbf{r}) \tag{4.5}$$

The field operator is written as

$$\hat{\psi}(\mathbf{r},t) = \sum_\nu \hat{a}_\nu(t)\phi_\nu(\mathbf{r}), \tag{4.6}$$

where $\phi_\nu(\mathbf{r})$ is the complete set of Bloch wave function written by

$$\phi_{n,\mathbf{k}}(\mathbf{r}) = u_{n,\mathbf{k}}(\mathbf{r})\mathrm{e}^{i\mathbf{k}\cdot\mathbf{r}}, \tag{4.7}$$

where $u_{n,\mathbf{k}}(\mathbf{r})$ is a periodic function in real space. For simplicity, we ignore the spin degrees of freedom and denote the band number n and Bloch wavenumber k collectively as ν.

$$H = \sum_\nu \langle\nu|H_1|\nu\rangle a_\nu^\dagger a_\nu + \frac{1}{2}\sum_{\nu_1,\nu_2,\nu_3,\nu_4}\langle\nu_1,\nu_2|H_2|\nu_4,\nu_3\rangle a_{\nu_1}^\dagger a_{\nu_2}^\dagger a_{\nu_3}a_{\nu_4}, \tag{4.8}$$

where H_1 is the operator that represents the electron kinetic energy and the potential from the lattice, H_2 represents the Coulomb interaction between two electrons. $a_\nu^\dagger$ and a_ν are creation and annihilation operator of electron suffixed by ν, respectively. The matrix element of H_2 is written by

$$\begin{aligned}\langle\nu_1,\nu_2|H_2|\nu_4,\nu_3\rangle &= \langle n_1,\mathbf{k}_1|_1\otimes\langle n_2,\mathbf{k}_2|_2 V(\hat{\mathbf{r}}_1-\hat{\mathbf{r}}_2)|n_4,\mathbf{k}_4\rangle_1\otimes|n_3,\mathbf{k}_3\rangle_2 \\ &= \sum_{\mathbf{q}} V_q\langle n_1,\mathbf{k}_1|\mathrm{e}^{i\mathbf{q}\cdot\hat{\mathbf{r}}}|n_4,\mathbf{k}_4\rangle\langle n_2,\mathbf{k}_2|\mathrm{e}^{-i\mathbf{q}\cdot\hat{\mathbf{r}}}|n_3,\mathbf{k}_3\rangle,\end{aligned} \tag{4.9}$$

where

$$V(\mathbf{r}) = \frac{e^2}{4\pi\varepsilon_0 r} \tag{4.10}$$

$$V(\mathbf{r}) = \sum_{\mathbf{q}} V_q \mathrm{e}^{i\mathbf{q}\cdot\mathbf{r}} = \sum_{\mathbf{G}} \sum_{\mathbf{q}\in \mathrm{BZ}} V_{\mathbf{q}+\mathbf{G}} \mathrm{e}^{i(\mathbf{q}+\mathbf{G})\cdot\mathbf{r}}, \tag{4.11}$$

$e > 0$ is the elemental charge and $\mathbf{G}$ is the reciprocal vector. To consider two-dimensional materials in this work, we evaluate the Coulomb interaction by integrating eq. (4.10) in 2D space

$$V_q = \frac{1}{L^2} \int V(\mathbf{r}) \mathrm{e}^{-i\mathbf{q}\cdot\mathbf{r}} d\mathbf{r} = \frac{e^2}{2\varepsilon_0 L^2 q}, \tag{4.12}$$

where ε_0 is the permittivity in the 2D space. The component in eq. (4.9) is calculated as follows:

$$\langle n,\mathbf{k}| \mathrm{e}^{i\mathbf{q}\cdot\hat{\mathbf{r}}} |n',\mathbf{k}'\rangle = \int u^*_{n,\mathbf{k}}(\mathbf{r}) u_{n',\mathbf{k}'}(\mathbf{r}) \mathrm{e}^{i(\mathbf{q}-\mathbf{k}+\mathbf{k}')\cdot\mathbf{r}} d\mathbf{r} \tag{4.13}$$

$$= \int_{unitcell} \sum_{\mathbf{R}} u^*_{n,\mathbf{k}}(\mathbf{r}) u_{n',\mathbf{k}'}(\mathbf{r}) \mathrm{e}^{i(\mathbf{q}-\mathbf{k}+\mathbf{k}')\cdot(\mathbf{r}+\mathbf{R})} d\mathbf{r} \tag{4.14}$$

$$= \sum_{\mathbf{G}} \delta_{\mathbf{q}+\mathbf{G},\mathbf{k}-\mathbf{k}'} \langle u_{n,\mathbf{k}} | u_{n',\mathbf{k}'} \rangle . \tag{4.15}$$

Thus, we obtain

$$H = \sum_{n,\mathbf{k}} \varepsilon_n(\mathbf{k}) a^\dagger_{n,\mathbf{k}} a_{n,\mathbf{k}} + \frac{1}{2} \sum_{n,n',m,m'} \sum_{\mathbf{k},\mathbf{k}',\mathbf{q}\in \mathrm{BZ}} V^{n,n',m,m'}_{\mathbf{k},\mathbf{k}',\mathbf{q}} a^\dagger_{n,\mathbf{k}+\mathbf{q}} a^\dagger_{m,\mathbf{k}'-\mathbf{q}} a_{m',\mathbf{k}'} a_{n',\mathbf{k}} \tag{4.16}$$

$$V^{n,n',m,m'}_{\mathbf{k},\mathbf{k}',\mathbf{q}} = \sum_{\mathbf{G}} V_{\mathbf{q}+\mathbf{G}} \langle u_{n,\mathbf{k}+\mathbf{q}} | u_{n',\mathbf{k}} \rangle \langle u_{m,\mathbf{k}'-\mathbf{q}} | u_{m',\mathbf{k}'} \rangle , \tag{4.17}$$

where $\varepsilon_{e(h)}(\mathbf{k})$ is the energy of the n-th band for single electron. In semiconductor optics, the sum over the $\mathbf{G}$ has often been neglected to describe the excitonic response near Γ point [165].

Semiconductor Bloch equation near bandgap

Here, we derive the Semiconductor Bloch equation historically used for the electrons around the Γ point near the bandgap of typical semiconductors. The periodic part of the Bloch function contains the information of the atomic wave functions. We neglect its wavenumber dependence around the bandgap:

$$\langle u_{n,\mathbf{k}+\mathbf{q}} | u_{n',\mathbf{k}} \rangle \approx \langle u_{n,\mathbf{k}} | u_{n',\mathbf{k}} \rangle = \delta_{n,n'}. \tag{4.18}$$

Accordingly, we obtain a simplier form of eq. (4.16).

$$H = \sum_{n,\mathbf{k}} \varepsilon_n(\mathbf{k}) a^\dagger_{n,\mathbf{k}} a_{n,\mathbf{k}} + \frac{1}{2} \sum_{n,n'} \sum_{\mathbf{G}} \sum_{\mathbf{k},\mathbf{k}',\mathbf{q}\in \mathrm{BZ}} V_{\mathbf{q}+\mathbf{G}} a^\dagger_{n,\mathbf{k}+\mathbf{q}} a^\dagger_{m,\mathbf{k}'-\mathbf{q}} a_{m,\mathbf{k}'} a_{n,\mathbf{k}} \tag{4.19}$$

Below, we focus on a two-band system and use the electron-hole picture. We define the creation operators of the electron in conduction band and hole in valence band by

$$\alpha_{\mathbf{k}}^{\dagger} = a_{c,\mathbf{k}}^{\dagger} \tag{4.20}$$

$$\beta_{-\mathbf{k}}^{\dagger} = a_{v,\mathbf{k}} \tag{4.21}$$

, respectively. By using the anti-commutation relation,

$$[a_{\mu}, a_{\nu}^{\dagger}]_{+} = \delta_{\mu,\nu} \tag{4.22}$$

$$[a_{\mu}, a_{\nu}]_{+} = 0 \tag{4.23}$$

$$[a_{\mu}^{\dagger}, a_{\nu}^{\dagger}]_{+} = 0 \tag{4.24}$$

the Hamiltonian eq. (4.16) becomes the following form:

$$\begin{aligned} H_0 &= \sum_{\mathbf{k}} \left(\varepsilon_e(\mathbf{k}) \alpha_{\mathbf{k}}^{\dagger} \alpha_{\mathbf{k}} + \varepsilon_h(\mathbf{k}) \beta_{-\mathbf{k}}^{\dagger} \beta_{-\mathbf{k}} \right) + \frac{1}{2} \sum_{\mathbf{G}} \sum_{\mathbf{k},\mathbf{k}',\mathbf{q} \in \mathrm{BZ}} V_{\mathbf{q}+\mathbf{G}} \Big[\alpha_{\mathbf{k}+\mathbf{q}}^{\dagger} \alpha_{\mathbf{k}'-\mathbf{q}}^{\dagger} \alpha_{\mathbf{k}'} \alpha_{\mathbf{k}} \\ &\quad + \beta_{\mathbf{k}+\mathbf{q}}^{\dagger} \beta_{\mathbf{k}'-\mathbf{q}}^{\dagger} \beta_{\mathbf{k}'} \beta_{\mathbf{k}} - 2 \alpha_{\mathbf{k}+\mathbf{q}}^{\dagger} \beta_{\mathbf{k}'-\mathbf{q}}^{\dagger} \beta_{\mathbf{k}'} \alpha_{\mathbf{k}} \Big]. \end{aligned} \tag{4.25}$$

where $\varepsilon_{e(h)}(\mathbf{k})$ is the energy of electron (hole) band.

Next, we consider the interaction Hamiltonian between single electron and classical electric field. By using the length gauge assuming the long wavelength approximation and Houston basis [33, 166], we obtain

$$\begin{aligned} H_I(t) &= \int \mathbf{dr} \hat{\psi}^{\dagger}(\mathbf{r}) e \mathbf{r} \cdot \mathbf{E}(t) \hat{\psi}(\mathbf{r}) && (4.26) \\ &= -\mathbf{E}(t) \cdot \sum_{\mathbf{k}} \Big[\alpha_{\mathbf{k}}^{\dagger} \mathbf{X}_{cc}(\mathbf{k}) \alpha_{\mathbf{k}} + \beta_{-\mathbf{k}} \mathbf{X}_{vv}(\mathbf{k}) \beta_{-\mathbf{k}}^{\dagger} \\ &\quad + \alpha_{\mathbf{k}}^{\dagger} \beta_{-\mathbf{k}}^{\dagger} \mathbf{X}_{cv}(\mathbf{k}) + \beta_{-\mathbf{k}} \alpha_{\mathbf{k}} \mathbf{X}_{vc}(\mathbf{k}) \Big] && (4.27) \\ \mathbf{X}_{nm}(\mathbf{k}) &= -e \langle n, \mathbf{k} | \hat{\mathbf{r}} | m, \mathbf{k} \rangle && (4.28) \\ &= -ie \delta_{nm} \frac{\partial}{\partial \mathbf{k}} + \mathbf{d}_{nm}(\mathbf{k}). && (4.29) \end{aligned}$$

Here, the eq. (4.29) is calculated by the following procedure.

$$\begin{aligned} & \langle n, \mathbf{k} | \hat{\mathbf{r}} | m, \mathbf{k}' \rangle \\ &= \int \mathbf{d}^3\mathbf{r} \phi_{n,\mathbf{k}}^*(\mathbf{r}) \mathbf{r} \phi_{m,\mathbf{k}'}(\mathbf{r}) \\ &= \int \mathbf{d}^3\mathbf{r} \mathrm{e}^{-i\mathbf{k}\cdot\mathbf{r}} u_{n,\mathbf{k}}^*(\mathbf{r}) u_{m,\mathbf{k}'}(\mathbf{r}) \left(-i \frac{\partial}{\partial \mathbf{k}'} \mathrm{e}^{i\mathbf{k}'\cdot\mathbf{r}} \right) \\ &= -i \frac{\partial}{\partial \mathbf{k}} \int \mathbf{d}^3\mathbf{r} \phi_{n,\mathbf{k}}^*(\mathbf{r}) \phi_{m,\mathbf{k}'}(\mathbf{r}) + i \int \mathbf{d}^3\mathbf{r} \mathrm{e}^{-i(\mathbf{k}-\mathbf{k}')\cdot\mathbf{r}} u_{n,\mathbf{k}}^*(\mathbf{r}) \frac{\partial}{\partial \mathbf{k}'} u_{m,\mathbf{k}'}(\mathbf{r}) \\ &= i \delta_{nm} \delta(\mathbf{k}-\mathbf{k}') \frac{\partial}{\partial \mathbf{k}} + i \sum_{\mathbf{R}} \mathrm{e}^{-i(\mathbf{k}-\mathbf{k}')\cdot\mathbf{R}} \int_{unitcell} \mathbf{d}^3\mathbf{r} \mathrm{e}^{-i(\mathbf{k}-\mathbf{k}')\cdot\mathbf{r}} u_{n,\mathbf{k}}^*(\mathbf{r}) \frac{\partial}{\partial \mathbf{k}'} u_{m,\mathbf{k}'}(\mathbf{r}) \\ &= \delta(\mathbf{k}-\mathbf{k}') \left(i \delta_{nm} \frac{\partial}{\partial \mathbf{k}} + i \int_{unitcell} \mathbf{d}^3\mathbf{r} u_{n,\mathbf{k}}^*(\mathbf{r}) \frac{\partial}{\partial \mathbf{k}} u_{m,\mathbf{k}}(\mathbf{r}) \right) \\ &= \delta(\mathbf{k}-\mathbf{k}') \left(i \delta_{nm} \frac{\partial}{\partial \mathbf{k}} - \mathbf{d}_{nm}(\mathbf{k})/e \right), \end{aligned} \tag{4.30}$$

where the **R** is the primitive vector in a crystalline solid, and the delta function is defined in the first Brillouin zone. The transformation between the fourth and fifth lines is obtained by integrating by parts and considering the surface term to be zero due to the periodicity in k-space. The diagonal and off-diagonal terms of

$$\mathbf{d}_{nm}(\mathbf{k}) = -ie\int_{unitcell}\mathbf{d}^3\mathbf{r}u^*_{n,\mathbf{k}}(\mathbf{r})\frac{\partial}{\partial\mathbf{k}}u_{m,\mathbf{k}}(\mathbf{r}). \tag{4.31}$$

are the Berry connection and interband dipole moment, respectively.

Below we neglect the dependence of the dipole moment in k-space. We also neglect the Berry connection, which vanishes around the Γ due to the symmetry, i.e., $\mathbf{d}_{nn}(\mathbf{k}) = -\mathbf{d}^*_{nn}(-\mathbf{k})$. Around the bandgap at K point in TMDs, the Berry curvature may have a non-negligible effect. These assumptions break the gauge invariance of SBE [167]. However, a recent calculation considering monolayer WSe_2 showed that the Berry connection is negligible for HSG.

We now want to derive the coupled equation of motion for the following elements.

$$P_{\mathbf{k}}(t) = \langle\beta_{-\mathbf{k}}\alpha_{\mathbf{k}}(t)\rangle \tag{4.32}$$

$$n_{e,\mathbf{k}}(t) = \langle\alpha^\dagger_{\mathbf{k}}\alpha_{\mathbf{k}}(t)\rangle \tag{4.33}$$

$$n_{h,\mathbf{k}}(t) = \langle\beta^\dagger_{-\mathbf{k}}\beta_{-\mathbf{k}}(t)\rangle \tag{4.34}$$

The time evolution is calculated by the Heisenberg equation:

$$i\hbar\frac{\partial\langle\mathscr{O}\rangle}{\partial t} = \langle[\mathscr{O},H]\rangle \tag{4.35}$$

where $\mathscr{O}$ is an operator.

The time evolution of above elements are written as

$$\begin{aligned}
\frac{\partial}{\partial t}(\beta_{-\mathbf{k}}\alpha_{\mathbf{k}}) &= \frac{i}{\hbar}[H_0+H_I(t),\beta_{-\mathbf{k}}\alpha_{\mathbf{k}}] \\
&= -\frac{i}{\hbar}(\varepsilon_e(\mathbf{k})+\varepsilon_h(\mathbf{k})+ie\mathbf{E}(t)\cdot\frac{\partial}{\partial\mathbf{k}})(\beta_{-\mathbf{k}}\alpha_{\mathbf{k}}) \\
&- \frac{i}{\hbar}\mathbf{d}_{cv}\cdot\mathbf{E}(t)\left(\alpha^\dagger_{\mathbf{k}}\alpha_{\mathbf{k}}+\beta^\dagger_{-\mathbf{k}}\beta_{-\mathbf{k}}-1\right) \\
&- \frac{i}{\hbar}\sum_{\mathbf{k}',\mathbf{q}\in\mathrm{BZ}}\tilde{V}_{\mathbf{q}}\left(\alpha^\dagger_{\mathbf{k}'+\mathbf{q}}\beta_{-\mathbf{k}+\mathbf{q}}\alpha_{\mathbf{k}'}\alpha_{\mathbf{k}}-\beta^\dagger_{\mathbf{k}'+\mathbf{q}}\beta_{-\mathbf{k}+\mathbf{q}}\beta_{\mathbf{k}'}\alpha_{\mathbf{k}}\right. \\
&+ \left.\beta_{-\mathbf{k}}\alpha^\dagger_{\mathbf{k}'-\mathbf{q}}\alpha_{\mathbf{k}'}\alpha_{\mathbf{k}-\mathbf{q}}-\beta_{-\mathbf{k}}\beta^\dagger_{\mathbf{k}'-\mathbf{q}}\beta_{\mathbf{k}'}\alpha_{\mathbf{k}-\mathbf{q}}\right)
\end{aligned} \tag{4.36}$$

$$\begin{aligned}
\frac{\partial}{\partial t}\left(\alpha^\dagger_{\mathbf{k}}\alpha_{\mathbf{k}}\right) &= \frac{i}{\hbar}\left[H_0+H_I(t),\alpha^\dagger_{\mathbf{k}}\alpha_{\mathbf{k}}\right] \\
&= -2\mathrm{Im}[\frac{\mathbf{d}_{cv}\cdot\mathbf{E}(t)}{\hbar}\alpha^\dagger_{\mathbf{k}}\beta^\dagger_{-\mathbf{k}}]+\frac{e\mathbf{E}(t)}{\hbar}\cdot\frac{\partial}{\partial\mathbf{k}}\alpha^\dagger_{\mathbf{k}}\alpha_{\mathbf{k}} \\
&+ \frac{i}{\hbar}\sum_{\mathbf{k}',\mathbf{q}\in\mathrm{BZ}}\tilde{V}_{\mathbf{q}}\left(\alpha^\dagger_{\mathbf{k}}\alpha^\dagger_{\mathbf{k}'-\mathbf{q}}\alpha_{\mathbf{k}-\mathbf{q}}\alpha_{\mathbf{k}'}-\alpha^\dagger_{\mathbf{k}+\mathbf{q}}\alpha^\dagger_{\mathbf{k}'-\mathbf{q}}\alpha_{\mathbf{k}}\alpha_{\mathbf{k}'}\right. \\
&+ \left.\alpha^\dagger_{\mathbf{k}}\alpha_{\mathbf{k}-\mathbf{q}}\beta^\dagger_{\mathbf{k}'-\mathbf{q}}\beta_{\mathbf{k}'}-\alpha^\dagger_{\mathbf{k}+\mathbf{q}}\alpha_{\mathbf{k}}\beta^\dagger_{\mathbf{k}'-\mathbf{q}}\beta_{\mathbf{k}'}\right)
\end{aligned} \tag{4.37}$$

$$\begin{aligned}
\frac{\partial}{\partial t}\left(\beta^{\dagger}_{-\mathbf{k}}\beta_{-\mathbf{k}}\right) &= \frac{i}{\hbar}\left[H_0+H_I(t),\beta^{\dagger}_{-\mathbf{k}}\beta_{-\mathbf{k}}\right] \\
&= -2\mathrm{Im}[\frac{\mathbf{d}_{cv}\cdot\mathbf{E}(t)}{\hbar}\alpha^{\dagger}_{\mathbf{k}}\beta^{\dagger}_{-\mathbf{k}}]+\frac{e\mathbf{E}(t)}{\hbar}\cdot\frac{\partial}{\partial\mathbf{k}}\beta^{\dagger}_{-\mathbf{k}}\beta_{-\mathbf{k}} \\
&+ \frac{i}{\hbar}\sum_{\mathbf{k}',\mathbf{q}\in\mathrm{BZ}}\tilde{V}_{\mathbf{q}}\left(\beta^{\dagger}_{-\mathbf{k}}\beta^{\dagger}_{\mathbf{k}'-\mathbf{q}}\beta_{-\mathbf{k}-\mathbf{q}}\beta_{\mathbf{k}'}-\beta^{\dagger}_{-\mathbf{k}+\mathbf{q}}\beta^{\dagger}_{\mathbf{k}'-\mathbf{q}}\beta_{-\mathbf{k}}\beta_{\mathbf{k}'}\right. \\
&+ \left.\alpha^{\dagger}_{\mathbf{k}'+\mathbf{q}}\alpha_{\mathbf{k}'}\beta^{\dagger}_{-\mathbf{k}}\beta_{-\mathbf{k}+\mathbf{q}}-\alpha^{\dagger}_{\mathbf{k}'+\mathbf{q}}\alpha_{\mathbf{k}'}\beta^{\dagger}_{-\mathbf{k}-\mathbf{q}}\beta_{-\mathbf{k}}\right), \qquad (4.38)
\end{aligned}$$

where $\tilde{V}_{\mathbf{q}}=\sum_{\mathbf{G}}V_{\mathbf{q}+\mathbf{G}}$ is used. The right-hand sides of the above equations contain the products of four creation and annihilation operators. The time evolutions of the expectation values of these products also follow higher correlation terms according to the Heisenberg equation. This problem is dealt with as a hierarchy problem using a cluster expansion approach [163, 165]. By neglecting the higher order term of the hierarchy, we obtain

$$\begin{aligned}
\frac{\partial}{\partial t}P_{\mathbf{k}} &= -\frac{i}{\hbar}(e_e(\mathbf{k})+e_h(\mathbf{k})+ie\mathbf{E}(t)\cdot\frac{\partial}{\partial\mathbf{k}})P_{\mathbf{k}}-i\omega_{R,\mathbf{k}}\left(n_{e,\mathbf{k}}+n_{h,\mathbf{k}}-1\right) && (4.39)\\
\frac{\partial}{\partial t}n_{e,\mathbf{k}} &= -2\mathrm{Im}[\omega_{R,\mathbf{k}}P^{*}_{\mathbf{k}}]+\frac{e\mathbf{E}(t)}{\hbar}\cdot\frac{\partial}{\partial\mathbf{k}}n_{e,\mathbf{k}} && (4.40)\\
\frac{\partial}{\partial t}n_{h,\mathbf{k}} &= -2\mathrm{Im}[\omega_{R,\mathbf{k}}P^{*}_{\mathbf{k}}]+\frac{e\mathbf{E}(t)}{\hbar}\cdot\frac{\partial}{\partial\mathbf{k}}n_{h,\mathbf{k}} && (4.41)\\
e_i(\mathbf{k}) &= \varepsilon_i(\mathbf{k})-\sum_{\mathbf{q}\neq\mathbf{k}}\tilde{V}_{\mathbf{k}-\mathbf{q}}n_{i,\mathbf{q}} && (4.42)\\
\omega_{R,\mathbf{k}} &= \frac{1}{\hbar}\left[\mathbf{d}_{cv}\cdot\mathbf{E}(t)+\sum_{\mathbf{q}\neq\mathbf{k}}\tilde{V}_{\mathbf{k}-\mathbf{q}}P_{\mathbf{q}}\right] && (4.43)
\end{aligned}$$

where $e_i(\mathbf{k})$ is the single particle energy and $\hbar\omega_{R,\mathbf{k}}$ is the generalized Rabi frequency. The equation (4.39-4.43) is called SBE. Note that the representation of SBE derived here are different from those considering the Berry connection [167].

The intra- and inter-band current is calculated by the expectation values of current operator. We define the current operator from the velocity operator using the Heisenberg equation (4.35) as

$$\hat{\mathbf{J}}(\mathbf{r}) = \frac{ie}{\hbar}[\hat{\mathbf{r}},H] \qquad (4.44)$$

using eq. (4.19). By taking only single-particle Hamiltonian into account, we obtain the expectation values of total current as follows

$$\langle\hat{\mathbf{J}}\rangle = \frac{ie}{\hbar}\sum_{\mathbf{k},\mathbf{k}'}\sum_{i,j}\int d^3\mathbf{r}\,\langle n,\mathbf{k}|\,[\hat{\mathbf{r}},H_1]\,|m,\mathbf{k}'\rangle\,\langle a^{\dagger}_{n,\mathbf{k}}a_{m,\mathbf{k}'}\rangle\,. \qquad (4.45)$$

When we focus on the two-band system, we can separate the current into two terms: intraband (diagonal term) and interband (off-diagonal) current

$$\begin{aligned}
\mathbf{J}(t) &= \mathbf{J}_{ra}(t)+\mathbf{J}_{er}(t) && (4.46)\\
\mathbf{J}_{ra}(t) &= \frac{e}{\hbar}\sum_{\mathbf{k},i=e,h}\frac{\partial}{\partial\mathbf{k}}\varepsilon_i(\mathbf{k})n_{i,\mathbf{k}} && (4.47)\\
\mathbf{J}_{er}(t) &= \frac{2}{\hbar}\sum_{\mathbf{k}}\varepsilon_g(\mathbf{k})\mathrm{Im}\left[\mathbf{d}^{*}_{cv}P_{\mathbf{k}}\right]. && (4.48)
\end{aligned}$$

with $\varepsilon_g(\mathbf{k})=\varepsilon_c(\mathbf{k})-\varepsilon_v(\mathbf{k})$

Transformation of SBE into ordinary differential equation

By transforming the frame of eq. (4.43), we can rewrite the SBE as ordinary differential equation [67, 167]. We replace the parameter $(t, \mathbf{k})$ by $(t, \mathbf{K})$ with $\mathbf{K}(t) = \mathbf{k} + \frac{e}{\hbar}\mathbf{A}(t)$. The transformed equations are given as follows:

$$\frac{d}{dt}\tilde{P}_{\mathbf{K}} = -\frac{i}{\hbar}(e_e(\mathbf{K} - \frac{e}{\hbar}\mathbf{A}(t)) + e_h(\mathbf{K} - \frac{e}{\hbar}\mathbf{A}(t)))\tilde{P}_{\mathbf{K}} - i\omega_{R,\mathbf{k}}\left(\tilde{n}_{e,\mathbf{K}} + \tilde{n}_{h,\mathbf{K}} - 1\right) \tag{4.49}$$

$$\frac{d}{dt}\tilde{n}_{e,\mathbf{K}} = -2\mathrm{Im}[\omega_{R,\mathbf{K}-\frac{e}{\hbar}\mathbf{A}(t)}\tilde{P}^*_{\mathbf{K}}] \tag{4.50}$$

$$\frac{d}{dt}\tilde{n}_{h,\mathbf{K}} = -2\mathrm{Im}[\omega_{R,\mathbf{K}-\frac{e}{\hbar}\mathbf{A}(t)}\tilde{P}^*_{\mathbf{K}}] \tag{4.51}$$

with $P_{\mathbf{k}} = \tilde{P}_{\mathbf{K}}$ and $n_{\mathbf{k}} = \tilde{n}_{e,\mathbf{K}}$. In this frame, the parameter $\mathbf{K}$ follows the motion of electron wave packet in k-space written by the acceleration theorem $\frac{\partial \hbar \mathbf{K}}{\partial t} = -e\mathbf{F}(t)$. The corresponding intraband and interband current is written by

$$\mathbf{J}(t) = \mathbf{J}_{ra}(t) + \mathbf{J}_{er}(t) \tag{4.52}$$

$$\mathbf{J}_{ra}(t) = \frac{e}{\hbar}\sum_{\mathbf{K},i=e,h}\frac{\partial}{\partial \mathbf{K}}\varepsilon_i(\mathbf{K} - \frac{e}{\hbar}\mathbf{A}(t))\tilde{n}_{i,\mathbf{K}} \tag{4.53}$$

$$\mathbf{J}_{er}(t) = \frac{2}{\hbar}\sum_{\mathbf{K}}\varepsilon_g(\mathbf{K} - \frac{e}{\hbar}\mathbf{A}(t))\mathrm{Im}\left[\mathbf{d}^*_{cv}\tilde{P}_{\mathbf{K}}\right]. \tag{4.54}$$

Exciton wave function

The homogeneous part of eq. (4.39) leads to the linear optical response of exciton [163, 165].

$$\frac{d}{dt}P_{\mathbf{k}}(t) = -\frac{i}{\hbar}(\varepsilon_e(\mathbf{k}) + \varepsilon_h(\mathbf{k}))P_{\mathbf{k}}(t) + \frac{i}{\hbar}\left[\mathbf{d}_{cv}\cdot\mathbf{E}(t) + \sum_{\mathbf{q}\neq\mathbf{k}}\tilde{V}_{\mathbf{k}-\mathbf{q}}P_{\mathbf{q}}\right], \tag{4.55}$$

where $(n_{i,\mathbf{k}} \sim 0)$ is assumed. By Fourier transforming the eq. (4.55), we obtain

$$(\varepsilon_e(\mathbf{k}) + \varepsilon_h(\mathbf{k}) - \hbar\omega)P_{\mathbf{k}}(\omega) = \mathbf{d}_{cv}\cdot\mathbf{E}(\omega) + \sum_{\mathbf{q}\neq\mathbf{k}}\tilde{V}_{\mathbf{k}-\mathbf{q}}P_{\mathbf{q}}(\omega). \tag{4.56}$$

When $\mathbf{E}(\omega) = 0$, eq. (4.56) leads to the generalized Wannier equation represented in k-space [163, 165]. The exciton energy and wave function in k-space are the eigenvalue and the eigenfunction of the following equation, respectively:

$$(\varepsilon_e(\mathbf{k}) + \varepsilon_h(\mathbf{k}) - \varepsilon_\nu)\psi_\nu(\mathbf{k}) = \sum_{\mathbf{q}\neq\mathbf{k}}\tilde{V}_{\mathbf{k}-\mathbf{q}}\psi_\nu(\mathbf{q}). \tag{4.57}$$

If we reduce the energy dispersion to a parabolic structure and transform them into real space representation, we can obtain the Wannier equation used for the calculation of Wannier-Mott exciton [165].

Linear absorption of exciton

To understand the linear optical response of the exciton, we expand the $P_{\mathbf{k}}$ with the set of $\psi_\nu(\mathbf{k})$

$$P_{\mathbf{k}}(\omega) = \sum_\nu b_\nu(\omega)\psi_\nu(\mathbf{k}). \tag{4.58}$$

By substituting this into eq. (4.56), we obtain

$$\sum_\nu (\varepsilon_\nu - \hbar\omega) b_\nu(\omega)\psi_\nu(\mathbf{k}) \quad = \quad \mathbf{d}_{cv}(\mathbf{k})\cdot\mathbf{E}(\omega). \tag{4.59}$$

Multiplying by $\psi^*_\mu(\mathbf{k})$ from the left and summing over $\mathbf{k}$, we get

$$\sum_\nu (\varepsilon_\nu - \hbar\omega) b_\nu(\omega) \sum_{\mathbf{k}} \psi^*_\mu(\mathbf{k})\psi_\nu(\mathbf{k}) \quad = \quad \sum_{\mathbf{k}} \mathbf{d}_{cv}\cdot\mathbf{E}(\omega)\psi^*_\mu(\mathbf{k}) \tag{4.60}$$

$$\begin{aligned} b_\mu(\omega) &= \frac{\mathbf{d}_{cv}\cdot\mathbf{E}(\omega)}{\varepsilon_\mu - \hbar\omega}\sum_{\mathbf{k}}\psi^*_\mu(\mathbf{k}) \\ &= \frac{\mathbf{d}_{cv}\cdot\mathbf{E}(\omega)\psi^*_\mu(\mathbf{r}=0)}{\varepsilon_\mu - \hbar\omega} \end{aligned} \tag{4.61}$$

Thus, $P_{\mathbf{k}}(\omega)$ is given by

$$P_{\mathbf{k}}(\omega) \quad = \quad \sum_\nu \frac{\mathbf{d}_{cv}\cdot\mathbf{E}(\omega)\psi^*_\nu(\mathbf{r}=0)}{\varepsilon_\nu - \hbar\omega}\psi_\nu(\mathbf{k}) \tag{4.62}$$

Considering the phenomenological damping γ, one finds the polarization given as follows:

$$\begin{aligned} P(\omega) &= \sum_{\mathbf{k}} (d^*_{cv}P_{\mathbf{k}}(-\omega) + d_{cv}P^*_{\mathbf{k}}(\omega)) \\ &= -L^D\sum_\nu |d_{cv}|^2 E(\omega)|\psi_\nu(\mathbf{r}=0)|^2\left[\frac{1}{\hbar\omega - \varepsilon_\nu + i\gamma} - \frac{1}{\hbar\omega + \varepsilon_\nu + i\gamma}\right], \end{aligned} \tag{4.63}$$

where D is the dimension of the system. By considering only the resonant part of eq. (4.63), absorption spectrum can be calculated as

$$\alpha(\omega) \propto \mathrm{Im}\left[\frac{P(\omega)}{E(\omega)}\right] = -L^D\sum_\nu |d_{cv}|^2|\psi_\nu(\mathbf{r}=0)|^2\mathrm{Im}\left[\frac{1}{\hbar\omega - \varepsilon_\nu + i\gamma}\right] \tag{4.64}$$

Excitonic optical stark shift

We estimated the magnitude of dipole moment by evaluating the excitonic optical stark effect. The excitonic optical stark effect is the phenomenon where the exciton energy is shifted by a perturbation of an AC light field. Here, we derive the relation between the dipole moment in single electron-hole picture and the dipole of the exciton in two-level system.

We consider a situation where a non-resonant light pulse is irradiated to an exciton and its envelope is sufficiently smooth with respect to the carrier frequency. The exciton

resonance energy in the light pulse can be obtained by calculating the linear response to the probe light (test light) using the SBE about the microscopic polarization with $\mathbf{E}(\omega) = 0$ (eq. (4.55)). We write the electric field of the pump light as $\mathbf{E}(t) = \mathbf{E}_p \exp(-i\omega t)$. The energy shift of the exciton is written by

$$\begin{aligned} \Delta H_{\lambda\lambda'} &= \Pi_{\lambda\lambda'} + \Delta_{\lambda\lambda'} && (4.65)\\ \Pi_{\lambda\lambda'} &= 2\mathbf{E}_p \cdot \sum_k \psi^*_\lambda(\mathbf{k}) \mathbf{d}_{cv} p^*_k \psi_{\lambda'}(\mathbf{k}) && (4.66)\\ \Delta_{\lambda\lambda'} &= 2\sum_{kk'} V_{k-k'} \psi^*_\lambda(\mathbf{k})(p^*_k - p^*_{k'})(p_k \psi_{\lambda'}(\mathbf{k}') + p_{k'} \psi_{\lambda'}(\mathbf{k})) && (4.67) \end{aligned}$$

where The p_k is defined by $P_k = p_k \exp(-i\omega t)$ for the polarization P_k induced by the pump light [165]. $\Pi_{\lambda\lambda'}$ is the exciton photon interaction and $\Delta_{\lambda\lambda'}$ is the exciton exciton interaction.

The exciton polarization induced by the pump field is obtained from eq. (4.62),

$$p_k(\omega_p) = b^*_\mu(\omega) = \mathbf{d}_{cv} \cdot \mathbf{E}_{cv} \sum_\lambda \frac{\psi^*_\lambda(\mathbf{k}) \psi_\lambda(\mathbf{r}=0)}{\hbar(\omega_\lambda - \omega_p - i\delta)} \tag{4.68}$$

Under conditions where the frequency of the pump light is close enough to the 1s exciton resonance, the 1s term becomes dominant. Thus,

$$p_k(\omega_p) \approx \mathbf{d}_{cv} \cdot \mathbf{E}_{cv} \frac{\psi^*_{1s}(\mathbf{k}) \psi_{1s}(\mathbf{r}=0)}{\hbar(\omega_\lambda - \omega_p - i\delta)} \tag{4.69}$$

Therefore, the exciton energy shift is given by

$$\begin{aligned} \Pi_{1s1s} &= \psi_{1s}(\mathbf{r}=0) \sum_k \psi_{1s}(\mathbf{k}) |\psi_{1s}(\mathbf{k})|^2 \frac{2|\mathbf{d}_{cv} \cdot \mathbf{E}_{cv}|^2}{\hbar(\omega_{1s} - \omega_p)} && (4.70)\\ \Delta_{1s1s} &= |\psi_{1s}(\mathbf{r}=0)|^2 \\ &\times \sum_{kk'} \frac{V_{k-k'} \psi^*_{1s}(\mathbf{k})(\psi^*_{1s}(\mathbf{k}) - \psi^*_{1s}(\mathbf{k}'))(2\psi_{1s}(\mathbf{k})\psi_{1s}(\mathbf{k}'))}{\hbar(\omega_{1s} - \omega_p)} \frac{2|\mathbf{d}_{cv} \cdot \mathbf{E}_{cv}|^2}{\hbar(\omega_{1s} - \omega_p)}. && (4.71) \end{aligned}$$

The equation (4.70) is equal to the usual two-level stark shift $2|\mathbf{d}_{cv} \cdot \mathbf{E}_{cv}|^2/\hbar(\omega_{1s} - \omega_p)$ times an enhancement factor. The enhancement factor can be calculated analytically from the wave functions of the excitons in 2D and 3D.

$$\rho_{1S} = \psi_{1s}(\mathbf{r}=0) \sum_k \psi_{1s}(\mathbf{k}) |\psi_{1s}(\mathbf{k})|^2 = \begin{pmatrix} 16/7 & (2D) \\ 7/2 & (3D). \end{pmatrix} \tag{4.72}$$

Equation (4.71) is a term that has a different dependence on the pump optical wavelength of the shift and is particularly important near exciton resonance. In the experiment reported by Ref. [168], the stark shift is proportional to the inverse of the detuning. Thus, this term can be neglected in Ref. [168].

4.5.2 Model for numerical calculation

To better understand the effect of photo-carrier doping, we theoretically calculated harmonic spectra by using the linearized semiconductor Bloch equation (SBE) [165]. This

equation is based on the single-particle picture within the Hartree-Fock approximation, and the Coulomb interaction is introduced between the individual electrons and holes as described above. To solve the SBE, we used the band structure of gapped graphene [169]. This model describes the band structure near the band edge of monolayer TMDs at the K and K′ points [117].

$$\varepsilon_g(\mathbf{k}) = \sqrt{\Delta^2 + 4t_r^2 |f(\mathbf{k})|^2} \tag{4.73}$$

$$f(\mathbf{k}) = \sqrt{1 + 4\cos\frac{\sqrt{3}k_x a}{2}\cos\frac{k_x a}{2} + 4\cos^2\frac{k_x a}{2}} \tag{4.74}$$

Here $\Delta = 1.89$ eV is the band gap and $a = 3.28$Å is the lattice constant of monolayer WSe_2 taken from experimental results [170, 171]. t_r is determined so that the effective mass matches the value estimated from a first principles calculation [115]. $\varepsilon_g(\mathbf{k})$ is defined as the energy difference between the conduction and valence bands. The band structure is shown in Fig. 4.11(a). In our calculation, the dipole moment between the conduction and valence band $\mathbf{d}_{cv}(\mathbf{k})$ is assumed to be constant in k-space for simplicity. The Berry curvature is also neglected for simplicity. The Coulomb interaction matrix $V_{\mathbf{K}}$, which is in general dependent on the wavenumber of single electrons [172], is assumed to be only dependent on the relative wavevector of the electrons. Under these conditions, the system recovers inversion symmetry, which results in the disappearance of the even-order harmonics in the simulation. This is not an issue in our simulation as there is little difference between the odd and even order harmonics. We use the following SBE considering phenomenological scattering processes.

$$\begin{aligned}\frac{d}{dt}P_{\mathbf{K}} = &-\frac{i}{\hbar}\left[\varepsilon_g\left(\mathbf{K} - \frac{e}{\hbar}\mathbf{A}(t)\right) - i\gamma - i\gamma_e\sum_{\mathbf{q}} n_{\mathbf{q}}\right]P_{\mathbf{K}} \\ &-\frac{i}{\hbar}(2n_{\mathbf{K}} - 1)\,\mathbf{d}_{cv}\cdot\mathbf{E}(t) + \frac{i}{\hbar}\sum_{\mathbf{q}\neq\mathbf{K}}\tilde{V}_{\mathbf{K}-\mathbf{q}}P_{\mathbf{q}}\end{aligned} \tag{4.75}$$

$$\frac{d}{dt}n_{\mathbf{K}} = -\frac{2}{\hbar}\mathrm{Im}\left[\mathbf{d}_{cv}\cdot\mathbf{E}(t)\,P_{\mathbf{K}^*}\right] - \frac{1}{\hbar}\gamma_m\left[n_{\mathbf{K}} - n_{\mathbf{K}-\frac{e}{\hbar}\mathbf{A}(t),eq}\right] \tag{4.76}$$

Here, a symmetric population in the conduction and valence bands $n_{\mathbf{K}} = n_{\mathbf{c},\mathbf{K}} = 1 - n_{\mathbf{v},\mathbf{K}}$ is assumed. $\mathbf{E}(t)$ is the electric field of MIR driving field with a pulse width of 60 fs and peak field of 8.3 MV cm^{-1} corresponding to the intensity in our experiment, 0.092 TW cm^{-2}. The excursion scale of the electron-hole pairs in k-space is about a quarter of the distance between the K and K′ points at this electric field. The polarization is only in the zigzag direction in Fig. 4.11(b), because our experiment showed no clear difference between the zigzag and armchair polarizations. γ is the phenomenological dephasing rate of the interband polarization without excited carriers. The spontaneous recombination and Auger recombination process of the electron-hole pairs are assumed to be slow enough to be neglected in the HHG process. γ_e is the rate of EID, which is assumed to increase linearly with the total population [155–158]. The total dephasing rate is defined by $\Gamma = \gamma + \gamma_e\sum_{\mathbf{q}} n_{\mathbf{q}}$. The nonlinear terms of the interband coherence and population in SBE are neglected for simplicity [165]. This equation does not include the effect screening of the Coulomb interaction between electrons at high density of carriers, which is responsible for the bandgap renormalization observed in Ref. [125].

The photo-carriers are included in our simulation as initial carriers before the MIR irradiation. In our experiment, the NIR pulses were resonant with the A-exciton peak. Thus, the photo-carrier distribution is broadened in k-space according to the exciton wave function in k-space [112]. The exciton wave function is calculated by diagonalizing the following eigenvalue problem:

$$\left(\varepsilon_g(\mathbf{k}) - \varepsilon_\nu\right)\psi_\nu(\mathbf{k}) = \sum_{\mathbf{q}\neq\mathbf{k}} \tilde{V}_{\mathbf{k}-\mathbf{q}}\,\psi_\nu(\mathbf{q}), \tag{4.77}$$

where, $\psi_\nu(\mathbf{k})$ is the exciton wave function in k-space in the single-particle picture and ε_ν is the corresponding exciton energy [112, 165]. This wave function describes how the excitonic state is written by a linear superposition on the basis of Bloch wave function [112]. The diagonalization of eq. (4.77) is calculated using a 75×75 k-mech in the first Brillouin zone shown by a black area in Fig. 4.11. This area is equivalent to the first Brillouin zone enclosed by the red lines. The Coulomb interaction is modeled as being confined in 2D space as $V_\mathbf{q} \propto \sum_G 1/|\mathbf{q}+\mathbf{G}|$ using eq. (4.12). The sum over the reciprocal vectors is calculated up to the ninth-nearest Brillouin zone to ensure translational symmetry of $V_\mathbf{q}$. The coefficients that define the magnitude of the Coulomb interaction are determined so that the lowest exciton energy matches the A-exciton of monolayer WSe_2 in our experiment (1.63 eV). The resultant absorption spectrum calculated using eq. (4.64) is shown in Appendix B.3. The photo-carrier distribution in k-space is assumed to be proportional to the lowest exciton wave function $|\psi_0(\mathbf{k})|$ (Fig. 4.11(c)). We prepared $|\psi_0(\mathbf{k})|$ by using a fitting with the following trial function:

$$|\psi_0(\mathbf{k})| = \left(\frac{c_0}{\left(c_1 + |f(\mathbf{k})|^2\right)^{c_2}} + c_3\right)\exp\left(-\frac{|f(\mathbf{k})|^2}{\sigma^2}\right) \tag{4.78}$$

The fitting parameters are shown in Table 3.9. The maximum residual of the fitting was 1.6% of the diagonalization result, indicating that the trial function reproduced the numerically obtained wave function. The assumed distribution is further evaluated in Appendix B.3. The total fraction of the population $\sum_\mathbf{q} n_\mathbf{q}$ that corresponds to the carrier density in the experiment is calculated by multiplying the carrier density by the area of the unit cell of monolayer WSe_2.

Table 4.2: Fitting results for the excitonic wave function

parameter	fitting result
c_0	0.00956224
c_1	0.0963467
c_2	0.896374
c_3	0.00254523
σ	4.89707

We phenomenologically treat the momentum relaxation as a relaxation into the equilibrium distribution [14]. γ_m describes the rate of the momentum relaxation. We use the

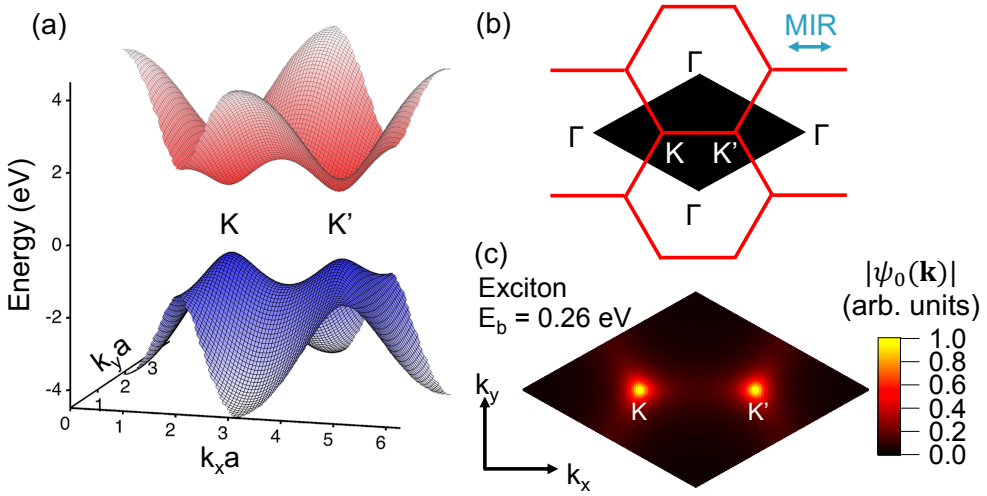

Figure 4.11: Method of numerical calculation (a) Band structure of gapped graphene model (red: conduction band, blue: valence band). (b) Calculated area (black) in k-space that corresponds to the first Brillouin zone. The light blue arrow represents the mid-infrared polarization (zigzag) used in the calculation. (c) Lowest energy exciton wavefunction $\psi_0(\mathbf{k})$ distributed in k-space in the single electron-hole picture. The black rhombic region in (c) corresponds to that in (b). The exciton binding energy was set to 0.26 eV.

equilibrium carrier distribution $n_{k,eq}$ defined by the exciton wave function and total carrier density:

$$n_{k,eq} = \frac{|\psi_0(\mathbf{k})|}{\sum_{\mathbf{q}} |\psi_0(\mathbf{q})|} \sum_{\mathbf{q}} n_{\mathbf{q}} \tag{4.79}$$

so that the total carrier density is conserved when the interband transition is zero. The magnitude of the dipole moment of the lowest energy exciton is estimated from the experimental results of the optical Stark effect for 1s excitons [173]. Reference [173] gives the dipole moment in the two-level system of the exciton. Thus, the dipole moment for single electrons d_{cv} is calculated by dividing the dipole moment of the exciton by an enhancement factor 16/7 in the 2D case under the effective mass approximation [165]. The estimated value is $d_{cv} = 1.5 \times 10^{-29}$ [C· m].

Equations (6-8) are calculated using a 75×75 k-mech in the first Brillouin zone. To calculate the harmonic spectra, we evaluated the harmonic intensity from the intra- and inter-band current defined as

$$\mathbf{J}(t) = \mathbf{J}_{ra}(t) + \mathbf{J}_{er}(t) \tag{4.80}$$

$$\mathbf{J}_{ra}(t) = \frac{2e}{\hbar} \sum_{\mathbf{K}} \frac{\partial}{\partial \mathbf{K}} \varepsilon_g \left(\mathbf{K} - \frac{e}{\hbar} \mathbf{A}(t) \right) n_{\mathbf{K}} \tag{4.81}$$

$$\mathbf{J}_{er}(t) = \frac{2}{\hbar} \sum_{\mathbf{K}} \varepsilon_g \left(\mathbf{K} - \frac{e}{\hbar} \mathbf{A}(t) \right) \mathrm{Im}\left[\mathbf{d}_{cv}^* P_{\mathbf{K}} \right] \tag{4.82}$$

The harmonic spectra are obtained as $I(\omega) \propto |\mathbf{J}(\omega)|^2$. Below, the harmonic intensity at each order is calculated by summing the spectra over the full harmonic spectral width.

4.6 Results of numerical calculations

4.6.1 Full numerical calculations

We solved the SBE in eqs. (4.76) and (4.76), and calculated the intraband and interband currents. $\hbar/\gamma$ was set to 8 fs (a half cycle of the MIR field), which is similar to the value in Ref. [153]. The momentum relaxation time $\hbar/\ \gamma_m$ was set to 16 fs, i.e., slower than the dephasing constant and the EID rate $\hbar/\gamma_e$ was set to 1.8×10^{14} fs cm^{-2} to reproduce the experimental results. The time profiles of the mid-infrared field and intraband and interband current without initial carriers are shown in Figs. 4.12(a) and 4.12(c). The time evolution of the carrier density is shown in Fig. 4.12(c). The carriers are generated by the tunneling process most efficiently when the electric field takes its peak value. This process is repeated for half the period of the MIR electric field. Without dephasing, no real carrier excitation occurs under the non-resonant driver due to the energy conservation. However, excited carriers accumulate when fast dephasing processes are present during the period of the MIR field [136]. Such incoherent carriers contribute to the intraband current, thus, the peak of its amplitude appears later in the pulse duration, as shown in Fig. 4.12(b).

The calculated intraband and interband harmonic spectra without initial carriers are shown in Fig. 4.13(a). Here, only odd-order harmonics appear because the calculated two-band system has inversion symmetry. In this calculation, the interband harmonics are dominant in the energy region above the absorption edge (1.63 eV), whereas the intraband harmonics are relevant in the lower energy region, as several studies have indicated [68, 84]. Next, we calculated the harmonic generation with a finite number of initial carriers. Figure 4.13(b) represents the total harmonic spectra for various photo-carrier densities.

Figures 4.14(a) and 4.14(b) compare the experimental result with the numerical calculation at an initial carrier density of 3.7×10^{12} cm^{-2}. The numerical calculation reproduced the behavior of the positive and negative changes below and above the absorption edge. There was also good agreement on the larger reduction of the higher-order harmonics.

Initial carrier density dependence of differential total harmonic intensity was calculated as shown in Fig. 4.15(a). The corresponding result in the experiment is in Fig. 4.15(b). The photo-carrier density dependences are in good agreement especially for the higher-order harmonics, as is the magnitude of the increase at fifth order for lower initial carrier density. At higher carrier density, the calculated fifth-order harmonics deviate from the dependence obtained from the experiment. In addition, we compared the MIR intensity dependence between the calculation and experiment at an initial carrier density of 3.7×10^{12} cm^{-2}.

The calculated differential harmonic intensity at seventh and higher order harmonics in Fig. 4.16(a) is not significantly dependent on the MIR intensity, which is consistent with the experimental results in Fig. 4.16(b). Although the absolute value of the calculated differential fifth-order harmonics is typically larger than the experimental result, the trend, where the value increases as the MIR intensity decreases, is the same as in the experiment. These results are discussed in sections 4.6.2 and 4.6.3.

To understand the mechanism underlying the observed changes in harmonic intensity due to photo-carrier doping, we calculated the initial carrier density dependence of the intraband and interband currents. In Figs. 4.17, the differential harmonic intensity is normalized by the total harmonic intensity. These results indicate that the increase in the fifth order harmonics is caused by an increase in the intraband contribution (Fig. 4.17(a)).

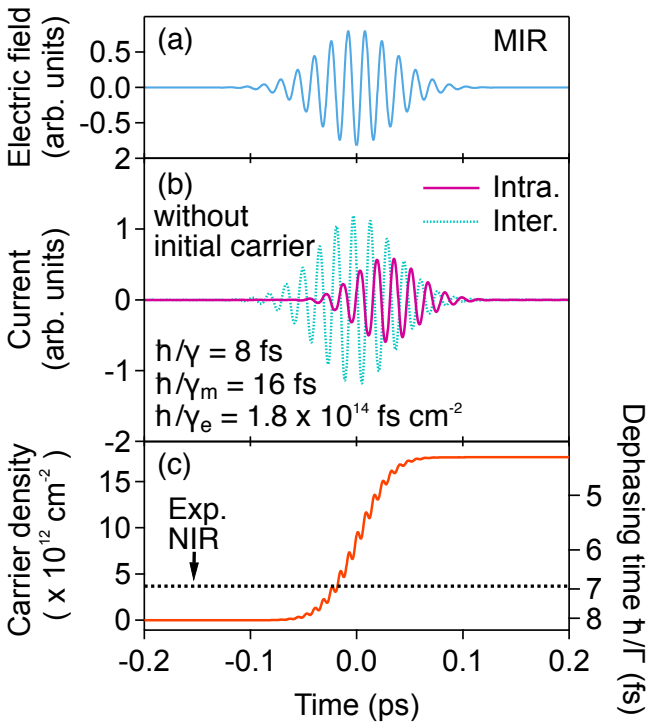

Figure 4.12: Calculated intraband and interband current and evolution of carrier density in the time domain. (a) Time profile of the mid-infrared (MIR) field used in the calculation. (b) Intraband and interband current calculated without initial carriers. (c) Time evolution of carrier density and corresponding dephasing time $\hbar/\Gamma$. The dotted black line represents the photo-carrier density of 3.7×10^{12} cm^{-2} excited by the near-infrared (NIR) pump pulse, corresponding to the experimental condition in Fig. 4.7. The calculation parameters are $\hbar/\gamma = 8$ fs, $\hbar/\gamma_m = 16$ fs, and $\hbar/\gamma_e = 1.8 \times 10^{14}$ fs cm^{-2}. The dephasing time is $\hbar/\Gamma = 4.5$ fs after the MIR pulse passes.

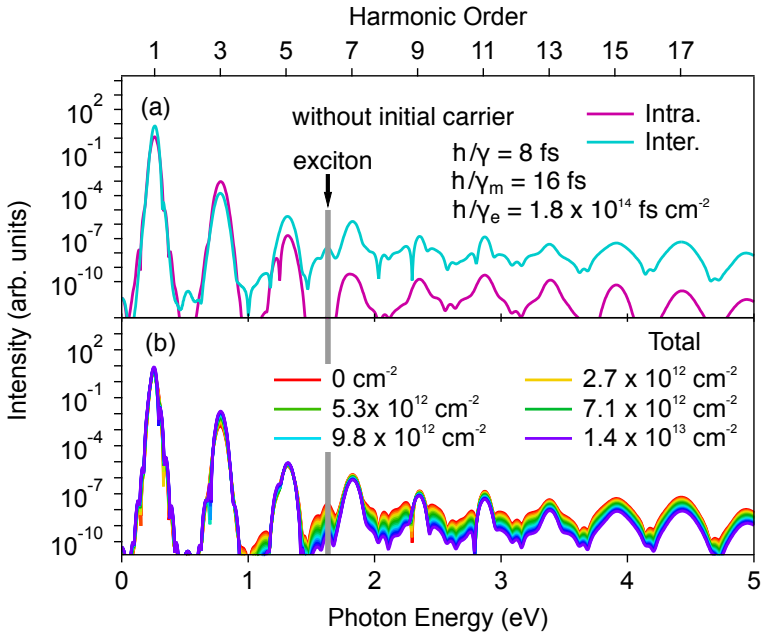

Figure 4.13: Numerical calculation of high harmonic generation spectra with photo-carrier doping effects. The calculation parameters are $\hbar/\gamma = 8$ fs, $\hbar/\gamma_m = 16$ fs, and $\hbar/\gamma_e = 1.8 \times 10^{14}$ fs cm^{-2}. (a) Intraband and interband harmonic spectrum without initial carriers. (b) Total harmonic spectra for various photo-carrier densities. The gray lines represents the lowest exciton energy.

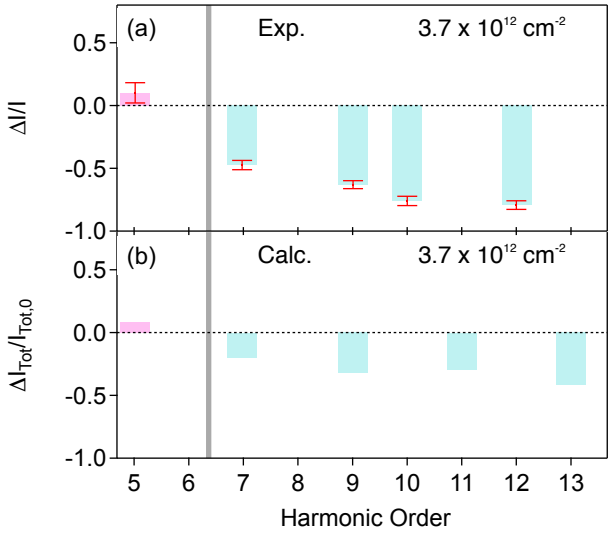

Figure 4.14: Comparison of differential harmonic intensity between (a) experiment and (b) calculation at the initial carrier density of 3.7×10^{12} cm^{-2}. The calculation result in (b) is the differential total harmonic intensity normalized by the total harmonics without initial carriers. The gray lines represents the lowest exciton energy.

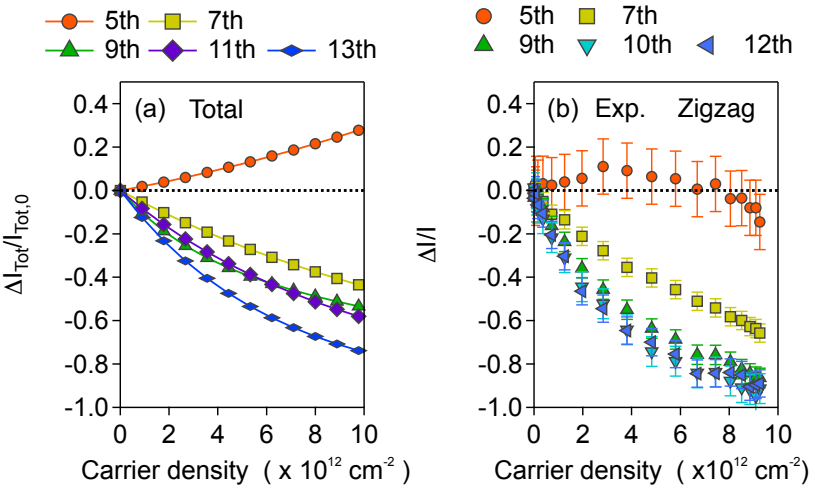

Figure 4.15: Comparison of photo-carrier density dependence of differential harmonic intensity between (a) calculation and (b) experiment in Fig. 4.9(a). The calculation parameters are $\hbar/\gamma = 8$ fs, $\hbar/\gamma_m = 16$ fs, and $\hbar/\gamma_e = 1.8 \times 10^{14}$ fs cm^{-2}.

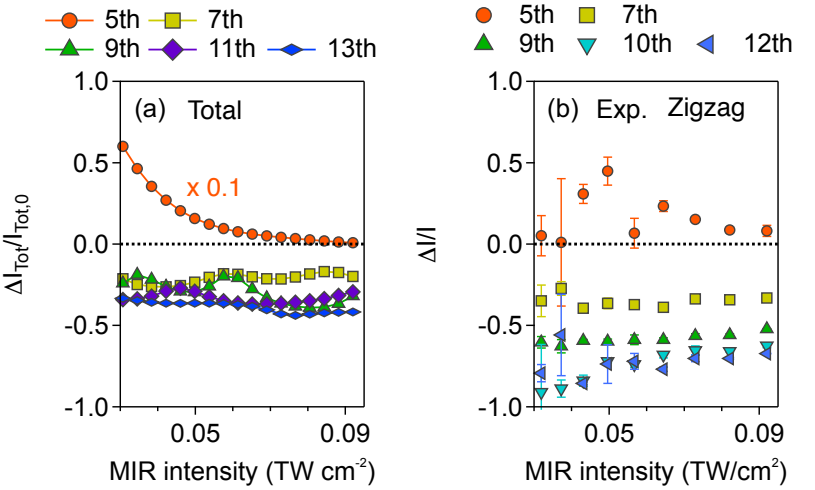

Figure 4.16: Comparison of MIR intensity dependence of differential harmonic intensity between (a) calculation at the initial carrier density of 3.7×10^{12} cm^{-2} and (b) experiment in Fig. 4.10. The fifth-order harmonic intensity in (b) is multiplied by 0.1 for visibility. The calculation parameters are $\hbar/\gamma = 8$ fs, $\hbar/\gamma_m = 16$ fs, and $\hbar/\gamma_e = 1.8 \times 10^{14}$ fs cm^{-2}.

On the other hand, the reductions in the harmonics higher than the absorption edge can be attributed to the reduction in the interband contribution (Fig. 4.17(b)).

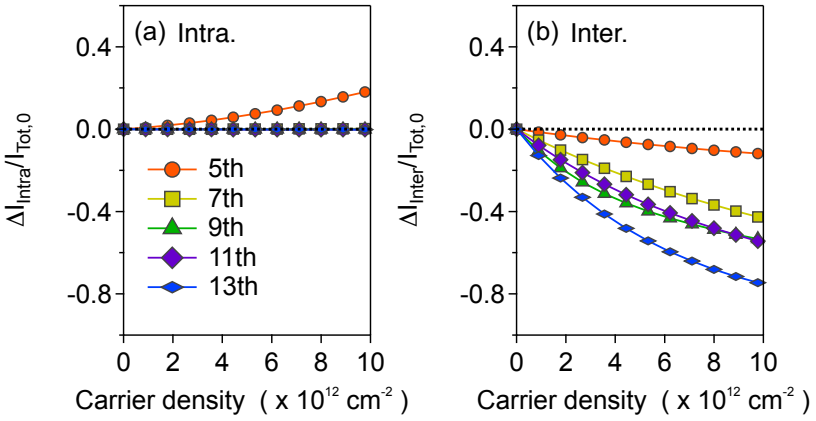

Figure 4.17: Numerical calculation of photo-carrier density dependence of (a) intraband and (b) interband differential harmonic intensity. The calculation parameters are $\hbar/\gamma = 8$ fs, $\hbar/\gamma_m = 16$ fs, and $\hbar/\gamma_e = 1.8 \times 10^{14}$ fs cm^{-2}. Differential intraband and interband harmonic intensity are normalized by the total harmonic intensity calculated without initial carriers.

4.6.2 Switch-off analysis of the photo-carrier doping effects

To clarify the many-body effects included in our calculation, we performed switch-off analyses based on the full numerical simulations described in the previous section. Figure 4.18(a) is a schematic diagram of the four effects included in our calculation: ($\varepsilon 1$) initial carrier distribution, ($\varepsilon 2$) momentum relaxation, ($\varepsilon 3$) excitation-induced dephasing (EID), and ($\varepsilon 4$) excitonic effect. Here, we discuss the initial carrier density dependence of the differential harmonic intensity on the four effects by removing their contributions one at a time.

The initial carriers may enhance the intraband harmonics due to the acceleration of the photo-carriers and also suppress the interband harmonics through the phase-space filling effect. Figure 4.19(a) compares the full calculation (ON, filled markers) and a calculation without the initial carrier distribution $n_q(t=0) = 0$ (OFF, unfilled markers), which is a similar condition to the previous work where the initial carrier density dependence is effectively included in the increased dephasing rate at $t = 0$ through the EID [155]. Here, we could not reproduce the increase in the fifth-order harmonics, as shown by the unfilled circles in Fig. 4.19(a). This indicates that intraband acceleration of the incoherent initial carriers should be relevant to the increase in the fifth-order harmonics, which is consistent with the result in Fig. 4.17(a). On the other hand, intraband acceleration of the incoherent carriers does not affect the harmonics above the absorption edge where the interband mechanism is dominant. Note that the increase in the EID rate in turn increases the incoherent carriers excited by the strong MIR field, and it might lead to an increase in the fifth-order intraband current. However, this effect is not significant enough in the calculation to explain the increase in the fifth-order harmonics. We also found little dif-

ferences in the seventh- and ninth-order harmonics. This indicates the phase-space filling effect is negligible in this calculation.

Figure 4.19(b) shows the results for the momentum relaxation. Without momentum relaxation ($\hbar/\gamma_m = \infty$), the fifth-order harmonics increase by one order of the magnitude and clearly deviate from our experimental observations, where the enhancement was only about 10%. This is because the intraband current is suppressed by the momentum relaxation as shown Fig. B.4. This indicates the significance of the momentum relaxation to the HHG process.

Figure 4.19(c) shows the results for the EID. Without EID ($\hbar/\gamma_e = \infty$), we could not reproduce the large suppression of higher order harmonics above the absorption edge, where the interband mechanism is the dominant. Given the result in Fig. 4.19(a), this result indicates that the EID should be the main cause of the reduction in HHG, not the phase-space filling effect.

Figure 4.19(d) shows results for the excitonic effect derived from the strong Coulomb interaction in monolayer WSe_2. Without the excitonic effect ($V_q = 0$), there are large increases in the fifth- and seventh-order harmonics. If exciton effects were absent, the bandgap of the single electron would be between the energies of the seventh and ninth harmonics (1.89 eV). Thus, the intraband contribution would be remarkable even as the seventh order harmonic intensity increases with the initial carrier density (yellow unfilled squares in Fig. 4.19(d)). This indicates that the excitonic absorption edge and not the single-electron bandgap energy determines the HHG mechanism near the edge. Summarizing above discussions, it is clear that we need to include all four contributions, i.e., the initial carrier distribution, momentum relaxation, excitation-induced dephasing (EID), and excitonic effect, to reproduce the experimental effects of photo-doping on HHG.

Note that the rate of EID $\hbar/\gamma_e = 1.8 \times 10^{14}$ fs cm^{-2}, i.e.,$\gamma_e = 3.7 \times 10^{-12}$ meV cm^2, which is determined to reproduce the experimental results in our calculation, is very similar to the value $\gamma_e = 2.7 \times 10^{-12}$ meV cm^2 estimated from the homogeneous linewidth of the exciton in monolayer WSe_2 at low temperature [158]. The rate of EID for excitons in GaAs divided by the thickness of monolayer WSe_2 (6.5 Å) is $\gamma_e = 2.5 \times 10^{-12}$ or 2.5×10^{-11} meV cm^2 [158, 170]. These results point to the validity of including EID in our calculation.

4.6.3 Contributions of incoherent electron-hole pairs generated by MIR driving field for HHG

The calculations in sections 4.6.1 and 4.6.2 revealed the significance of EID in the HHG process. Here, we evaluate the impact of incoherent carriers generated by a strong MIR pulse itself on HHG through EID. Figure 4.12(a) shows the total carrier density without initial carriers and the corresponding evolution of the dephasing time $\hbar/\Gamma$. According to our simulation, an MIR pulse with a peak electric field of 8.3 MV cm^{-1} creates carriers with a density of approximately 10^{13} cm^{-2} at the center of the pulse duration. This carrier density is comparable to or higher than the density of the doped photo-carriers in the experiment in Fig. 4.7 (the black dotted line in Fig. 4.12(a)). These incoherent carriers created by the MIR pulse promote the dephasing process. The calculated dephasing time decreases from 8 fs to 6 fs at the center of the mid-infrared field. This suggests the importance of EID during the MIR pulse irradiation. An MIR driving field with a longer pulse duration may create more incoherent carriers and suppress the high harmonics in

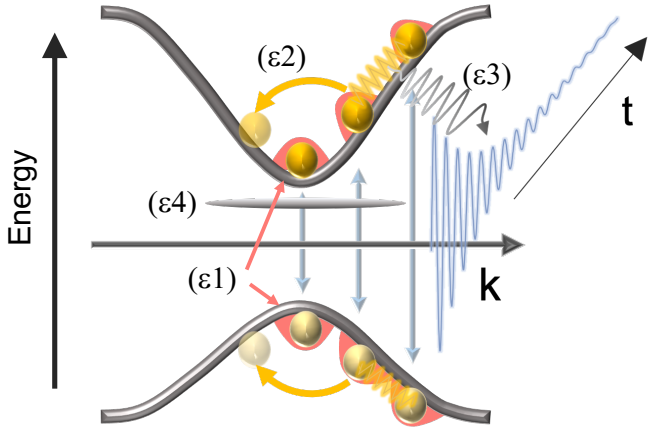

Figure 4.18: Schematics of the four effects: ($\varepsilon 1$) initial carrier distribution, ($\varepsilon 2$) momentum relaxation, ($\varepsilon 3$) excitation-induced dephasing (EID), and ($\varepsilon 4$) excitonic effect.

the ultraviolet or higher energy region.

The previous sections assumed that EID increases linearly with respect to the carrier density. The validity of this assumption is supported by the experimentally observed MIR intensity dependence, which can be explained as follows. We generally write the carrier density dependent dephasing rate as $\Gamma\left(N_{MIR}\left(I_{MIR}\right)+N_{NIR}\right)$, where N_{NIR} is the incoherent photo-carrier density and $N_{MIR}\left(I_{MIR}\right)$ is the incoherent carrier density generated by the MIR pulse depending on the intensity I_{MIR}. Since the interband harmonics is exponentially dependent on the dephasing rate as shown in Fig. B.5 [155], the ratio between the n-th order interband harmonic intensity with $\left(I^n{}_{Inter}\left(I_{MIR}\right)\right)$ and without $\left(I^n{}_{Inter,0}\left(I_{MIR}\right)\right)$ photo-carrier doping is expressed as

$$I^n{}_{Inter}\left(I_{MIR}\right)=I^n{}_{Inter,\,0}\left(I_{MIR}\right)\exp\left[-\frac{\Gamma\left(N_{MIR}\left(I_{MIR}\right)+N_{NIR}\right)-\Gamma\left(N_{MIR}\left(I_{MIR}\right)\right)}{\Gamma_n}\right] \tag{4.83}$$

where Γ_n is a normalization parameter for the n-th order harmonics. The normalized differential harmonic intensity is given by

$$\frac{\Delta I^n_{Inter}\left(I_{MIR}\right)}{I^n{}_{Inter,\,0}\left(I_{MIR}\right)}=\exp\left[-\frac{\Gamma\left(N_{MIR}\left(I_{MIR}\right)+N_{NIR}\right)-\Gamma\left(N_{MIR}\left(I_{MIR}\right)\right)}{\Gamma_n}\right]-1. \tag{4.84}$$

On the other hand, the experiment showed no significant change for the seventh and higher order harmonics in Fig. 4.15(b). This can only be explained when the right hand side of eq. (4.84) is independent of the MIR intensity, i.e., the dephasing rate is linearly dependent on the carrier density.

In Fig. 4.15(a), the fifth-order differential harmonic intensity increases by lowering the MIR intensity. This is because N_{NIR} becomes relatively larger than $N_{MIR}\left(I_{MIR}\right)$ at lower MIR intensity and results in a relatively large enhancement in the intraband harmonics that is significant at fifth order. This is similar in trend to the experimental results in Fig. 4.15(b) and supports the idea of including the initial carrier distribution in the simulation. On the other hand, our calculation overestimates the increase in the fifth-order harmonics. This may be due to the effect of electron-electron scattering that are not included in our calculation.

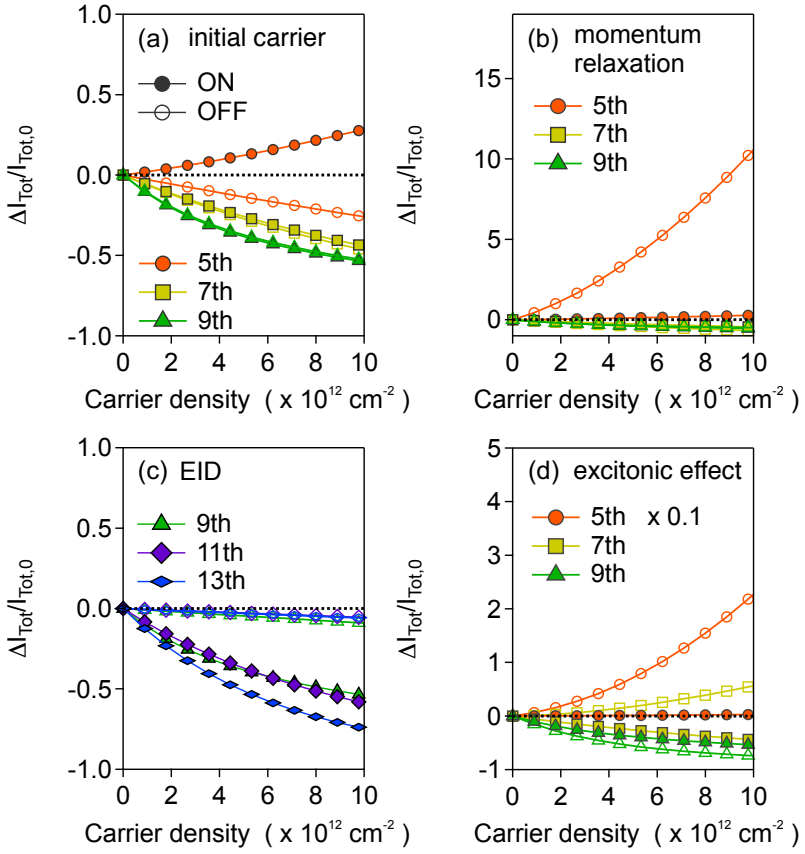

Figure 4.19: Switch-off analysis of four effects: ($\varepsilon 1$) initial carrier distribution, ($\varepsilon 2$) momentum relaxation ($\varepsilon 3$) excitation-induced dephasing (EID) and ($\varepsilon 4$) excitonic effect. Calculated initial carrier density dependence of differential total harmonic intensity normalized by the total harmonic intensity without initial carriers. Filled and unfilled markers represent the results of full and switched-off calculations, respectively. The switched-off results were calculated by respectively setting (a) $n_q(t=0)=0$, (b) $\hbar/\gamma_m=\infty$, (c) $\hbar/\gamma_e=\infty$, and (d) $V_q=0$. For the calculation in (a), the initial carrier density dependence is effectively included in the increased dephasing rate at t=0 through the EID. The fifth-order harmonic intensity in (a) is multiplied by 0.1 for visibility.

The calculated initial carrier density dependence for the fifth-order harmonics in Fig. 4.15(a) deviates from the observed dependence in Fig. 4.15(b) at high photo-carrier densities. The calculated dependence monotonically increases with increasing the carrier density but the experimental result reaches the maximum value at a certain density and starts to decrease after that. This experimental result may be reproduced by considering the temperature rise due to the strong electron-electron scattering at higher carrier density, which reduces the intraband harmonics (see Fig. B.6). The above considerations point to the necessity of including the photo-carrier doping effects discussed in section 4.6.2 and suggest the crucial role in HHG of incoherent carriers generated by the MIR pulse itself through EID.

4.7 Effect of carrier dynamics on dynamical symmetry in ultrashort laser pulse

In this section we discuss how much DS is broken in strongly MIR light-driven semiconductors.

4.7.1 Effect on excitation-induced dephasing on dynamical symmetry

In many numerical calculations for HHG, the dephasing time is assumed to be constant, and the effect of time-varying dephasing due to EID has not been explored. The time-varying dephasing may disrupt the time translational symmetry of the electronic system in the periodically driven semiconductor. Here, we evaluate the effect of EID on HHG and DS by using the EID rate estimated from our experiment and calculation. Figure 4.20 compares the harmonic spectra in the case where EID is taken into account and the case where the dephasing rate at the center of the pulse is kept constant from the beginning. Figures 4.20 (a,b) displays the temporal profile of the MIR pulse and the computed dephasing time. The red and yellow-green curves in Fig. 4.20 respectively represent the case with and without time-varying dephasing. The corresponding spectra are shown in Fig. 4.20 (c). The spectra are calculated via the same condition as that in Fig. 4.13 without initial carriers. In the comparison between the red and yellow-green spectra, we found no significant change, such as peak shift of the harmonics observed in HHG from graphene [58]. This indicates that the effect of its temporal variation within the pulse width is not significant on the shape of the resulting spectrum. Also, this shows that the time-varying dephasing in the driving pulse duration does not significantly disturb the DS.

In our study for semiconductors, the total number of excited carriers is estimated to be several percent after the strong MIR pulse passes. Thus, our calculation showed this amount of the carriers is not enough to cause phase-space filling in the HHG process. However, the application of the strong pulse to a narrow gap semiconductor may make the phase-space filling effect more obvious because a number of carriers are generated. This may break the time translational symmetry of the periodically driven system.

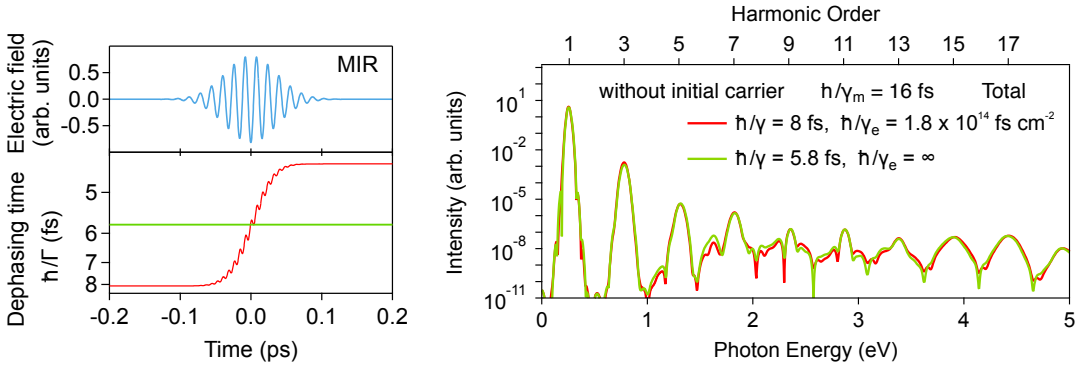

Figure 4.20: Effect of time-varying dephasing in the driving pulse duration on high harmonic generation (HHG). (a) Temporal profile of the MIR electric field. (b) Temporal profile of the dephasing time in the case where EID is taken into account (red curve) and the case where the dephasing rate at the center of the pulse is kept constant from the beginning (yellow-green curve). (c) Comparison of the harmonic spectra corresponding to the dephasing time in (b). The spectra were calculated using the method explained in Fig. 4.13. The initial carriers are set to 0. The calculation parameters are $\hbar/\gamma = 8$ fs, $\hbar/\gamma_m = 16$ fs, and $\hbar/\gamma_e = 1.8 \times 10^{14}$ fs cm^{-2} for the red curve, and $\hbar/\gamma = 5.8$ fs, $\hbar/\gamma_m = 16$ fs, and $\hbar/\gamma_e = \infty$ for the green curve, respectively.

4.7.2 Time-translational symmetry in ultrashort laser pulse

In previous research, clear evidence of time-translational symmetry breaking was observed in semiconductors in ultrashort laser pulses, where the frequency of the harmonic peak deviates from the integer multiples of the fundamental pulse frequency [55,64]. Both experiments used few-cycle driving pulses whose temporal profiles of driving laser fields were far from the periodic ones. Our experiments used the MIR pulse with a duration of 60 fs, which includes approximately six laser cycles in its duration. This resulted in the harmonic peaks at the integer multiples of the fundamental frequency throughout our study. This contributes to the description of Floquet's picture used in the HSG analysis working well.

4.8 Summery

We studied the effects of incoherent electron-hole pairs on high harmonic generation in an ideally thin semiconductor under a strong MIR field. We found that, due to the photo-carrier doping, the harmonic intensity changes positively and negatively below and above the absorption edge. To describe the photo-carrier doping effect, we performed numerical simulations phenomenologically considering both the electron-electron scattering process and the photo-doped carrier distributions. They showed that photo-carriers enhance the intraband current relevant to lower-order harmonics, which is relatively suppressed by momentum relaxation. We also showed that photo-carriers significantly suppress the interband current that contributes to higher-order harmonics above the absorption edge. We clarified that the main suppressive effect is not the phase-space filling but rather the EID. Our work revealed that many-body effects such as the electron-electron scattering beyond

the single-active electron picture play a crucial role in the solid-state HHG, although they do not break the symmetry of the periodically driven system. These findings provide a basic understanding of high harmonic spectroscopy in solids and the generation of broad-band light from solids.

Chapter 5

Conclusion and outlook

5.1 Conclusion

In this study, we focused on the dynamical symmetry (DS), which is promising for generally describing the nature of strongly light-driven electronic systems. We investigated the validity of DS in solids, which has been still unclear, by performing two experiments. Throughout this thesis, we used monolayer transition metal dichalcogenides. These materials allow us to discuss high harmonic generation (HHG) and high order sideband generation (HSG) without considering propagation effects, such as reabsorption and phase matching. In addition, these materials facilitate the theoretical analysis since they can be treated as a two-dimensional system rather than a three-dimensional system.

Since HSG is a phenomenon induced by two light pulses of different frequencies, the polarization selection rule for HSG provides more information about the symmetry than the one for HHG. In our experiments, we generated high order sidebands by applying intense mid-infrared light and weak near-infrared light nearly resonant with the absorption edge of the material. We obtained clear polarization selection rules for linear and circular polarizations. We proposed a physical picture of HSG as "Raman scattering in the Floquet system", which comprehensively explains the selection rules. As a result, we found perfect agreement in the experimentally and theoretically obtained selection rules. This indicates that DS, which describes the coherent time evolution of a single electron, well illustrates the strong light-driven electronic system in semiconductors.

Meanwhile, one remarkable effect that can break DS in solids is the accumulation of incoherent carriers during the application of a strong infrared pulse. To investigate this effect, we studied incoherent photo-carrier doping on HHG. We observed HHG in monolayer WSe_2 and confirmed a weak enhancement of the fifth harmonic (appearing at the lower energy side of the absorption edge) and a strong suppression of the higher harmonics (at higher energy side of the absorption edge) following the photo-carrier doping. Numerical calculations reproducing the experimental results showed that the enhancement of the fifth order harmonics is owing to increased intraband current by the photo-carriers, which is suppressed by the momentum relaxation. We also found that the decrease in the high order interband harmonics is not due to phase-space filling but the effect of excitation-induced dephasing. The numerical results suggest that the incoherent carriers generated by the mid-infrared light pulse promote the dephasing of the interband polarization in the latter half of the MIR pulse duration.

We summarize these two studies. The first study showed that the electronic state in

an intense mid-infrared pulse can be well described by DS based on the coherent time evolution of a single electron. However, the second study showed that the fast scattering phenomena on a timescale comparable to the mid-infrared electric field period is promoted by the accumulation of incoherent carriers, which inhibits the coherent motion of a single electron. This indicates that it is necessary to consider the many-body effects for a detailed understanding of HHG. Due to the many-body effect, one may intuitively expect that the accumulation of incoherent carriers in the pulse duration disrupts the time periodicity. However, we showed that these effects are not significant enough to interfere with the DS of the system and the resulting polarization selection rules. Therefore, we concluded that DS symmetry is useful for describing nonperturbative light-matter interactions in semiconductors under strong MIR light field. This provides a general insight for further nonperturbative optical phenomena and Floquet engineering of semiconductors.

5.2 Outlook

Regarding the DS, in Chapter 3, the symmetry mainly used to understand the polarization selection rule is the operator accompanied by time-translational symmetry. The validity of time-reversal symmetry is still unclear. Dissipative processes may hinder these symmetries in solids. In fast, our study for black phosphorous revealed the breaking of the time-reversal symmetry by observing the elliptically polarized high harmonics under linearly polarized field [174]. It remains to be verified in what cases this symmetry is valid in solids. In Chapter 4, we performed numerical calculations of higher harmonics using a simplified model to more comprehensively understand the underlying physics. The reproduction of the experimentally obtained HHG spectra has yet to be done within this work. Future theoretical studies on the mechanism of HHG should take account of an ab-initio band structure, dipole moment structure, and Berry curvature, which are simplified or neglected in our study.

This thesis has focused on the generation of higher harmonics in semiconductors. However, in metals and strongly correlated electron systems in strong light fields, the DS may be broken due to the strong effects of many-body interaction. It will be interesting to understand how DS works in such strongly correlated systems using the more sophisticated formalism of DS in many-body Floquet systems. It is also essential to systematically clarify how the many-body effect affects the DS when a field-effect transistor structure largely controls the Fermi level in semiconductors. A high doping density of carriers may cause screening of the Coulomb interaction between electrons, and they allow studying its role for HHG. Furthermore, it will also be an interesting research subject to clarify how the interactions of electrons with spins and phonons modify the electronic dynamics in a strong field.

Although our experiment focused on monolayer TMDs in this thesis, we also investigated HHG from nano-size materials such as black phosphorous and carbon nanotubes in recent works [84, 174]. In principle, we can generate high harmonics in any material. The fact that a wide variety of materials show characteristic responses to a strong light field indicates another direction for strong-field physics in solids as material science.

The strong field physics in solid-state systems leaves many aspects to be developed in the future. Vigorous experimental and theoretical research will lead to discovering novel physical phenomena and point the way to further directions in this research field.

Appendix A

A.1 Estimation of pulse durations

Here, we show how to estimate the pulse duration of the NIR and MIR pulses used in HSG measurement. We consider gaussian envelops for the MIR and NIR electric field

$$E_{MIR}(t) = E_M^{(0)} \exp\left(-\frac{t^2}{2\tau_M^2}\right) \tag{A.1}$$

$$E_{NIR}(t) = E_N^{(0)} \exp\left(-\frac{t^2}{2\tau_N^2}\right), \tag{A.2}$$

where $E_{MIR}(t)$ and $E_{NIR}(t)$ are the envelops of the MIR and NIR electric field respectively. τ_M and τ_N are related to the full width at half maximum of MIR ($\mathrm{FWHM_M}$) and NIR ($\mathrm{FWHM_N}$) pulses as follows:

$$\mathrm{FWHM_M} = 2\tau_M\sqrt{\ln(2)} \tag{A.3}$$

$$\mathrm{FWHM_N} = 2\tau_N\sqrt{\ln(2)}. \tag{A.4}$$

The pulse duration of NIR pulses after passing through the bandpass filter and liquid crystal retarder was measured as 110 fs (FWHM) by SPIDER (Spectral Phase Interferometry for Direct Electric-field Reconstruction). We estimated the pulse duration of the MIR pulses from the time delay dependence of the first-order sideband intensity.

One of the conventional methods to examine an unknown pulse duration is the cross-correlation method, where an unknown pulse duration is estimated from the time delay dependence of the sum-frequency generation (SFG) in a nonlinear optical media with another known pulse. According to the perturbation theory, the electric field generated by SFG of the NIR and MIR pulses at each time t' is given by

$$E_{SFG}(t,t') \propto E_{MIR}(t-t')\, E_{NIR}(t'), \tag{A.5}$$

where the optical response of the media is assumed to be instantaneous. t is the time delay of the NIR and MIR pulses. When the intensity of SFG is measured by a detector that has no time resolution, the integrated intensity $I_{SFG}(t)$ is given by

$$I_{SFG}(t) \propto \int dt' \left|E_{MIR}(t-t')\, E_{NIR}(t')\right|^2 \propto \int dt' I_{MIR}(t-t')\, I_{NIR}(t'). \tag{A.6}$$

The MIR pulse duration can be derived from this expression. However, the sideband generation is a non-perturbative phenomenon; excitation power dependence does not follow the power law. Thus, we modify the analysis of the cross-correlation method. We

approximate the instantaneous response of sideband generation and write the first-order sideband intensity as

$$I_S(t) \propto \int dt' f\left(I_{MIR}\left(t-t'\right)\right) I_{NIR}\left(t'\right) \tag{A.7}$$

with a nonlinear function f. The function f is determined by fitting the obtained the MIR excitation power dependence of the sideband intensity $F\left(I_{MIR,0}\right)$, where $I_{MIR,0}$ is the peak power of the MIR pulses written as

$$I_{MIR,0} = \frac{1}{2} c\varepsilon_0 E_M^{(0)^2}, \tag{A.8}$$

c is the speed of light and ε_0 is the permittivity in a vacuum. We assume that the function f can be approximately written as

$$f(I) = 1 - \exp\left(-\frac{I}{w_1}\right), \tag{A.9}$$

which is convex and satisfies $f(0) = 0$. The function f works so that the time duration of $f\left(I_{MIR}(t)\right)$ becomes longer than that of $I_{MIR}(t)$. The excitation power dependence $F\left(I_{MIR,0}\right)$ is measured at time delay 0, therefore that is given by

$$\begin{aligned} F\left(I_{MIR,0}\right) &= C\int dt' f\left(I_{MIR}\left(-t'\right)\right) I_{NIR}\left(t'\right) \\ &= C'\int dt' \left(1-\exp\left(-\frac{I_{MIR,0}}{w_1}\exp\left(-\frac{t'^2}{\tau_M^2}\right)\right)\right)\exp\left(-\frac{t'^2}{\tau_N^2}\right), \end{aligned} \tag{A.10}$$

where C and C' are constants. Furthermore, the time delay dependence $G(t)$ is give by

$$\begin{aligned} G(t) &= C\int dt' f\left(I_{MIR}\left(t-t'\right)\right) I_{NIR}\left(t'\right) \\ &= C'\int dt' \left(1-\exp\left(-\frac{I_{MIR,0,max}}{w_1}\exp\left(-\frac{\left(t-t'\right)^2}{\tau_M^2}\right)\right)\right)\exp\left(-\frac{t'^2}{\tau_N^2}\right). \end{aligned} \tag{A.11}$$

$I_{MIR,0,max}$ is the maximum MIR power, which was used for the measurement of the time delay dependence. The parameters C', τ_M, and w_1 are determined through the global fitting of the experimental results. As a result, $\mathrm{FWHM_M}$ was estimated to be 60 fs from τ_M. The fitting curves by eqs. (A.10) and (A.11) are shown by solid lines in Fig. A.1.

A.2 Frequency component of $J_{SG}\left(t\right)$

We show $J_{SG}(t)$ emits the electric field that has the sideband frequency components. According to eqs. (3.6), the tensor $\chi^{e_F}_{\mu,\nu}(t,t')$ satisfies the following temporal periodicity:

$$\chi^{e_F}_{\mu,\nu}\left(t,t'\right) = \chi^{e_F}_{\mu,\nu}\left(t+2\pi l/\omega_{MIR}, t'+2\pi l'/\omega_{MIR}\right), \tag{A.12}$$

where l, l' are integers. Thus, $\chi^{e_F}_{\mu,\nu}(t,t')$ can be expanded in a Fourier series as follows:

$$\chi^{e_F}_{\mu,\nu}\left(t,t'\right) = \sum_{l,l\prime} a^{e_F}_{\mu,\nu,l,l'} e^{il\omega_{MIR}t} e^{-il'\omega_{MIR}t\prime}. \tag{A.13}$$

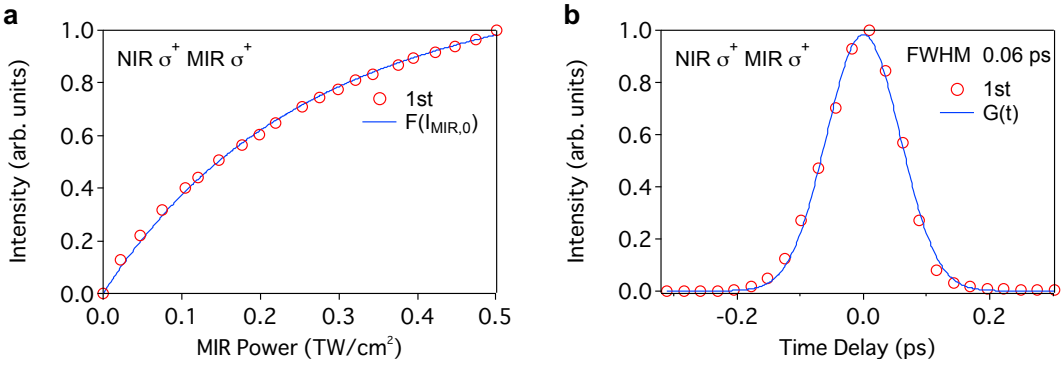

Figure A.1: Estimation of MIR pulse duration. **a**, **b** MIR power dependence (**a**) and time delay dependence (**b**) of the first order sideband intensity under σ^+-polarized NIR and MIR pulses. The blue solid lines in (**a**) and (**b**) are the fitting result with $F(I_{MIR,0})$ and $G(t)$, respectively.

Note that $\chi^{e_F}_{\mu,\nu}(t,t')$ can also be expanded on the basis of the Floquet modes [127], however, the representation of eq. (A.13) would become lengthy. When the NIR light is a continuous wave, the Fourier component of $\mathbf{J}_{SG}(t)$ can be written explicitly. We write the NIR light as $\delta A_{NIR,\nu}(t') = \delta A_{0,\nu} e^{-i\omega_{NIR}t'}$ by applying the rotating wave approximation. To simplify the discussion, we only consider the first term of eq. (3.11) because the complex conjugate term just gives the time-reversal pair of the current. We consider the damping Γ and then obtain

$$J_{SG,\mu}(\omega) = -\frac{i}{\hbar}\sum_{\nu,l,l'}\sum_{e_F\neq i_F} a^{e_F}_{\mu,\nu,l,l'}\delta A_{0,\nu}\int_{-\infty}^{\infty}dt\int_{-\infty}^{t}dt' e^{-(i\omega_{ei}+\Gamma)(t-t')} \times e^{il\omega_{MIR}t}e^{-il'\omega_{MIR}t'}e^{-i\omega_{NIR}t'}e^{i\omega t}. \tag{A.14}$$

By calculating the integral with respect to t' and taking the limit of $\Gamma \to +0$, we get

$$\begin{aligned} J_{SG,\mu}(\omega) &= -\frac{i}{\hbar}\sum_{\nu,l,l'}\sum_{e_F\neq i_F} a^{e_F}_{\mu,\nu,l,l'}\delta A_{0,\nu}\int_{-\infty}^{\infty}dt\frac{e^{i(l-l')\omega_{MIR}-\omega_{NIR}+\omega)t}}{-l'\omega_{MIR}-\omega_{NIR}+\omega_{ei}-i0} \\ &= -\frac{2\pi i}{\hbar}\sum_{\nu,l,l'}\sum_{e_F\neq i_F} a^{e_F}_{\mu,\nu,l,l'}\delta A_{0,\nu}\frac{1}{-l'\omega_{MIR}-\omega_{NIR}+\omega_{ei}-i0} \\ &\quad\times\delta\left(\left(l-l'\right)\omega_{MIR}-\omega_{NIR}+\omega\right)\right) \end{aligned} \tag{A.15}$$

Therefore, the current $\mathbf{J}_{SG}(t)$ is the sum of the m-th order frequency component written as

$$\begin{aligned} J_{SG,\mu}(t) &= \sum_m J_{SG,\ m,\mu}(t) \\ &= -\frac{i}{\hbar}\sum_m\sum_{\nu,l}\sum_{e_F\neq i_F} a^{e_F}_{\mu,\nu,l,l'}\delta A_{0,\nu}\frac{1}{-(m+l)\omega_{MIR}-\omega_{NIR}+\omega_{ei}-i0}e^{-i(\omega_{NIR}+m\omega_{MIR})t}. \end{aligned} \tag{A.16}$$

A.3 Derivation of " Raman tensor "

In this section, we derive the symmetry constraint on " Raman tensor " discussed in Section 3.5.2

A.3.1 Definition of dynamical symmetry

Here, we show the definition of the DS operation n this thesis. We basically follow the definition and the notation of DS operations studied by Neufeld, O. et al. [98]. Accordingly, the time-reversal operation is included in our discussion of DS. We regard a "static" symmetry (i.e., pure spatial symmetry) operation as one of the DS operations [99]. Note that we distinguish the following two different definitions of the DS operations.

1. Operations for the vector component and temporal part of the electric fields (denoted as $\hat{X}$)
2. Corresponding unitary and anti-unitary operations in quantum mechanics for the position of the electron and time (**r**,t) (denoted as $\hat{X}_q$)

A.3.2 Symmetry constraint on microscopic model

We derive the DS constraint on the microscopic model introduced in Section 3.5.1. We show only the example for the DS operations that are accompanied by the temporal translation. Note that the microscopic model is also restricted by the DS operations accompanied by the time-reversal operation. In the following, to simplify the discussion, we only consider the first term of eq. (3.11). We consider the DS operation $\hat{X}^t = \hat{X}_s \cdot \hat{\tau}^t$ for the MIR driven system, where $\hat{X}_s$ is an operation for the spatial component of the vectors and $\hat{\tau}^t$ is a time-translation operation for the time t by Δt. By applying this operation for the current $\mathbf{J}_{SG}(t)$ in eq. (3.11), we obtain

$$\begin{aligned}
\hat{X}^t \mathbf{J}_{SG}(t) &= -\frac{i}{\hbar} \sum_{e_F \neq i_F} \hat{X}^t \int_{-\infty}^{t} dt' e^{-i\omega_{ei}(t-t')} \chi^{e_F}\left(t,t'\right) \delta \mathbf{A}_{NIR}\left(t'\right) \\
&= -\frac{i}{\hbar} \sum_{e_F \neq i_F} \int_{-\infty}^{t+\Delta t} dt'' e^{-i\omega_{ei}(t+\Delta t-t')} \hat{X}_s \chi^{e_F}\left(t+\Delta t,t'\right) \hat{X}_s^{-1} \hat{X}_s \delta \mathbf{A}_{NIR}\left(t'\right) \\
&= -\frac{i}{\hbar} \sum_{e_F \neq i_F} \int_{-\infty}^{t} dt'' e^{-i\omega_{ei}(t-t'')} \hat{X}_s \chi^{e_F}\left(t+\Delta t,t''+\Delta t\right) \hat{X}_s^{-1} \hat{X}_s \delta \mathbf{A}_{NIR}\left(t''+\Delta t\right) \\
&= -\frac{i}{\hbar} \sum_{e_F \neq i_F} \int_{-\infty}^{t} dt'' e^{-i\omega_{ei}(t-t'')} \hat{X}^t \chi^{e_F}\left(t,t''\right) \left(\hat{X}^{t''}\right)^{-1} \hat{X}^{t''} \delta \mathbf{A}_{NIR}\left(t''\right), \qquad \text{(A.17)}
\end{aligned}$$

where $\hat{X}^{t''}$ operates on time t''.

In the following, we prove the equation

$$\hat{X}^t \chi^{e_F}\left(t,t''\right) \left(\hat{X}^{t''}\right)^{-1} = \chi^{e_F}\left(t,t''\right). \qquad \text{(A.18)}$$

For preparation, we discuss the symmetry of the Hamiltonian and wave functions. When $\hat{X}^t$ is a DS operator of the MIR driven system, the corresponding operator commutes with

the Hamiltonian (eq. (3.2)) as following :

$$\hat{X}_q^t \hat{H}_0(t) = \hat{H}_0(t) \hat{X}_q^t. \tag{A.19}$$

The same should hold for the Floquet Hamiltonian

$$\hat{X}_q^t \hat{H}_F(t) = \hat{H}_F(t) \hat{X}_q^t. \tag{A.20}$$

We consider the simplest case where the eigenstates of $\hat{H}_F(t)$ are nondegenerate. In this case, the eigenstates are simultaneous eigenstates of $\hat{H}_F(t)$ and $\hat{X}^t$. Hence, for eigenstate $|\Phi_\alpha(t)\rangle$ of $\hat{H}_F(t)$,

$$\hat{X}_q^t |\Phi_F(t)\rangle = e^{i\delta} |\Phi_F(t)\rangle \tag{A.21}$$

holds, where the phase δ is a real number. As a result, we get

$$\begin{aligned} \hat{X}^t \left\langle i_F(t) \left| \frac{\partial \hat{H}_0(t)}{\partial \mathbf{A}(t)} \right| e_F(t) \right\rangle &\equiv \left\langle i_F(t) \left| \left(\hat{X}_q^t\right)^\dagger \frac{\partial \hat{H}_0(t)}{\partial \mathbf{A}(t)} \hat{X}_q^t \right| e_F(t) \right\rangle \\ &= \left\langle i_F(t) \left| \frac{\partial\, \hat{H}_0(t)}{\partial\, \mathbf{A}(t)} \right| e_F(t) \right\rangle e^{i(\delta_i - \delta_e)}, \end{aligned} \tag{A.22}$$

where δ_i and δ_e are the phases in eq. (A.21) corresponding to $|i_F\rangle$ and $|e_F\rangle$, respectively. Through the same discussion for $\hat{X}^{t\prime\prime}$, eq. (A.18) can be demonstrated. By combining eq. (A.18) with eq. (A.17), we obtain

$$\hat{X}^t \mathbf{J}_{SG}(t) = -\frac{i}{\hbar} \sum_{e_F \neq i_F} \int_{-\infty}^{t} dt'' e^{-i\omega_{ei}(t-t'')} \chi^{e_F}\left(t, t''\right) \hat{X}^{t\prime\prime} \delta\mathbf{A}_{NIR}\left(t''\right) + c.c.. \tag{A.23}$$

This equation gives a relation between the polarization of the NIR and the sideband. Note that this discussion is valid even in the case that the eigenstates are degenerate through the same discussion for the degeneracy studied by Neufeld, O. et al. [98].

A.3.3 Derivation of symmetry constraint on " Raman tensor "

The relation in eq. (A.23) can be transformed into a simpler form as the invariance of " Raman tensor " under DS operation. When the NIR light is a continuous wave, any vector potential $\delta\mathbf{A}_{NIR}(t'')$ can be written as a linear combination of " eigenvectors " of DS operator, which are summarized in Table A.1. For example, if $\hat{C}_{3,\sigma_M}$ is a DS operator of the system, $\delta\mathbf{A}_{NIR}(t) = \delta A_{NIR}(1,-i)^T e^{i\omega_{NIR}t}$ is an eigenvector satisfying

$$\hat{C}_{3,\sigma_M} \begin{pmatrix} 1 \\ -i \end{pmatrix} e^{i\omega_{NIR}t} = e^{i\frac{2\pi}{3}} e^{-i\frac{2\pi\omega_{NIR}}{3\omega_{MIR}}\sigma_M} \begin{pmatrix} 1 \\ -i \end{pmatrix} e^{i\omega_{NIR}t}, \tag{A.24}$$

where ω_{NIR} is angular frequency of the NIR light. When $\delta\mathbf{A}_{NIR}(t)$ satisfies

$$\hat{X}^t \delta\mathbf{A}_{NIR}(t) = e^{i\theta} \delta\mathbf{A}_{NIR}(t), \tag{A.25}$$

the tensor product of $\hat{X}^t \mathbf{J}_{SG}(t)$ and $\hat{X}^t \delta\mathbf{A}_{NIR}(t)$ is given by

$$\begin{aligned}
&\hat{X}^t \mathbf{J}_{SG}(t) \left(\hat{X}^t \mathbf{A}_{NIR}(t)\right)^\dagger \\
&= -\frac{i}{\hbar} \sum_{e_F \neq i_F} \int_{-\infty}^{t} dt'' e^{-i\omega_{ei}(t-t'')} \chi^{e_F}\left(t,t'\right) \hat{X}^{t''} \delta\mathbf{A}_{NIR}\left(t''\right) \left(\hat{X}^t \mathbf{A}_{NIR}(t)\right)^\dagger \\
&= -\frac{i}{\hbar} \sum_{e_F \neq i_F} \int_{-\infty}^{t} dt'' e^{-i\omega_{ei}(t-t'')} \chi^{e_F}\left(t,t'\right) \delta\mathbf{A}_{NIR}\left(t''\right) e^{i\theta} \delta\mathbf{A}_{NIR}^\dagger(t) e^{-i\theta} \\
&= -\frac{i}{\hbar} \sum_{e_F \neq i_F} \int_{-\infty}^{t} dt'' e^{-i\omega_{ei}(t-t'')} \chi^{e_F}\left(t,t'\right) \delta\mathbf{A}_{NIR}\left(t''\right) \delta\mathbf{A}_{NIR}^\dagger(t) \\
&= \mathbf{J}_{SG}(t) \delta\mathbf{A}_{NIR}^\dagger(t). \qquad \text{(A.26)}
\end{aligned}$$

According to eq.(A.23), the symmetry constraint can be reduced into

$$\hat{X}^t \mathbf{J}_{SG,m}(t) \left(\hat{X}^t \delta\mathbf{A}_{NIR}(t)\right)^\dagger = \mathbf{J}_{SG,m}(t) \delta\mathbf{A}_{NIR}^\dagger(t) \qquad \text{(A.27)}$$

by comparing the m-th order frequency component of both sides in eq. (A.26). When the electric field of the sideband is given by eq. (2.27), by considering $E_{NIR}(t) = -\frac{\partial(\delta A_{NIR}(t))}{\partial t}$, we get

$$\hat{X}^t \mathbf{E}_{SG,m}(t) \left(\hat{X}^t \mathbf{E}_{NIR}(t)\right)^\dagger = \mathbf{E}_{SG,m}(t) \mathbf{E}_{NIR}(t)^\dagger \qquad \text{(A.28)}$$

This equation indicates the invariance of "Raman tensor" under the DS operation :

$$\hat{X}^t \mathscr{R}_m(t) = \mathscr{R}_m(t) \qquad \text{(A.29)}$$

$$\mathscr{R}_m(t) = \mathbf{E}_{SG,m}(t) \mathbf{E}_{NIR}^\dagger(t). \qquad \text{(A.30)}$$

A.4 Derivation of HSG selection rules from dynamical symmetry

We require the invariance of " Raman tensor " under DS operations to derive selection rules. In the following, we show examples of the derivations of the selection rules on HSG in monolayer TMDs. All symmetry constraints under the circularly and linearly polarized MIR field are summarized in Table 3.1.

A.4.1 Case 1— Circularly polarized MIR light

Invariance under $\hat{D}_{\mathrm{y}}$

We write the " Raman tensor " by using an electric field of the NIR and m-th order sideband light as follows:

$$\mathscr{R}_m(t) = \mathbf{E}_{SG,m}(t) \mathbf{E}_{NIR}^\dagger(t) \qquad \text{(A.31)}$$

Table A.1: Dynamical symmetry operation and eigenvector. Reproduced from the supplemental document of K. Nagai *et al.*, Communications Physics **3**, 137 (2020). [1].

Dynamical symmetry operation		**Eigenvector**		**Eigenvalue**
Spatial operation	$\hat{\sigma}_y$	Spatial part	$\begin{pmatrix}1\\0\end{pmatrix},\begin{pmatrix}0\\1\end{pmatrix}$	$+1,-1$
	$\hat{R}_n$		$\begin{pmatrix}1\\-i\end{pmatrix},\begin{pmatrix}1\\i\end{pmatrix}$	$e^{i\frac{2\pi}{n}},e^{-i\frac{2\pi}{n}}$
Temporal operation	$\hat{\tau}_n$	Temporal part (NIR)	$e^{i\omega_{\mathrm{NIR}}t}$	$e^{-i\frac{2\pi\omega_{\mathrm{NIR}}}{n\omega_{\mathrm{MIR}}}}$
	$\hat{\mathcal{T}}$		$\cos(\omega_{\mathrm{NIR}}t),\sin(\omega_{\mathrm{NIR}}t)$	$+1,-1$
	$\hat{\mathcal{T}}\cdot\hat{\tau}_2$		$\cos\left(\omega_{\mathrm{NIR}}t-\frac{\omega_{\mathrm{NIR}}\pi}{2\omega_{\mathrm{MIR}}}\right)$, $\sin\left(\omega_{\mathrm{NIR}}t-\frac{\omega_{\mathrm{NIR}}\pi}{2\omega_{\mathrm{MIR}}}\right)$	$+1,-1$

where $E_{SG,m}(t)=\sin\left((\omega_{NIR}+m\omega_{MIR})t+\phi_S\right)\left(E_{SG,m,x},E_{SG,m,y}\right)^T$ and $E_{NIR}(t)=\sin\left(\omega_{NIR}t+\phi_N\right)\left(E_{NIR,x},E_{NIR,y}\right)^T$ denote the electric field of the sideband and NIR light, respectively. Note that $\left(E_{NIR,x},E_{NIR,y}\right)^T$ must be $(1,0)^T$ or $(0,1)^T$, and ϕ_N must be 0 or $\pi/2$ under $\hat{D}_y$ since the electric field of the NIR and sideband light must be eigenvectors of $\hat{D}_y$. ϕ_N can be set to 0 without loss of generality. By requiring $\hat{D}_y\mathscr{R}_m=\mathscr{R}_m$, the relation between the electric field of the NIR and sideband light can be obtained. For example, under y-polarized NIR field (i.e., $E_{NIR,x}=0$), the electric field of the sideband light is constrained as

$$E_{SG,m,x}=0 \text{ and } \phi_S=0 \tag{A.32}$$

or

$$E_{SG,m,y}=0 \text{ and } \phi_S=\pi/2. \tag{A.33}$$

The sideband can be a linear combination of allowed two cases:

$$E_{SG,m}(t)=\begin{pmatrix}\cos\left((\omega_{NIR}+m\omega_{MIR})t\right)\\ b\sin\left((\omega_{NIR}+m\omega_{MIR})t\right)\end{pmatrix}, \tag{A.34}$$

where b is a real number. This demonstrates that the sideband light can be elliptical polarization with a major or minor axis parallel to the x-axis. In the same way, we can also determine constraints on the sideband light under x- polarized NIR field. Thus, the selection rule for $\hat{D}_y$ in Table 3.1 is obtained, which is similar to the result of the selection rules of HHG shown in Chapter 2 [98].

Invariance under $\hat{C}_{n,\sigma_{\mathbf{M}}}$

Here, we discuss the invariance of " Raman tensor " under $\hat{C}_{n,\sigma_M}$ (n : integer). We write the " Raman tensor " by using the electric field of the NIR and m-th order sideband light as follows:

$$\mathscr{R}_m(t) = \mathbf{E}_{S,m}(t)\,\mathbf{E}^{\dagger}_{NIR}(t) = \exp(im\omega_{MIR}t)\begin{pmatrix} 1 & i\sigma_N \\ -i\sigma_S^m & \sigma_S^m\sigma_N \end{pmatrix}, \tag{A.35}$$

where $E_{S,m} = \exp(i(\omega_{NIR}+m\omega_{MIR})t)\left(1,-i\sigma_S^m\right)^T$,$E_{NIR} = \exp(i\omega_{NIR}t)(1,-i\sigma_N)^T$. By requiring $\hat{C}_{n,\sigma_M}\mathscr{R}_m = \mathscr{R}_m$, we obtain

$$(\hat{\tau}_{-n\sigma_M}\exp(im\omega_{MIR}t))(\hat{R}_n\begin{pmatrix} 1 & i\sigma_N \\ -i\sigma_S^m & \sigma_N\sigma_S^m \end{pmatrix}) = \exp(im\omega_{MIR}t)\begin{pmatrix} 1 & i\sigma_N \\ -i\sigma_S^m & \sigma_N\sigma_S^m \end{pmatrix} \tag{A.36}$$

$$\exp\left(i\left(m\omega_{MIR}t - m\frac{2\pi\sigma_M}{n}\right)\right)\exp\left(i(\sigma_S^m-\sigma_N)\frac{2\pi}{n}\right)\begin{pmatrix} 1 & i\sigma_N \\ -i\sigma_S^m & \sigma_N\sigma_S^m \end{pmatrix} = \exp(im\omega_{MIR}t)\begin{pmatrix} 1 & i\sigma_N \\ -i\sigma_S^m & \sigma_N\sigma_S^m \end{pmatrix}, \tag{A.37}$$

where the operation of the rotation $\hat{R}_n$ to the matrix part is represented by

$$\hat{R}_n\begin{pmatrix} 1 & i\sigma_N \\ -i\sigma_S^m & \sigma_N\sigma_S^m \end{pmatrix} \tag{A.38}$$

$$= \begin{pmatrix} \cos(2\pi/n) & -\sin(2\pi/n) \\ \sin(2\pi/n) & \cos(2\pi/n) \end{pmatrix}\begin{pmatrix} 1 & i\sigma_N \\ -i\sigma_S^m & \sigma_N\sigma_S^m \end{pmatrix}\begin{pmatrix} \cos(2\pi/n) & \sin(2\pi/n) \\ -\sin(2\pi/n) & \cos(2\pi/n) \end{pmatrix}. \tag{A.39}$$

Thus, the symmetry constraint can be written by

$$m\sigma_M + \sigma_N - \sigma_S^m = nN. \tag{A.40}$$

where N is an integer. Note that $\hat{D}_y$ gives no further restrictions for the sideband under circularly polarized NIR field. We show an example of the circular polarization selection rules given in Table 3.2. Since monolayer TMDs have three-fold rotational symmetry, n is 3 in our experiment. When the MIR and NIR light is left circular polarized ($\sigma_M, \sigma_N = 1$), σ_S^m must be equal to $m+1-3N$ according to the eq. (A.40). Thus, $\sigma_S^1 = -1$ with $N = 1$, and $\sigma_S^3 = 1$ with $N = 0$ are allowed, but there is no solution for σ_S^2, which indicates that the second-order sideband is forbidden. The other cases of the circular polarization selection rules shown in Table 3.2 are also derived similarly.

A.4.2 Case 2-1— x-polarized MIR light

We have discussed the operation $\hat{D}_y$, thus, we only deal with the $\hat{Z}_y$.

Invariance under $\hat{Z}_y$

We write the " Raman tensor " by using the electric field of the NIR and m-th order sideband light as follows:

$$\mathscr{R}_m(t) = \mathbf{E}_{S,m}(t)\,\mathbf{E}^{\dagger}_{NIR}(t) = \exp(im\omega_{MIR}t)\begin{pmatrix} E_{S,m,x}E^*_{NIR,x} & E_{S,m,x}E^*_{NIR,y} \\ E_{S,m,y}E^*_{NIR,x} & E_{S,m,y}E^*_{NIR,y}\end{pmatrix}, \tag{A.41}$$

where $(E_{NIR,x}, E_{NIR,y})^T$ is $(1,0)^T$ or $(0,1)^T$. By requiring $\hat{Z}_y\mathscr{R}_m = \mathscr{R}_m$, we obtain

$$(-1)^m\begin{pmatrix} E_{S,m,x}E^*_{NIR,x} & E_{S,m,x}E^*_{NIR,y} \\ E_{S,m,y}E^*_{NIR,x} & E_{S,m,y}E^*_{NIR,y}\end{pmatrix} = \begin{pmatrix} E_{S,m,x}E^*_{NIR,x} & -E_{S,m,x}E^*_{NIR,y} \\ -E_{S,m,y}E^*_{NIR,x} & E_{S,m,y}E^*_{NIR,y}\end{pmatrix}. \tag{A.42}$$

Here, the term $(-1)^m$ is attributed to the half-period temporal translation in $\hat{Z}_y$. The electric field of the sideband light is constrained as

$$E_{S,m,x} = 0 \ (m:\text{even}) \text{ and } E_{S,m,y} = 0 \ (m:\text{odd}) \tag{A.43}$$

under y-polarized NIR field (i.e., $E_{NIR,x} = 0$) and

$$E_{S,m,y} = 0 \ (m:\text{even}) \text{ and } E_{S,m,x} = 0 \ (m:\text{odd}) \tag{A.44}$$

under x-polarized NIR field (i.e., $E_{NIR,y} = 0$). As a result, the polarizations of the odd-order sidebands are perpendicular to the NIR field and even-order sidebands are parallel. Note that this selection rule is stricter than that derived from $\hat{D}_y$. We also note that Langer et al. observed elliptically polarized sidebands in monolayer WSe_2 under a circularly polarized NIR field [13]. This experimental result is consistent with our theory since both $\hat{D}_y$ and $\hat{Z}_y$ do not restrict the polarization of the sideband under circularly polarized NIR field.

A.4.3 Case 2-2— y-polarized MIR light

Invariance under $\hat{\sigma}_y$

We write the " Raman tensor " by using the electric field of the NIR and m-th order sideband light as follows:

$$\mathscr{R}_m(t) = \mathbf{E}_{S,m}(t)\,\mathbf{E}^{\dagger}_{NIR}(t) = \exp(im\omega_{MIR}t)\begin{pmatrix} E_{S,m,x}E^*_{NIR,x} & E_{S,m,x}E^*_{NIR,y} \\ E_{S,m,y}E^*_{NIR,x} & E_{S,m,y}E^*_{NIR,y}\end{pmatrix}, \tag{A.45}$$

where $(E_{NIR,x}, E_{NIR,y})^T$ is $(1,0)^T$ or $(0,1)^T$. By requiring $\hat{\sigma}_y\mathscr{R}_m = \mathscr{R}_m$, we obtain

$$E_{S,m,x} = 0 \tag{A.46}$$

under y-polarized NIR field (i.e., $E_{NIR,x} = 0$) and

$$E_{S,m,y} = 0 \tag{A.47}$$

under x-polarized NIR field (i.e., $E_{NIR,y} = 0$). This indicates that all sidebands have the same polarization as that of the NIR field.

Invariance under $\hat{H}_y$

We write the " Raman tensor " by using the electric field of the NIR and m-th order sideband light as follows:

$$\begin{aligned}
&\mathscr{R}_m(t) = \mathbf{E}_{SG,m}(t)\,\mathbf{E}^{\dagger}_{NIR}(t) \\
&= \sin\left((\omega_{NIR}+m\omega_{MIR})t - \frac{(\omega_{NIR}+m\omega_{MIR})\pi}{2\omega_{MIR}} + \phi_S\right)\sin\left(\omega_{NIR}t - \frac{\omega_{NIR}\pi}{2\omega_{MIR}} + \phi_N\right) \\
&\times \begin{pmatrix} E_{S,m,x}E^*_{NIR,x} & E_{S,m,x}E^*_{NIR,y} \\ E_{S,m,y}E^*_{NIR,x} & E_{S,m,y}E^*_{NIR,y} \end{pmatrix},
\end{aligned} \tag{A.48}$$

where $(E_{NIR,x}, E_{NIR,y})^T$ is $(1,0)^T$ or $(0,1)^T$, and ϕ_N must be 0 or $\pi/2$ under $\hat{D}_y$ since the electric field of the NIR and sideband light must be eigenvectors of $\hat{D}_y$. ϕ_N can be set to 0 without loss of generality. Under y-polarized NIR field (i.e., $E_{NIR,x} = 0$), by requiring $\hat{D}_y\mathscr{R}_m = \mathscr{R}_m$, the electric field of the sideband light is constrained as

$$E_{SG,m,x} = 0 \text{ and } \phi_S = 0 \tag{A.49}$$

or

$$E_{SG,m,y} = 0 \text{ and } \phi_S = \pi/2. \tag{A.50}$$

The sideband can be a linear combination of allowed two cases:

$$\mathbf{E}_{SG,m}(t) = \begin{pmatrix} \cos\left((\omega_{NIR}+m\omega_{MIR})t - \frac{(\omega_{NIR}+m\omega_{MIR})\pi}{2\omega_{MIR}}\right) \\ b\sin\left((\omega_{NIR}+m\omega_{MIR})t - \frac{(\omega_{NIR}+m\omega_{MIR})\pi}{2\omega_{MIR}}\right) \end{pmatrix}, \tag{A.51}$$

where b is a real number. This demonstrates that the sideband light can be elliptical polarization with a major or minor axis parallel to the x-axis. In the same way, we can also determine constraints on the sideband light under x-polarized NIR field. Thus, the selection rule for $\hat{H}_y$ in Table 3.1 is obtained, which is similar to the selection rules of HHG [98]. Note that the selection rule derived from $\hat{\sigma}_y$ is stricter than that derived from $\hat{H}_y$.

Appendix B

B.1 Derivation of the fitting function

We derive the equation for the fitting considering exciton-exciton annihilation (EEA) and absorption saturation. First, we consider a rate equation for two-level systems. The rate equation used for the modeling is

$$\frac{dN_1}{dt} = -k_A N_1^2 - \alpha \frac{I_p(t)}{\hbar\omega_N}(N_1 - N_2) \tag{B.1}$$

where k_A is the EEA rate and N_1,N_2 are the population per unit area in level 1 and 2, respectively. N_1 corresponds to the population of the exciton. $I_p(t)$ is the intensity of the near-infrared (NIR) pulse, and α is the optical cross section of the NIR photon on the monolayer. The photon energy of the NIR pulse is assumed to be resonant with the two-level systems. First, we calculate the absorbance of the NIR probe beam with the initial population $N_1 = N_i$. The absorbance is defined by the change between the population before and after the probe pulse irradiation. Since the EEA is typically slower than the NIR pulse width ($\sim$ 100 fs), we will neglect the first term in the eq. (B.1) and solve

$$\frac{dN_1}{dt} = -\alpha \frac{I_p(t)}{\hbar\omega}(N_1 - N_2) \tag{B.2}$$

to calculate N_1 just after the probe pulse irradiation. We assume $N_1 + N_2 = N_T$, where the N_T is the total number of the two-level system. By defining $\Delta N(t) = N_2 - N_1$, we get

$$\Delta N(t) = \Delta N(0) \exp\left(-\frac{F_p}{F_S}\right) \tag{B.3}$$

where

$$F_p = \int_{-\infty}^{t} dt I_p(t) \tag{B.4}$$

is the NIR probe fluence and $F_S = \hbar\omega/\alpha$ is the saturation fluence. The absorbance (optical density) is calculated by

$$A(N_i) = \left.\frac{dN_1\hbar\omega_N}{dF_p}\right|_{F_p=0} = -\frac{1}{2}\left.\frac{d\Delta N\hbar\omega_N}{dF_p}\right|_{F_p=0} = \frac{\Delta N\hbar\omega_N}{2F_S} \tag{B.5}$$

Here, $A = A(0) = N_T\hbar\omega/2F_S$ corresponds to the absorbance without the pump pulse. On the other hand, in the case of the transparent substrate, the difference of the transmission

signal between for the monolayer on the substrate and for bare substrate is proportional to absorbance of the monolayer [142],

$$\frac{T-T_s}{T_s} = -\frac{2}{n_S+1}A \tag{B.6}$$

Here, $T\,(T_s)$ is the transmittance for the monolayer WSe_2 on the substrate (bare substrate) and $n_S = 1.76$ is the refractive index of the sapphire substrate at 1.63eV [161]. When the absorbance of the monolayer is small, the differential transmittance due to the photo-carrier doping is given by

$$\frac{\Delta T}{T} \approx -\frac{2}{n_S+1}\Delta A = -\frac{2}{n_S+1}\left(A\left(N_i\right)-A\left(0\right)\right) = \frac{\hbar\omega_N}{F_S}\frac{2N_1}{n_S+1} \tag{B.7}$$

Next, we calculate the carrier density excited by the pump NIR pulse. It can be calculated by replacing the fluence of the probe pulse in eq. (B.3) with that of the pump pulse F_N. By assuming $N_i = 0$, we obtain the population before the relaxation process:

$$N_1\left(0\right) = \frac{AF_S}{\hbar\omega_N}\left(1-\exp\left(-\frac{F_N}{F_S}\right)\right). \tag{B.8}$$

The population at the time delay t is calculated by considering EEA process:

$$\frac{dN_1}{dt} = -k_A N_1^2. \tag{B.9}$$

By solving this equation, we obtain

$$N_1\left(t\right) = \frac{N_1\left(0\right)}{1+k_A N_1\left(0\right)t}. \tag{B.10}$$

Finally, we obtain the differential transmittance at the time delay t from eqs. (B.7), (B.8), (B.10) as follows:

$$\frac{\Delta T}{T} = \frac{\hbar\omega_N}{F_S}\frac{2}{n_S+1}\frac{N_1\left(0\right)}{1+k_A N_1\left(0\right)t} = \frac{2A}{n_S+1}\frac{1-\exp\left(-\frac{F_N}{F_S}\right)}{1+k_A\frac{AF_S}{\hbar\omega_N}\left(1-\exp\left(-\frac{F_N}{F_S}\right)\right)t} \tag{B.11}$$

The global fitting in Fig. 4.6 was performed by using eq. (B.11) with common free parameters A, k_A, F_S.

B.2 Photo-carrier doping effect on HHG in multilayer WSe_2

We performed the photo-carrier doping experiment for HHG in multilayer 2H-WSe_2 to compare the results with that in the monolayer. The sample was prepared by the same method as that in Chapter 4 on a sapphire substrate. The thickness of the sample was estimated to be from 25 to 30 nm by using an atomic force microscope (SHIMADZU, SPM-9700HT). The crystal axis was not determined in this experiment.

Figure B.2(a) shows the HHG spectra obtained from the multilayer WSe_2 with the same MIR intensity as that used for the monolayer WSe_2. We could observe the third-order harmonics from the multilayer, although we could not observe that from monolayer WSe_2. The spectra were obtained using an InGaAs line detector and the same grating spectrometer as the other experiments (Kymera 193i, Andor). The third-order harmonic intensity from the monolayer was below that from the sapphire substrate. Only odd-order harmonics are observed since the bulk TMDs have inversion symmetry. The harmonic intensity exponentially decreases with increasing the order, which is different from the monolayer. This may be because the harmonics from each monolayer in the multilayer cause constructive or destructive interference that modulates the magnitude of the intraband and interband harmonics obtained from the sample. Although the thickness of the layer is smaller than the wavelength, the propagation effect may contribute noticeably to the harmonic spectrum. Alternatively, the strong Coulomb interaction in the monolayer may enhance the efficiency of HHG in the monolayer. Figure B.2(b) shows the dependence of the differential harmonic intensity on the NIR pump fluence. We set the time delay to 1 ps. Here, we observed a similar trend to the monolayer, where the higher-order harmonics largely decrease due to the NIR pump. We also observed a significant increase of the third-order harmonics, whose photon energy is much lower than the absorption edge. The differential harmonic intensity of the third-order changes from decrease to increase with increasing the NIR fluence. This may also be due to the spatial interference of the harmonics radiated in the multilayer or the interference of the microscopic HHG (intraband and interband) mechanisms. This result indicates that the observed photo-carrier doping effect is not a unique process for monolayer, where a strong Coulomb interaction exists.

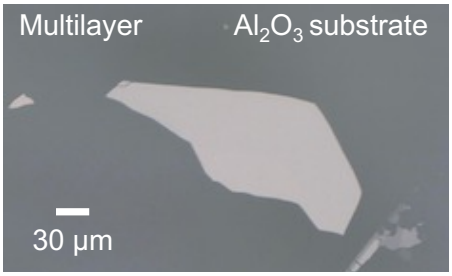

Figure B.1: Photograph of multilayer 2H-WSe_2 on a sapphire substrate used for the experiment.

B.3 Excitonic absorption and wave function

Figure B.3(a) shows the absorption spectrum calculated using eq. (4.64). The computed single-particle bandgap energy is 1.89 eV. A clear peak exciton peak was confirmed in the calculated spectrum. We determined the magnitude of Coulomb interaction so that the lowest energy exciton peak matches that in our experiment (1.63 eV). We confirmed that the application of NIR pulse resonant with this excitonic peak computed in SBE results in the electron distribution in k-space according to the excitonic wave function. Therefore, we prepared the initial carrier distribution in k-space to match the excitonic wave function.

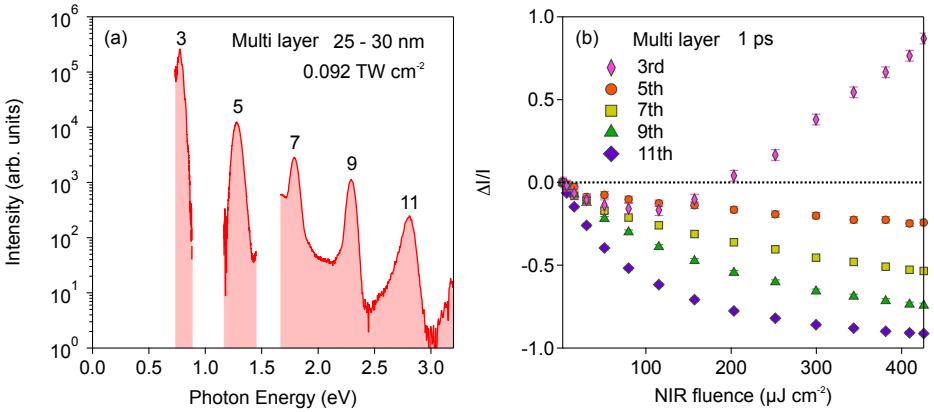

Figure B.2: (a) High harmonic generation spectra obtained from multilayer 2H-WSe_2. (b) The dependence of differential harmonic intensity on the near-infrared (NIR) pump fluence.

Figure B.3 shows the comparison between the excitonic wave function and Fermi-Dirac distribution. The broadening of the excitonic wave function is as large as that of the Fermi-Dirac distribution at 6000 K or 8000 K. A more accurate treatment of Coulomb interaction in monolayer TMDs using Keldysh potential may decrease the population in the region far from the K and K′ points [112]

B.4 Effect of the momentum relaxation on intraband harmonics

Figures B.4 shows results of the numerical calculation of the intraband harmonics without (red) and with (blue) momentum relaxation of $\hbar/\gamma_m = 16$ fs with the initial carrier density of 3.7×10^{12} cm^{-2}. In this calculation, the dipole moment is set to 0 to neglect the effect of interband transitions for simplicity. The spectra show exponential decays with increasing the harmonic order, which is derived from the Bloch oscillation of the initial carriers [68]. The dependence of each order intraband harmonics on momentum relaxation rate is shown in Fig. B.4(b). The momentum relaxation rate up to a moderate rate exponentially suppresses the intraband harmonics. The momentum relaxation returns the carrier distribution in a strong field to a symmetric distribution in k-space and cancels the intraband current.

B.5 Dephasing rate dependence of the intraband harmonic intensity

Figure B.5 represents the dephasing rate dependence of interband harmonics at each order. The interband harmonics above the absorption edge nearly exponentially decreas with respect to the dephasing rate around that used for our calculation (shown by the black arrow).

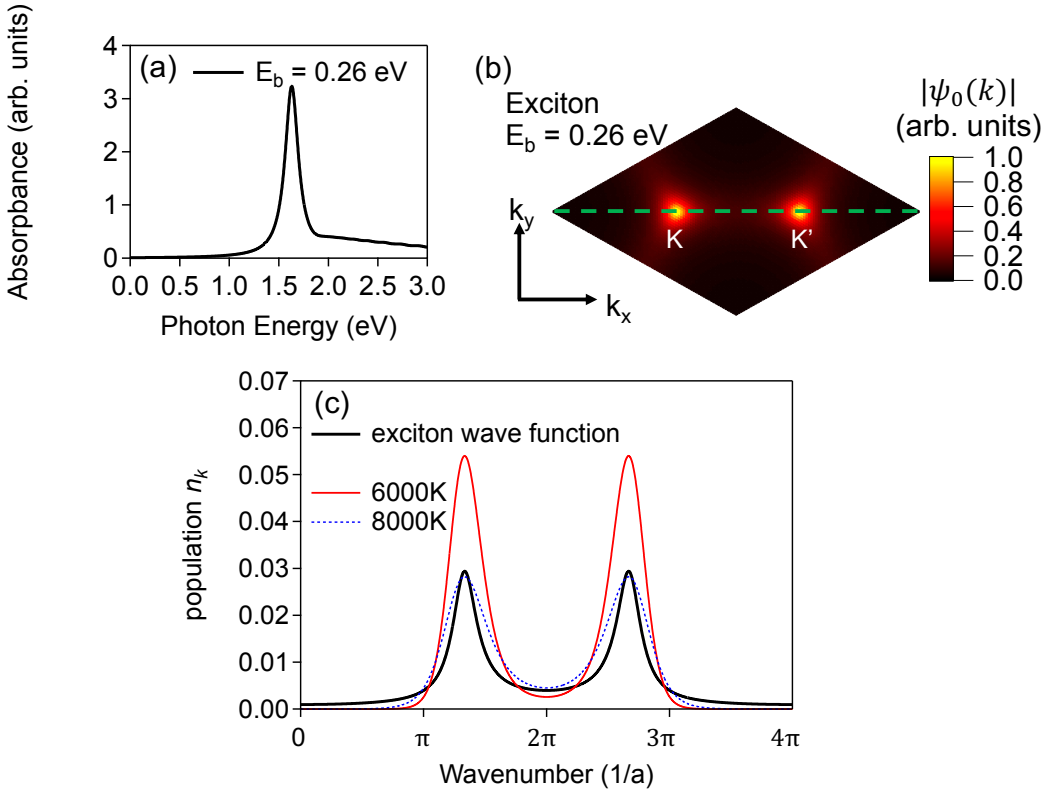

Figure B.3: (a) Absorption spectrum calculated by using eq. (4.64). The damping constant is $\gamma = 0.082$ eV. The exciton binding energy is 0.26 eV. (b) Lowest energy exciton wave function $\psi_0(k)$ distributed in k-space in the single electron-hole picture. (c) The electron distribution with a total population of 3.7×10^{12} cm^{-2} (0.0034 electrons per unit cell) assumed to be proportional to the excitonic wave function (black solid line) and Fermi-Dirac distribution at 6000K (red solid line) and at 8000K (blue dashed line), respectively. The green dashed line in (b) represents the k-points calculated for (c). The temperature and Fermi energy were varied in such a way as to conserve the total population.

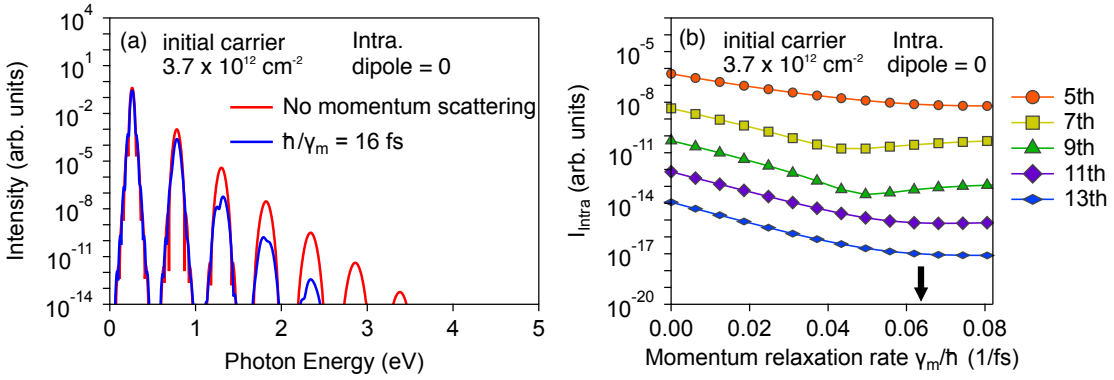

Figure B.4: (a) Intraband harmonic spectra with the initial carrier density of 3.7×10^{12} cm^{-2}. The dipole moment was set to 0 to calculate the spectra. Two spectra represent the results with $\hbar/\gamma_m = \infty$ (red) and $\hbar/\gamma_m = 16$ fs (blue). (b) Momentum relaxation rate dependence of intraband harmonic intensity. The black arrow indicates the rate of 16 fs, which is used for the full calculation.

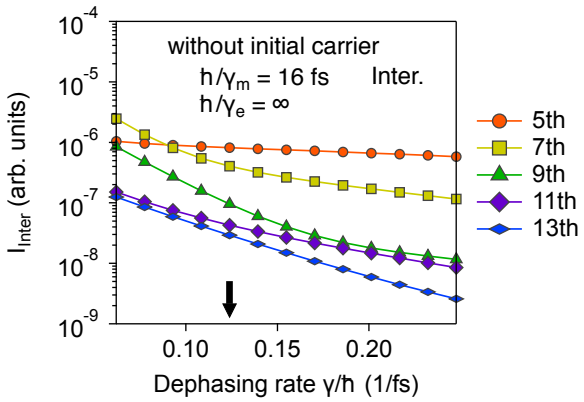

Figure B.5: The dependence of interband harmonic intensity on dephasing rate without initial carriers, and $\hbar/\gamma_m = 16$ fs and $\hbar/\gamma_e = \infty$. The black arrow represents the dephasing rate corresponding to $\hbar/\gamma = 8$ fs, which is used for all other calculations.

B.6 Temperature dependence of the intraband harmonics

Figure B.6 shows the temperature dependence of intraband harmonics with the initial carrier of 3.7×10^{12} cm^{-2}. In this calculation, the dipole moment is set to 0 to neglect the effect of interband transition. The initial carrier distribution is assumed to follow the Fermi Dirac distribution without the excitonic effect at each temperature. The momentum relaxation is not introduced in this calculation. The intraband harmonics monotonically decreases with increasing the temperature in this condition. This is because the intraband current created by the electrons and holes in k-space cancels each other when the electrons and holes uniformly spread out in the Brillouin zone. This is related to the fact that the summation of group velocity over the Brillouin zone becomes zero.

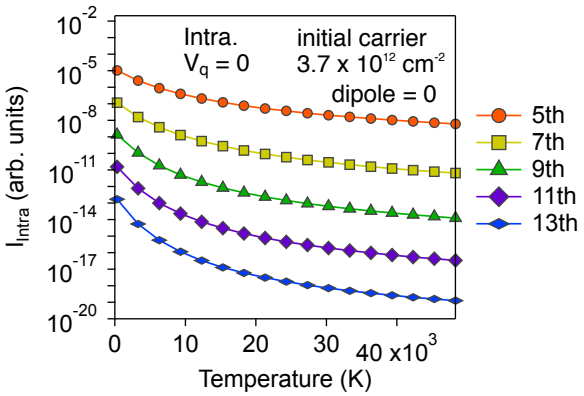

Figure B.6: Temperature dependence of intraband harmonics with initial carrier density of 3.7×10^{12} cm^{-2}. The initial carrier distribution is assumed to follow Fermi Dirac distribution without the excitonic effect ($V_q = 0$). The dipole moment was set to 0 to avoid the generation of carriers by the mid-infrared field. The momentum relaxation rate is set to 0.

Appendix C

C.1 Simulation code for semiconductor Bloch equation

The following shows a simulation code, which is used for the numerical calculation in Chapter 4. To check the correctness of the code, we confirmed the conservation of the length of the Bloch vector for each k point when the phenomenological scattering rates are switched off.

Listing C.1: Sample code for semiconductor Bloch equation (Julia)

```
using Distributed #for parallel computation

#for parallel computation
addprocs(1) #add Worker
nprocs() #number of Workers

@everywhere using LinearAlgebra
@everywhere using OrdinaryDiffEq
using Plots
@everywhere using DelimitedFiles
gr()

#-----------------------------------------------------------------------

#Parameters1
@everywhere Numk=75;#mesh number
@everywhere Numf=(Numk)*(Numk);#mesh number
@everywhere Numc=60;#time range of calculation (cycle)
@everywhere ω=0.26;#eV MIR frequency
@everywhere Trangeπ=2*/0.26*Numc;
@everywhere τ π ω
    =2*//16*60*sqrt(2)/sqrt(log(2))/2 # MIR pulse width = 60fs
#E=8.3:(MV/cm)
#a=3.28 angstrom: lattice constant of monolayer WSe2
#magnitude of vector potential
A0=8.3*3.28*10^(-2)ω/ #(*eEa/hbar/omega*)

#Parameter2
@everywhere Eg=1.89#eV#2D matrial paper
@everywhere dcv=0.284#WSe2 stark
@everywhere Ry=0.00525#estimated from excitonic stark shift in
    monolayer WSe2
@everywhere γ=0.082#decoherence
@everywhere γ m=0.041#relaxation to equiliblium distribution
@everywhere dcoef0γ=4#e excitaion-induced dephasing
@everywhere dcoef=dcoef0/Numf#renormalized by mesh number
@everywhere tr0=1.4656085741#(eV)
```

```
35
36 #Definition of k-mesh
37 @everywhere dk=4*pi/sqrt(3)/Numk;
38 @everywhere function kmatfunc(Numf)
39   kmat=zeros(Float64,Numf,2)
40   l=1;
41  for i in 0:Numk-1
42     for j in 0:Numk-1
43       kmat[l,:] = [dk*0.5*sqrt(3)*(j+i), dk*(i-j)*0.5]
44       l+=1
45      end
46   end
47
48   return kmat
49 end
50 kmatc=zeros(Float64,Numf,2);
51 kmatc=kmatfunc(Numf);
52
53
54 @everywhere function fxm(kx,ky)
55   return 1+4*cos(sqrt(3)*ky/2)*cos(kx/2)+4*(cos(kx/2))^2
56 end
57
58 #fitting result for exciton wave function (Vector)
59 @everywhere function exfitm(kmatx::Vector{Float64},kmaty::Vector{
      Float64})::Vector{Float64}
60   b0 = 0.00956224
61   b1 = 0.0963467
62   b2 = 0.896374
63   b3 = 0.00254523
64   sig = 4.89707
65   return @. (b0*(b1 + fxm(kmatx, kmaty))^(-b2) + b3)*exp(-fxm(kmatx,
         kmaty)/sig^2)
66 end
67
68 #-----------------------------------------------------------------

69 #functions
70 #band structure
71 @everywhere function Genergy(kx,ky)::Float64
72     return sqrt(Eg^2 + 4*tr0^2*(1 + 4*cos(sqrt(3)*ky/2)*cos(kx/2)+4*(
          cos(kx/2))^2));
73 end
74
75 @everywhere function Genergy2(kmatx::Vector{Float64},kmaty::Vector{
      Float64})::Vector{Float64}
76     return @. sqrt(Eg^2 + 4*tr0^2*(1 + 4*cos(sqrt(3)*kmaty/2)*cos(
          kmatx/2)+4*(cos(kmatx/2))^2));
77 end
78 #gradient of the band structure
79 @everywhere function diff(kx,ky)::Vector{Float64}
80     return [tr0^2*(-4*cos(kx/2)*sin(kx/2)-2*cos((sqrt(3)*ky)/2)*sin(
          kx/2))/(2*sqrt(Eg^2/4+tr0^2*(1+4*cos(kx/2)^2+4*cos(kx/2)*cos(
          sqrt(3)*ky/2)))),-(tr0^2*sqrt(3)*cos(kx/2)*sin(sqrt(3)*ky/2))
          /sqrt(Eg^2/4+tr0^2*(1+4*cos(kx/2)^2+4*cos(kx/2)*cos(sqrt(3)*
          ky/2)))]
81 end
82
83 @everywhere function diff2(kmatx,kmaty)
84     return @. tr0^2*(-4*cos(kmatx/2)*sin(kmatx/2)-2*cos((sqrt(3)*
          kmaty)/2)*sin(kmatx/2))/(2*sqrt(Eg^2/4+tr0^2*(1+4*cos(kmatx
```

```
        /2)^2+4*cos(kmatx/2)*cos(sqrt(3)*kmaty/2))))
85 end
86
87 #MIR electric field
88 @everywhere function Al(t,A0ω τ,,,t0)::Float64
89 return A0*sinω (*t)*exp(-(t-t0)τ^2/^2)
90 end
91
92 @everywhere function El(t,A0ω τ,,,t0)::Float64
93 return -A0ω**cosω (*t)*exp(-(t-t0)τ^2/^2)+2*A0*(t-t0)τ/^2*sinω
       (*t)*exp(-(t-t0)τ^2/^2)
94 end
95
96
97 #---------------------------------------------------------------------

98 # calculation of mat_Vqc takes 10~15 minutes
99
100 # summing up reciprocal vecters for nearest 9 Brillouin zones
101 @everywhere function gvecfunc()
102     gvec=zeros(Float64,361,2)
103     l=1;
104     for i in -9:9
105       for j in -9:9
106         gvec[l,:] = [2*pi*(j+i), 2*pi/sqrt(3)*(i-j)]
107         l+=1
108        end
109     end
110     return gvec
111   end
112
113
114   #Vq:Coulomb interaction between k-points
115   @everywhere function mat_Vqfunc(kmat, Numf)
116       mat_Vq=zeros(Complex{Float64},Numf,Numf);
117       gvec=gvecfunc()
118       for l in 1:Numf
119           for m in 1:Numf
120               if l==m
121               else
122                   mat_Vq[l,m]=sum(dk^2.1./sqrt.((kmat[l,1]-kmat[m,1].+
                        gvec[:,1]).^2+(kmat[l,2]-kmat[m,2].+gvec[:,2])
                        .^2))
123               end
124           end
125       end
126       return (mat_Vq+mat_Vq')/2
127   end
128
129   mat_Vqc=zeros(Float64,Numf,Numf);
130   mat_Vqc=mat_Vqfunc(kmatc, Numf);
131 #Differential equation to solve γ
132
133 #.-.-dcoef*w : Excitation-induced dephasing
134 #+complex(0,1)*Ry*(mat_Vqc*u) : Coulomb interaction γ
135 #.-m*(v.-w*z/sum(z)) : momentum scattering
136
137
138 #---------------------------------------------------------------------

139
```

```
@everywhere function semibloch(dr,r,p,t)
    A0ω τ,,,t0,dcv,Ryγ,,dcoef,kmatc,mat_Vqcγ,m=p
    u = r[:,1]
    v = r[:,2]
    w=sum(real(v))
    z=exfitm(kmatc[:,1].-Al(t,A0ω τ,,,t0),kmatc[:,2])
    dr[:,1]=(-complex(0,1)*Genergy2(kmatc[:,1].-Al(t,A0ω τ,,,t0),
        kmatc[:,2])).*u-complex(0,1)*(2*real(v).-1)*dcv*El(t,A0ω τ
        ,,,t0)+complex(0,1)*Ry*(mat_Vqc*u)
    dr[:,2]=2*dcv*El(t,A0ω τ,,,t0)*imag(u)γ.-m*(v.-w*z/sum(z))
end

 #Hamiltonian in the basis of k (independent electron)
 @everywhere function Hamiltonian(dk,Ry,kmatc)
    mat_H=zeros(Float64,Numf,Numf)
    mat_H=-Ry*mat_Vqc
    for l in 1:Numf
        mat_H[l,l]=Genergy(kmatc[l,1],kmatc[l,2])
    end
    return mat_H
end

#-----------------------------------------------------------------------

# For the setting of Ry so that the energy of lowest exciton state
    match that in my exp. 1.63eV
# Confirmation of lowest energy exciton ~ 1 minutes

mat_H=Hamiltonian(dk,Ry,kmatc)
eigmin(mat_H)

#-----------------------------------------------------------------------

# Calculation of lowest energy exciton 1~2 minutes

#optical spectra
@everywhere mat_H=zeros(Float64,Numf,Numf)
mat_H=Hamiltonian(dk,Ry,kmatc)
# diagonalization of Hamiltonian
@everywhere εψ,=eigen(mat_H)
@everywhere εs=realε()
@everywhere ψzeros=zeros(Complex{Float64},Numf)
for i in 1:Numfψ
   zeros[i]=dk*sumψ([:,i])
end
Nump=2000
Range=3#eV
de=Range/Nump
absorp=zeros(Complex{Float64},Nump)
absorp2=zeros(Float64,Nump)

for i in 1:Nump
       absorp[i]=sum((absψ.(zeros[:])).^2 ./((de*iε
           .-[:]).-complex(0,1)γ*))
end
absorp2=imag(absorp)
plot(absorp2)

#-----------------------------------------------------------------------
```

```
193 #path
194 cd("-----path-------")
195 pwd()
196 #file name
197 @everywhere str="-------name-------"::String
198
199 #---------------------------------------------------------------------

200 # for temperature dependence -----------------
201 using NLsolve
202 function nls(func, params...; ini = [0.0])
203     if typeof(ini) <: Number
204         r = nlsolve((vout,vin)->vout[1]=func(vin[1],params...), [ini
                ])
205         v = r.zero[1]
206     else
207         r = nlsolve((vout,vin)->vout .= func(vin,params...), ini)
208         v = r.zero
209     end
210     return v, r.f_converged
211 end
212
213 f(mu,temp)=(sum(1 ./(1 .+exp.((Genergy2(kmatc[:,1],kmatc[:,2]).-mu)
        /(8.61734e-05*temp))))/Numf-0.0034484)
214 #initial carrier distribution (1s exciton): File export
215
216 #---------------------------------------------------------------------

217 @everywhere rep=16 # repetition
218 Nk=zeros(Float64,Numf)
219 for l in 1:rep+1
220    Nk[:]=exfitm(kmatc[:,1],kmatc[:,2])*(l-1)*0.36572563 #
          distribution of photo-carrier: density =
          0.62 x 10^12 cm-2 * (l-1)
221
222    # for temperature dependence -----------------
223    #temp=300+l*3000
224    #mu=nls(f,temp,ini = 2.0)[1]
225    #Nk[:]=1 ./(1 .+exp.((Genergy2(kmatc[:,1],kmatc[:,2]).-mu)
          /(8.61734e-05*temp)))
226    # ------------------------------------------
227
228         open("Nk_"*str*"_$(l).txt","w") do out
229             Base.print_array(out,hcat(Nk[:]))
230         end
231 end
232
233 #---------------------------------------------------------------------

234 #Function to solve differential equation
235
236 @everywhere rep=16
237 @everywhere Numpoint=4800
238 @everywhere function numerical(l)
239     A0=8.3*3.28*10^(-2)ω/γ
240     #=0.041+0.041/4*(l-1)γ
241     #m=0.0041*(l-1)
242     #parameters
243     p=[A0ω τ,,,Trange/2,dcv,Ryγ,,dcoef,kmatc,mat_Vqcγ,m]
244     #time range
245     tspan=(0.0,Trange)
```

```
246     #intial value
247     mat_rho=zeros(Complex{Float64},Numf,2);
248     #mat_rho[:,2]=readdlm("Nk_"*str*"_$(2).txt");
249     prob = ODEProblem(semibloch,mat_rho,tspan,p)
250     #Tsitouras 5/4 Runge\UTF{2013}Kutta method Tsit5()
251     sol= solve(prob,Tsit5(),reltol=1e-16,abstol=1e-16,saveat=Trange/
            Numpoint);
252     return sol
253 end
254
255
256 #---------------------------------------------------------------------

257 #calculation of current, total carrier number
258 # typical calculation time = 20~30 minutes
259 # typical calculation time without Coulomb, EID, and momentum
        scattering = 2 minutes
260
261 for l in 1:rep+1
262     Pt=zeros(Float64,Numpoint)
263     Nt=zeros(Float64,Numpoint)
264     Ct=zeros(Float64,Numpoint)
265
266     # calculation
267     BB=numerical(l)
268     for i in 1:Numpoint
269         # interband
270         Pt[i]=sum(2*Genergy2(kmatc[:,1].-Al(i*Trange/Numpoint,A0ω τ
                ,,,Trange/2),kmatc[:,2]).*imag(dcv*BB(i*Trange/Numpoint)
                [:,1]))
271         # total carrier
272         Nt[i]=sum(real(BB(i*Trange/Numpoint)[:,2]))
273         # intraband
274         Ct[i]=sum(2*diff2(kmatc[:,1].-Al(i*Trange/Numpoint,A0ω τ ,,,
                Trange/2),kmatc[:,2]).*real(BB(i*Trange/Numpoint)[:,2]))
275
276     end
277     Pt*=1/Numf
278     Nt*=1/Numf
279     Ct*=1/Numf
280
281     open("Pt_"*str*"_$(l).txt","w") do out
282         Base.print_array(out,hcat(Pt[:]))
283     end
284     open("Nt_"*str*"_$(l).txt","w") do out
285         Base.print_array(out,hcat(Nt[:]))
286      end
287      open("Ct_"*str*"_$(l).txt","w") do out
288         Base.print_array(out,hcat(Ct[:]))
289      end
290
291     #Carrier distribution after MIR pulse irradiation
292     Nk=zeros(Float64,Numf)
293     Nk[:]=real(BB(Trange)[:,2])
294     open("Nkm_"*str*"_$(l).txt","w") do out
295         Base.print_array(out,hcat(Nk[:]))
296     end
297 end
298
299 #---------------------------------------------------------------------
```

```
300 #initilization
301 BB=0
302
303 # Export electric field
304 Numpoint=4800
305 Et=zeros(Float64,Numpoint)
306
307 for i in 1:Numpoint
308     Et[i]=El(i*Trange/Numpoint,A0ω τ,,,Trange/2)
309 end
310 open("Et_"*str*"_$(1)).txt","w") do out
311     Base.print_array(out,hcat(Et[:]))
312 end
```

Acknowledgement

First of all, I would like to thank my family. My research life in the master's and doctoral programs would not have been possible without their financial and mental support.

I am grateful to members of Department of Physics, Kyoto University. In particular, I would like to sincerely thank my supervisor, Prof. Koichiro Tanaka, for giving me a lot of indicative advice. He allowed me to be free in all aspects of my research life and has provided me with many educational instructions and discussions. Thanks to the discussions as equals as researchers, I could think for myself and carry out my research. I thank Prof. Nobuko Naka, who gave me a lot of suggestions on how to present my research and especially gave me objective and accurate guidance based on her comprehensive understanding of my overall research. I thank Prof. Takashi Arikawa, who has been my mentor since I was a third-year undergraduate student. He helped me develop an interest in the study of solid-state spectroscopy. I am especially grateful to Prof. Naotaka Yoshikawa at the University of Tokyo for building the basis of my research field and encouraging me to join the solid-state spectroscopy group. I was encouraged by his warm support. I am deeply grateful to Dr. Kento Uchida. He has been the most supportive of my research, and we have spent more time and discussions together than anyone else. I could not proceed with my research without his advice. I am also grateful to Dr. Satoshi Kusaba, who has been my mentor since my fourth year, for his much guidance in preparing my samples and his kind helps for my research.

I want to offer my special thanks to Prof. Yasumitsu Miyata, Mr. Takahiko Endo, and Mr. Hiroshi Shimizu in Tokyo Metropolitan University for their help in preparing samples for our collaborative research. Their high-quality samples are beneficial for my experiments. I am also grateful to Prof. Kazuhiro Yanagi and Mr. Hiroyuki Nishidome in Tokyo Metropolitan University for the many experiments and discussions. Our five years of research together have provided me with much knowledge that I could not have gained in our laboratory. I also thank my collaborator, Mr. Vivek Pareek, and Prof. Keshav M. Dani at Okinawa Institute of Science and Technology. I am grateful to Mr. Kenji Oba for his great support for my research on two-dimensional magnets.

I want to thank Prof. Masayuki Watanabe, Prof. Motoaki Bamba, Dr. Yuta Inose, Dr. Mitsuyoshi Takahata, Dr. Tomoki Hiraoka, Dr. Tomoaki Ichii, Dr. Konishi Kazuki, Dr. Yasuyuki Sanari, and Mr. Kousei Shimomura for supporting me in various aspects such as research discussions and daily life. I would also like to thank Mr. Yoshiki Kubo and Mr. Kenji Takiguchi for teaching me how to have an enjoyable time, and fun younger students, Mr. Kohei Eguchi, Mr. Masayuki Hojo, Mr. Ritaro Toda, Mr. Ryota Aoki, Mr. Rei Shimanoe, and Mr. Shinya Takahashi.

I want to express my gratitude to all members of the solid-state spectroscopy group. I could write this thesis thanks to everyone who has helped me. I am genuinely grateful to all of them.

Bibliography

[1] K. Nagai, K. Uchida, N. Yoshikawa, T. Endo, Y. Miyata, and K. Tanaka, Communications Physics **3**, 137 (2020).

[2] P. A. Franken, A. E. Hill, C. W. Peters, and G. Weinreich, Physical Review Letters **7**, 118 (1961).

[3] M. Wegener, *Extreme nonlinear optics : an introduction*Advanced Texts in Physics (Springer, Berlin/Heidelberg, 2005).

[4] D. Strickland and G. Mourou, Optics Communications **56**, 219 (1985).

[5] S.-W. Bahk, P. Rousseau, T. A. Planchon, V. Chvykov, G. Kalintchenko, A. Maksimchuk, G. A. Mourou, and V. Yanovsky, Optics Letters **29**, 2837 (2004).

[6] J. W. Yoon, Y. G. Kim, I. W. Choi, J. H. Sung, H. W. Lee, S. K. Lee, and C. H. Nam, Optica **8**, 630 (2021).

[7] 大森賢治, **アト秒科学: １京分の１秒スケールの超高速現象を光で観測・制御する** (化学同人, 2015).

[8] S. Y. Kruchinin, F. Krausz, and V. S. Yakovlev, Reviews of Modern Physics **90**, 021002 (2018).

[9] E. Goulielmakis, V. S. Yakovlev, A. L. Cavalieri, M. Uiberacker, V. Pervak, A. Apolonski, R. Kienberger, U. Kleineberg, and F. Krausz, Science **317**, 769 (2007).

[10] F. Krausz and M. I. Stockman, Nature Photonics **8**, 205 (2014).

[11] A. Schiffrin, T. Paasch-Colberg, N. Karpowicz, V. Apalkov, D. Gerster, S. Mühlbrandt, M. Korbman, J. Reichert, M. Schultze, S. Holzner, J. V. Barth, R. Kienberger, R. Ernstorfer, V. S. Yakovlev, M. I. Stockman, and F. Krausz, Nature **493**, 70 (2013).

[12] M. Garg, M. Zhan, T. T. Luu, H. Lakhotia, T. Klostermann, A. Guggenmos, and E. Goulielmakis, Nature **538**, 359 (2016).

[13] F. Langer, C. P. Schmid, S. Schlauderer, M. Gmitra, J. Fabian, P. Nagler, C. Schüller, T. Korn, P. G. Hawkins, J. T. Steiner, U. Huttner, S. W. Koch, M. Kira, and R. Huber, Nature **557**, 76 (2018).

[14] J. Reimann, S. Schlauderer, C. P. Schmid, F. Langer, S. Baierl, K. A. Kokh, O. E. Tereshchenko, A. Kimura, C. Lange, J. Güdde, U. Höfer, and R. Huber, Nature **562**, 396 (2018).

[15] G. Floquet, Annales scientifiques de l'École normale supérieure **12**, 47 (1883).

[16] J. H. Shirley, Physical Review **138**, B979 (1965).

[17] H. Sambe, Physical Review A **7**, 2203 (1973).

[18] T. Oka and S. Kitamura, Annual Review of Condensed Matter Physics **10**, 387 (2019).

[19] F. Harper, R. Roy, M. S. Rudner, and S. Sondhi, Annual Review of Condensed Matter Physics **11**, 345 (2020).

[20] M. S. Rudner and N. H. Lindner, Nature Reviews Physics **2**, 229 (2020).

[21] A. Cavalleri, C. Tóth, C. W. Siders, J. A. Squier, F. Ráksi, P. Forget, and J. C. Kieffer, Physical Review Letters **87**, 237401 (2001).

[22] D. H. D. N. Basov, R. D. Averitt, Nature Materials **16**, 1077 (2017).

[23] A. McPherson, G. Gibson, H. Jara, U. Johann, T. S. Luk, I. A. McIntyre, K. Boyer, and C. K. Rhodes, Journal of the Optical Society of America B **4**, 595 (1987).

[24] P. B. Corkum, Physical Review Letters **71**, 1994 (1993).

[25] C. Winterfeldt, C. Spielmann, and G. Gerber, Reviews of Modern Physics **80**, 117 (2008).

[26] T. Popmintchev, M.-C. Chen, D. Popmintchev, P. Arpin, S. Brown, S. Ališauskas, G. Andriukaitis, T. Balčiunas, O. D. Mücke, A. Pugzlys, A. Baltuška, B. Shim, S. E. Schrauth, A. Gaeta, C. Hernández-García, L. Plaja, A. Becker, A. Jaron-Becker, M. M. Murnane, and H. C. Kapteyn, Science **336**, 1287 (2012).

[27] C.-G. Wahlstrom, J. Larsson, A. Persson, T. Starczewski and S. Svanberg, Physical Review A **48**, 4709 (1993).

[28] N. Ben-Tal, N. Moiseyev, and A. Beswick, Journal of Physics B: Atomic, Molecular and Optical Physics **26**, 3017 (1993).

[29] M. Lewenstein, P. Balcou, M. Y. Ivanov, A. L'Huillier, and P. B. Corkum, Physical Review A **49**, 2117 (1994).

[30] J. Li, J. Lu, A. Chew, S. Han, J. Li, Y. Wu, H. Wang, S. Ghimire, and Z. Chang, Nature Communications **11**, 2748 (2020).

[31] J. Itatani, J. Levesque, D. Zeidler, H. Niikura, H. Pépin, J. C. Kieffer, P. B. Corkum, and D. M. Villeneuve, Nature **432**, 867 (2004).

[32] P. M. Kraus, B. Mignolet, D. Baykusheva, A. Rupenyan, L. Horný, E. F. Penka, G. Grassi, O. I. Tolstikhin, J. Schneider, F. Jensen, L. B. Madsen, A. D. Bandrauk, F. Remacle, and H. J. Wörner, Science **350**, 790 (2015).

[33] S. Ghimire and D. A. Reis, Nature Physics **15**, 10 (2019).

[34] T. T. Luu and H. J. Wörner, Nature Communications **9**, 916 (2018).

[35] C. B. Schaffer, A. Brodeur, and E. Mazur, Measurement Science and Technology **12**, 1784 (2001).

[36] A. H. Chin, O. G. Calderón, and J. Kono, Physical Review Letters **86**, 3292 (2001).

[37] S. Ghimire, A. D. Dichiara, E. Sistrunk, P. Agostini, L. F. Dimauro, and D. A. Reis, Nature Physics **7**, 138 (2011).

[38] O. Schubert, M. Hohenleutner, F. Langer, B. Urbanek, C. Lange, U. Huttner, D. Golde, T. Meier, M. Kira, S. W. Koch, and R. Huber, Nature Photonics **8**, 119 (2014).

[39] T. T. Luu, M. Garg, A. Moulet, and E. Goulielmakis, Nature **521**, 498 (2015).

[40] G. Vampa, T. Hammond, N. Thiré, B. Schmidt, F. Légaré, C. McDonald, T. Brabec, and P. Corkum, Nature **522**, 462 (2015).

[41] M. Hohenleutner, F. Langer, O. Schubert, M. Knorr, U. Huttner, S. W. Koch, M. Kira, and R. Huber, Nature **523**, 572 (2015).

[42] G. Ndabashimiye, S. Ghimire, M. Wu, D. A. Browne, K. J. Schafer, M. B. Gaarde, and D. A. Reis, Nature **534**, 520 (2016).

[43] Y. S. You, D. A. Reis, and S. Ghimire, Nature Physics **13**, 345 (2017).

[44] H. Liu, Y. Li, Y. S. You, S. Ghimire, T. F. Heinz, and D. A. Reis, Nature Physics **13**, 262 (2017).

[45] Y. S. You, Y. Yin, Y. Wu, A. Chew, X. Ren, F. Zhuang, S. Gholam-mirzaei, M. Chini, Z. Chang, and S. Ghimire, Nature Communications **8**, 724 (2017).

[46] F. Langer, M. Hohenleutner, U. Huttner, S. W. Koch, M. Kira, and R. Huber, Nature Photonics **11**, 227 (2017).

[47] H. Kim, S. Han, Y. W. Kim, S. Kim, and S. W. Kim, ACS Photonics **4**, 1627 (2017).

[48] G. Vampa, T. J. Hammond, M. Taucer, X. Ding, X. Ropagnol, T. Ozaki, S. Delprat, M. Chaker, N. Thiré, B. E. Schmidt, F. Légaré, D. D. Klug, A. Y. Naumov, D. M. Villeneuve, A. Staudte, and P. B. Corkum, Nature Photonics **12**, 465 (2018).

[49] K. Kaneshima, Y. Shinohara, K. Takeuchi, N. Ishii, K. Imasaka, T. Kaji, S. Ashihara, K. L. Ishikawa, and J. Itatani, Physical Review Letters **120**, 243903 (2018).

[50] P. Xia, C. Kim, F. Lu, T. Kanai, H. Akiyama, J. Itatani, and N. Ishii, Optics Express **26**, 29393 (2018).

[51] M. Garg, H. Y. Kim, and E. Goulielmakis, Nature Photonics **12**, 291 (2018).

[52] N. Yoshikawa, K. Nagai, K. Uchida, Y. Takaguchi, S. Sasaki, Y. Miyata, and K. Tanaka, Nature Communications **10**, 3709 (2019).

[53] Y. Sanari, T. Otobe, Y. Kanemitsu, and H. Hirori, Nature Communications **11**, 3069 (2020).

[54] A. J. Uzan, G. Orenstein, Á. Jiménez-Galán, C. McDonald, R. E. F. Silva, B. D. Bruner, N. D. Klimkin, V. Blanchet, T. Arusi-Parpar, M. Krüger, A. N. Rubtsov, O. Smirnova, M. Ivanov, B. Yan, T. Brabec, and N. Dudovich, Nature Photonics **14**, 183 (2020).

[55] H. Lakhotia, H. Y. Kim, M. Zhan, S. Hu, S. Meng, and E. Goulielmakis, Nature **583**, 55 (2020).

[56] N. Yoshikawa, T. Tamaya, and K. Tanaka, Science **356**, 736 (2017).

[57] H. A. Hafez, S. Kovalev, J.-C. Deinert, Z. Mics, B. Green, N. Awari, M. Chen, S. Germanskiy, U. Lehnert, J. Teichert, Z. Wang, K.-J. Tielrooij, Z. Liu, Z. Chen, A. Narita, K. Müllen, M. Bonn, M. Gensch, and D. Turchinovich, Nature **561**, 507 (2018).

[58] M. Baudisch, A. Marini, J. D. Cox, T. Zhu, F. Silva, S. Teichmann, M. Massicotte, F. Koppens, L. S. Levitov, F. J. García de Abajo, and J. Biegert, Nature Communications **9**, 1018 (2018).

[59] B. Cheng, N. Kanda, T. N. Ikeda, T. Matsuda, P. Xia, T. Schumann, S. Stemmer, J. Itatani, N. P. Armitage, and R. Matsunaga, Physical Review Letters **124**, 117402 (2020).

[60] S. Kovalev, R. M. Dantas, S. Germanskiy, J. C. Deinert, B. Green, I. Ilyakov, N. Awari, M. Chen, M. Bawatna, J. Ling, F. Xiu, P. H. van Loosdrecht, P. Surówka, T. Oka, and Z. Wang, Nature Communications **11**, 6 (2020).

[61] M. R. Bionta, E. Haddad, A. Leblanc, V. Gruson, P. Lassonde, H. Ibrahim, J. Chaillou, N. Émond, M. R. Otto, Á. Jiménez-Galán, R. E. F. Silva, M. Ivanov, B. J. Siwick, M. Chaker, and F. Légaré, Physical Review Research **3**, 023250 (2021).

[62] A. Korobenko, S. Saha, A. T. Godfrey, M. Gertsvolf, A. Y. Naumov, D. M. Villeneuve, A. Boltasseva, V. M. Shalaev, and P. B. Corkum, Nature Communications **12**, 1 (2021).

[63] Y. Bai, F. Fei, S. Wang, N. Li, X. Li, F. Song, R. Li, Z. Xu, and P. Liu, Nature Physics **17**, 311 (2021).

[64] C. P. Schmid, L. Weigl, P. Grössing, V. Junk, C. Gorini, S. Schlauderer, S. Ito, M. Meierhofer, N. Hofmann, D. Afanasiev, J. Crewse, K. A. Kokh, O. E. Tereshchenko, J. Güdde, F. Evers, J. Wilhelm, K. Richter, U. Höfer, and R. Huber, Nature **593**, 385 (2021).

[65] Y. Y. Lv, J. Xu, S. Han, C. Zhang, Y. Han, J. Zhou, S. H. Yao, X. P. Liu, M. H. Lu, H. Weng, Z. Xie, Y. B. Chen, J. Hu, Y. F. Chen, and S. Zhu, Nature Communications **12**, 1 (2021).

[66] C. Zener, Proceedings of the Royal Society A: Mathematical, Physical and Engineering Sciences **145**, 523 (1934).

[67] G. Vampa, C. R. McDonald, G. Orlando, D. D. Klug, P. B. Corkum, and T. Brabec, Physical Review Letters **113**, 073901 (2014).

[68] G. Vampa, B. G. Ghamsari, S. Siadat Mousavi, T. J. Hammond, A. Olivieri, E. Lisicka-Skrek, A. Y. Naumov, D. M. Villeneuve, A. Staudte, P. Berini, and P. B. Corkum, Nature Physics **13**, 659 (2017).

[69] M. Wu, S. Ghimire, D. A. Reis, K. J. Schafer, and M. B. Gaarde, Physical Review A **91**, 043839 (2015).

[70] P. Földi, Physical Review B **96**, 1 (2017).

[71] G. Ernotte, T. J. Hammond, and M. Taucer, Physical Review B **98**, 1 (2018).

[72] D. Golde, T. Meier, and S. W. Koch, Physical Review B **77**, 075330 (2008).

[73] T. Otobe, Physical Review B **235152**, 2 (2016).

[74] N. Tancogne-Dejean, O. D. Mücke, F. X. Kärtner, and A. Rubio, Physical Review Letters **118**, 087403 (2017).

[75] F. H. M. Faisal and J. Z. Kamiński, Physical Review A **56**, 748 (1997).

[76] T. Higuchi, M. I. Stockman, and P. Hommelhoff, Physical Review Letters **113**, 213901 (2014).

[77] T. N. Ikeda, Physical Review A **97**, 063413 (2018).

[78] N. Dudovich, O. Smirnova, J. Levesque, Y. Mairesse, M. Y. Ivanov, D. M. Villeneuve, and P. B. Corkum, Nature Physics **2**, 781 (2006).

[79] Y. S. You, M. Wu, Y. Yin, A. Chew, X. Ren, S. Gholam-Mirzaei, D. A. Browne, M. Chini, Z. Chang, K. J. Schafer, M. B. Gaarde, and S. Ghimire, Optics Letters **42**, 1816 (2017).

[80] G. Vampa, T. J. Hammond, N. Thiré, B. E. Schmidt, F. Légaré, C. R. McDonald, T. Brabec, D. D. Klug, and P. B. Corkum, Physical Review Letters **115**, 193603 (2015).

[81] S. Han, H. Kim, Y. W. Kim, Y. J. Kim, S. Kim, I. Y. Park, and S. W. Kim, Nature Communications **7**, 1 (2016).

[82] M. Sivis, M. Taucer, G. Vampa, K. Johnston, A. Staudte, A. Y. Naumov, D. M. Villeneuve, C. Ropers, and P. B. Corkum, Science **357**, 303 (2017).

[83] Z.-X. Liu, B. Wang, H. Xiong, and Y. Wu, Optics Letters **43**, 3698 (2018).

[84] H. Nishidome, K. Nagai, K. Uchida, Y. Ichinose, Y. Yomogida, Y. Miyata, K. Tanaka, and K. Yanagi, Nano Letters **20**, 6215 (2020).

[85] B. Zaks, R. B. Liu, and M. S. Sherwin, Nature **483**, 580 (2012).

[86] F. Langer, M. Hohenleutner, C. P. Schmid, C. Poellmann, P. Nagler, T. Korn, C. Schüller, M. S. Sherwin, U. Huttner, J. T. Steiner, S. W. Koch, M. Kira, and R. Huber, Nature **533**, 225 (2016).

[87] B. Zaks, H. Banks, and M. S. Sherwin, Applied Physics Letters **102** (2013).

[88] H. B. Banks, Q. Wu, D. C. Valovcin, S. Mack, A. C. Gossard, L. Pfeiffer, R.-b. Liu, and M. S. Sherwin, Physical Review X **7**, 041042 (2017).

[89] R.-B. Liu and B.-F. Zhu, High-order THz-sideband generation in semiconductors, in *AIP Conference Proceedings*, volume 893, pp. 1455–1456, AIP, 2007.

[90] M. Borsch, C. P. Schmid, L. Weigl, S. Schlauderer, N. Hofmann, C. Lange, J. T. Steiner, S. W. Koch, R. Huber, and M. Kira, Science **370**, 1204 (2020).

[91] J. B. Costello, S. D. O'Hara, Q. Wu, D. C. Valovcin, L. N. Pfeiffer, K. W. West, and M. S. Sherwin, Nature **599**, 57 (2021).

[92] O. E. Alon, V. Averbukh, and N. Moiseyev, Physical Review Letters **80**, 3743 (1998).

[93] V. Averbukh, O. E. Alon, and N. Moiseyev, Physical Review A **60**, 2585 (1999).

[94] B. M. Fregoso, Y. H. Wang, N. Gedik, and V. Galitski, Physical Review B **88**, 155129 (2013).

[95] K. Ofer, P. Grychtol, E. Turgut, R. Knut, D. Zusin, D. Popmintchev, T. Popmintchev, H. Nembach, J. M. Shaw, A. Fleischer, H. Kapteyn, M. Murnane, and O. Cohen, Nature Photonics **9**, 99 (2015).

[96] T. Morimoto, H. C. Po, and A. Vishwanath, Physical Review B **95**, 195155 (2017).

[97] S. Xu and C. Wu, Physical Review Letters **120**, 096401 (2018).

[98] O. Neufeld, D. Podolsky, and O. Cohen, Nature Communications **10**, 405 (2019).

[99] O. Neufeld, D. Ayuso, P. Decleva, M. Y. Ivanov, O. Smirnova, and O. Cohen, Physical Review X **9**, 031002 (2019).

[100] O. Neufeld and O. Cohen, Physical Review Letters **123**, 103202 (2019).

[101] Y. H. Wang, H. Steinberg, P. Jarillo-Herrero, and N. Gedik, Science **342**, 453 (2013).

[102] J. W. McIver, B. Schulte, F.-U. Stein, T. Matsuyama, G. Jotzu, G. Meier, and A. Cavalleri, Nature Physics **16**, 38 (2020).

[103] X. M. Tong and S. I. Chu, Physical Review A - Atomic, Molecular, and Optical Physics **58**, R2656 (1998).

[104] A. Fleischer, O. Kfir, T. Diskin, P. Sidorenko, and O. Cohen, Nature Photonics **8**, 543 (2014).

[105] N. Saito, P. Xia, F. Lu, T. Kanai, J. Itatani, and N. Ishii, Optica **4**, 1333 (2017).

[106] Y.-R. Shen, *The Principles of Nonlinear Optics* (New York, 1984).

[107] S. Ghimire, A. D. DiChiara, E. Sistrunk, G. Ndabashimiye, U. B. Szafruga, A. Mohammad, P. Agostini, L. F. DiMauro, and D. A. Reis, Physical Review A **85**, 043836 (2012).

[108] G. Vampa, Y. S. You, H. Liu, S. Ghimire, and D. A. Reis, Optics Express **26**, 12210 (2018).

[109] K. S. Novoselov, A. K. Geim, S. V. Morozov, D. Jiang, Y. Zhang, S. V. Dubonos, I. V. Grigorieva, and A. A. Firsov, Science **306**, 666 (2004).

[110] X. Xu, W. Yao, D. Xiao, and T. F. Heinz, Nature Physics **10**, 343 (2014).

[111] K. F. Mak and J. Shan, Nature Photonics **10**, 216 (2016).

[112] G. Wang, A. Chernikov, M. M. Glazov, T. F. Heinz, X. Marie, T. Amand, and B. Urbaszek, Reviews of Modern Physics **90**, 21001 (2018).

[113] A. Splendiani, L. Sun, Y. Zhang, T. Li, J. Kim, C.-Y. Chim, G. Galli, and F. Wang, Nano Letters **10**, 1271 (2010).

[114] K. F. Mak, C. Lee, J. Hone, J. Shan, and T. F. Heinz, Physical Review Letters **105**, 136805 (2010).

[115] G.-B. Liu, W.-Y. Shan, Y. Yao, W. Yao, and D. Xiao, Physical Review B **88**, 085433 (2013).

[116] A. Chernikov, T. C. Berkelbach, H. M. Hill, A. Rigosi, Y. Li, O. B. Aslan, D. R. Reichman, M. S. Hybertsen, and T. F. Heinz, Physical Review Letters **113**, 076802 (2014).

[117] D. Xiao, G.-B. Liu, W. Feng, X. Xu, and W. Yao, Physical Review Letters **108**, 196802 (2012).

[118] D. Kozawa, R. Kumar, A. Carvalho, K. Kumar Amara, W. Zhao, S. Wang, M. Toh, R. M. Ribeiro, A. H. Castro Neto, K. Matsuda, and G. Eda, Nature Communications **5**, 4543 (2014).

[119] K. F. Mak, K. He, J. Shan, and T. F. Heinz, Nature Nanotechnology **7**, 494 (2012).

[120] H. Zeng, J. Dai, W. Yao, D. Xiao, and X. Cui, Nature Nanotechnology **7**, 490 (2012).

[121] T. Cao, G. Wang, W. Han, H. Ye, C. Zhu, J. Shi, Q. Niu, P. Tan, E. Wang, B. Liu, and J. Feng, Nature Communications **3**, 887 (2012).

[122] K. F. Mak, K. L. McGill, J. Park, and P. L. McEuen, Science **344**, 1489 (2014).

[123] Y. You, X.-X. Zhang, T. C. Berkelbach, M. S. Hybertsen, D. R. Reichman, and T. F. Heinz, Nature Physics **11**, 477 (2015).

[124] D. Sun, Y. Rao, G. A. Reider, G. Chen, Y. You, L. Brézin, A. R. Harutyunyan, and T. F. Heinz, Nano Letters **14**, 5625 (2014).

[125] A. Chernikov, C. Ruppert, H. M. Hill, A. F. Rigosi, and T. F. Heinz, Nature Photonics **9**, 466 (2015).

[126] A. Ramasubramaniam, Physical Review B - Condensed Matter and Materials Physics **86**, 1 (2012).

[127] P. Hänggi, *Quantum transport and dissipation* (Wiley, New York, 1988).

[128] M. S. Rudner and N. H. Lindner, arXiv , preprint arXiv:2003.08252v2 (2020).

[129] T. Oka and H. Aoki, Physical Review B **79**, 081406 (2009).

[130] T. Kitagawa, T. Oka, A. Brataas, L. Fu, and E. Demler, Physical Review B **84**, 235108 (2011).

[131] A. Kumar, M. Rodriguez-Vega, T. Pereg-Barnea, and B. Seradjeh, Physical Review B **101**, 174314 (2020).

[132] K. Konishi, T. Higuchi, J. Li, J. Larsson, S. Ishii, and M. Kuwata-Gonokami, Physical Review Letters **112**, 135502 (2014).

[133] K. L. Seyler, J. R. Schaibley, P. Gong, P. Rivera, A. M. Jones, S. Wu, J. Yan, D. G. Mandrus, W. Yao, and X. Xu, Nature Nanotechnology **10**, 407 (2015).

[134] R. Loudon and T. von Foerster, American Journal of Physics **42**, 1041 (1974).

[135] E. J. Sie, C. H. Lui, Y.-H. Lee, L. Fu, J. Kong, and N. Gedik, Science **355**, 1066 (2017).

[136] W. Kuehn, P. Gaal, K. Reimann, M. Woerner, T. Elsaesser, and R. Hey, Physical Review B **82**, 075204 (2010).

[137] N. H. Lindner, G. Refael, and V. Galitski, Nature Physics **7**, 490 (2011).

[138] F. Mahmood, C. K. Chan, Z. Alpichshev, D. Gardner, Y. Lee, P. A. Lee, and N. Gedik, Nature Physics **12**, 306 (2016).

[139] E. J. Sie, J. W. McIver, Y.-h. Lee, L. Fu, J. Kong, and N. Gedik, Nature Materials **14**, 290 (2015).

[140] K. Uchida, T. Otobe, T. Mochizuki, C. Kim, M. Yoshita, H. Akiyama, L. N. Pfeiffer, K. W. West, K. Tanaka, and H. Hirori, Physical Review Letters **117**, 277402 (2016).

[141] K. Kojima, H. E. Lim, Z. Liu, W. Zhang, T. Saito, Y. Nakanishi, T. Endo, Y. Kobayashi, K. Watanabe, T. Taniguchi, K. Matsuda, Y. Maniwa, Y. Miyauchi, and Y. Miyata, Nanoscale **11**, 12798 (2019).

[142] K. F. Mak, M. Y. Sfeir, Y. Wu, C. H. Lui, J. A. Misewich, and T. F. Heinz, Physical Review Letters **101**, 196405 (2008).

[143] P. Y. Yu and M. Cardona, *Fundamentals of Semiconductors* (Springer-Verlag Berlin Heidelberg, 2005).

[144] A. D. Shiner, B. E. Schmidt, C. Trallero-Herrero, H. J. Wörner, S. Patchkovskii, P. B. Corkum, J. C. Kieffer, F. Légaré, and D. M. Villeneuve, Nature Physics **7**, 464 (2011).

[145] S. Pabst and R. Santra, Physical Review Letters **111**, 2 (2013).

[146] K. K. Hansen, T. Deffge, and D. Bauer, Physical Review A **96**, 1 (2017).

[147] J. Li, S. Fu, H. Wang, X. Zhang, B. Ding, B. Hu, and H. Du, Physical Review A **98**, 043409 (2018).

[148] N. Tancogne-Dejean and A. Rubio, Science Advances **4**, 1 (2018).

[149] R. E. Silva, I. V. Blinov, A. N. Rubtsov, O. Smirnova, and M. Ivanov, Nature Photonics **12**, 266 (2018).

[150] Y. Murakami, M. Eckstein, and P. Werner, Physical Review Letters **121**, 057405 (2018).

[151] S. de Vega, J. D. Cox, F. Sols, and F. J. García de Abajo, Physical Review Research **2**, 013313 (2020).

[152] H. K. Avetissian, G. F. Mkrtchian, and K. Z. Hatsagortsyan, Physical Review Research **2**, 023072 (2020).

[153] I. Floss, C. Lemell, G. Wachter, V. Smejkal, S. A. Sato, X.-M. Tong, K. Yabana, and J. Burgdörfer, Physical Review A **97**, 011401 (2018).

[154] Z. Wang, H. Park, Y. H. Lai, J. Xu, C. I. Blaga, F. Yang, P. Agostini, and L. F. DiMauro, Nature Communications **8**, 1686 (2017).

[155] C. Heide, Y. Kobayashi, A. Johnson, F. Liu, T. F. Heinz, D. A. Reis, and S. Ghimire, arXiv , preprint arXiv:2109.04508v1 (2021).

[156] L. Schultheis, J. Kuhl, A. Honold, and C. W. Tu, Physical Review Letters **57**, 1635 (1986).

[157] H. Wang, K. Ferrio, D. G. Steel, Y. Z. Hu, R. Binder, and S. W. Koch, Physical Review Letters **71**, 1261 (1993).

[158] G. Moody, C. Kavir Dass, K. Hao, C.-H. Chen, L.-J. Li, A. Singh, K. Tran, G. Clark, X. Xu, G. Berghäuser, E. Malic, A. Knorr, and X. Li, Nature Communications **6**, 8315 (2015).

[159] Z. Li, T. Wang, C. Jin, Z. Lu, Z. Lian, Y. Meng, M. Blei, M. Gao, T. Taniguchi, K. Watanabe, T. Ren, T. Cao, S. Tongay, D. Smirnov, L. Zhang, and S.-F. Shi, ACS Nano **13**, 14107 (2019).

[160] T. Zhang and J. Wang, ACS Photonics **8**, 2770 (2021).

[161] I. H. Malitson and M. J. Dodge, Journal of the Optical Society of America **62**, 1425 (1972).

[162] Y. Yu, Y. Yu, C. Xu, A. Barrette, K. Gundogdu, and L. Cao, Physical Review B **93**, 201111 (2016).

[163] M. Kira and S. Koch, Progress in Quantum Electronics **30**, 155 (2006).

[164] 浅野建一, **固体電子の量子論** (東京大学出版会, 2019).

[165] H. Haug and S. W. Koch, *Quantum Theory of the Optical and Electronic Properties of Semiconductors* (WORLD SCIENTIFIC, 2009).

[166] J. B. Krieger and G. J. Iafrate, Physical Review B **33**, 5494 (1986).

[167] J. Li, X. Zhang, S. Fu, Y. Feng, B. Hu, and H. Du, Physical Review A **100**, 43404 (2019).

[168] J. Kim, X. Hong, C. Jin, S.-F. Shi, C.-Y. S. Chang, M.-H. Chiu, L.-J. Li, and F. Wang, Science **346**, 1205 (2014).

[169] S. Jiang, H. Wei, J. Chen, C. Yu, R. Lu, and C. D. Lin, Physical Review A **96**, 053850 (2017).

[170] L. H. Brixner, Journal of Inorganic and Nuclear Chemistry **24**, 257 (1962).

[171] S. Park, N. Mutz, T. Schultz, S. Blumstengel, A. Han, A. Aljarb, L.-J. Li, E. J. W. List-Kratochvil, P. Amsalem, and N. Koch, 2D Materials **5**, 025003 (2018).

[172] A. Steinhoff, M. Rösner, F. Jahnke, T. O. Wehling, and C. Gies, Nano Letters **14**, 3743 (2014).

[173] J. Kim, X. Hong, C. Jin, S. F. Shi, C. Y. S. Chang, M. H. Chiu, L. J. Li, and F. Wang, Science **346**, 1205 (2014).

[174] K. Uchida, V. Pareek, K. Nagai, K. M. Dani, and K. Tanaka, Physical Review B **103**, L161406 (2021).